Final_Thesis_-_Copy_1.pdf

by Mohammad Nashiruzzaman

Submission date: 24-Sep-2025 02:49PM (UTC+0600)
Submission ID: 2760551799
File name: Final_Thesis_-_Copy_1.pdf (6.4M)
Word count: 27953
Character count: 128946

STUDY OF STRUCTURAL, DIELECTRIC, ELECTRICAL AND MAGNETIC PROPERTIES OF NiCdAl BULK FERRITES



By

Nur Mohammed

Student ID: 20MPHY004P

A thesis submitted in partial fulfillment of the requirement for the degree of

MASTER of PHILOSOPHY

Department of Physics

CHITTAGONG UNIVERSITY OF ENGINEERING AND TECHNOLOGY

August 2025

Declaration of Candidate

I hereby authorize that all the information in this thesis have collected and presented in compliance with ethical standards and academic regulations. As far as I am aware and believe, the Thesis does not incorporate any content that has been published by others, except in instances where proper references are acknowledged. Moreover, the thesis is in accordance with the PLAGIARISM and ACADEMIC INTEGRITY policies established by CUET.

Nur Mohammed

Student ID: 20MPHY004P

Department of Physics

Chittagong University of Engineering and Technology (CUET)

Copyright © Nur Mohammed, 2025.

This work may not be copied without the permission of the author or Chittagong University of Engineering and Technology.

Dedicated to my Parents,

&

Beloved wife

Sarmin Akther.

List of Publications

Journal Article

- Publication: Nur Mohammed, Arjumanara Bagum , Md. Shahbaz Khan and M. Belal Hossen Structural with Rietveld Analysis and Enhancement of Magnetic, Magnetocaloric study of Al substituted Ni-Cd Bulk spinel ferrites, Applied Physics A : Materials Science and Processing, 131, 216, 2025, DOI : 10.1007/s00339-025-08295-3.
- Nur Mohammed, Arjumanara Bagum , M. Belal Hossen , Investigation of Crystallite size, Strain effect, initial permeability and optical properties of Al substituted Ni-Cd dense ferrites, Journal of Engineering Science, 15(2), 2024, 79-88, DOI: https://doi.org/10.3329/jes.v15i2.82164

Conference Participation

- Nur Mohammed and M. Belal Hossen*, Analyzing of dielectric, electrical, and optical properties from structural perspective of Al substituted Ni-Cd nanoferrites , BCSIR , 1-3, December, 2022
- Nur Mohammed and M. Belal Hossen*, Investigation of Structural perspective and Magnetic, Electrical, Dielectric, Optical properties of Al substituted Ni-Cd nanoferrites and bulk ceramics, International Conference on Natural Science & Technology, 3-4 March , 2023,
- Nur Mohammed and M. Belal Hossen*, Exploration of Al substitution on the structural with Rietveld refinement analysis, magnetic, electrical, dielectric and optical properties of Ni-Al-Cd dense ceramics obtained from nanocrystalline Powder, ICPSDT-2023, September 7-8, 2023.

Declaration by the Supervisor

This is to certify that Nur Mohammed, Student ID no 20MPHY004P, conducted this research work under my supervision and met the requirements of the Chittagong University of Engineering and Technology's academic ordinance. As a result, he is qualified to submit the following thesis as part of his candidacy for the MASTER of PHILOSOPHY in Department of Physics. Furthermore, the thesis follows with the PLAGIARISM and ACADEMIC INTEGRITY rules of CUET.

Mohammad Belal Hossen, Ph.D.
Professor
Department of Physics
Chittagong University of Engineering and Technology (CUET)

Acknowledgment

First of all, I would like to express my deepest admiration and devotion to the almighty Allah who has given me the ability to complete this research work and submit this thesis.

I would like to extend my gratitude to my honorable supervisor Professor Dr. Mohammad Belal Hossen, a researcher at the Department of Physics, CUET, is acknowledged for his continued guidance, assistance, significant scientific discussions, helpful feedback and motivational influence throughout the entire investigation of this study.

I am very grateful to Professor Dr. H. M. A. R. Maruf, the Head of the Department, and Arjumanara Bagum, Assistant Professor at the department of Physics, CUET, for their remarkable suggestions that has greatly contributed to this work. I wish to acknowledge the contribution of the CUET faculty members in Physics, whose teachings and supportive feedback have enriched my academic knowledge.

My special thanks to Md. Sohel Rana, technical officer, at the department of Physics in CUET for his help during the preparation of the sample and experimental measurements.

Al last, I would like to express a deep gratitude for the moral encouragement and ongoing motivation offered by my family and friends. The completion of this dissertation is largely due to their love and support.

Thank you

Nur Mohammed

Abstract

$Ni_{0.65}Cd_{0.35}Fe_{2-x}Al_xO_4$ ($0 \leq x \leq 0.060$ with step 0.015) disc and toroid shaped bulk specimen has been fabricated from the sol-gel synthesized nanocrystalline powders and illustrated how influence of Al substitution in its structural, optical, dielectric, electric and magnetic properties. Structural characterization has been analyzed using X-ray diffraction (XRD) and Fourier Transform Infrared Spectra (FTIR) data. Theoretical analysis has been carried out using the Rietveld refinement method from the experimentally obtained XRD data. Crystallite size has been computed (39-36) nm, (43-36) nm, (64-46) nm, (44-38) nm applying Scherer's formula, modified Scherer's formula, Williamson-Hall method and Size-strain plot method respectively. Surface morphology as well as microstructure have been analyzed using Scanning Electron Microscope (SEM). From FTIR spectra, like force constant, stiffness constant, elastic moduli, wave velocities and Debye temperature have been estimated. Intrinsic magnetic hysteresis parameters at room temperature and temperature dependent magnetization have been measured using the Physical Properties Measurement System (PPMS). Law of Approach to saturation applied for theoretical analysis as well as magnetic entropy changes for relative cooling power estimated which is an important for magnetic caloric refrigeration application. Using optical properties measurement, Kramers - Kroning (K-K) relation is employed to compute the refractive index (n) and the extinction coefficient (K). Initial permeability spectra have been obtained from 20 to10MHz by an impedance analyzer in order to understand the high frequency application. Dielectric, permittivity, dielectric loss tangent and AC conductivity have been measured using impedance analyzer data. Complex impedance and modulus spectra have been calculated from impedance data as well as theoretical analysis of the grain and grain boundary parameters Rg, Rgb, Cg, Cgb using Z-sim software.

বিমূর্ত

$Ni_{0.65}Cd_{0.35}Fe_{2-x}Al_xO_4(0 \leq x \leq 0.060$ ধাপ 0.015) ডিস্ক এবং টরয়েড আকৃতির বাল্ক নমুনাটি সল-জেল সংশ্লেষিত ন্যানোক্রিস্টালাইন পাউডার থেকে তৈরী করা হয়েছে এবং অ্যালুমিনিয়াম (Al) প্রতিস্থাপনের সাথে তাদের কাঠামোগত , অপটিক্যাল, ডাইইলেকট্রিক, বৈদ্যুতিক এবং চৌম্বকীয় বৈশিষ্টগুলির প্রভাব চিত্রিত করা হয়েছে । এক্স-রে ডিফ্র্যাকশন (XRD) এবং ফুরিয়ার ট্রান্সফর্ম ইনফ্রারেড স্পেকট্রা (FTIR) ডাটা ব্যবহার করে কাঠামোগত বৈশিষ্ট বিশ্লেষণ করা হয়েছে । পরীক্ষামূলকভাবে প্রাপ্ত XRD ডাটা থেকে Rietveld refinement পদ্ধতি ব্যবহার করে তাত্ত্বিত বিশ্লেষণ করা হয়েছে । Scherer's, modified Scherer's, Williamson-Hall method এবং Size-strain plot পদ্ধতি প্রয়োগ করে স্ফটিকের আকার যথাক্রমে (৩৯-৩৬), (৪৩-৩৬), (৬৪-৩৪) এবং (৪৪-৩৮) ন্যানোমিটার গণনা করা হয়েছে । স্ক্যানিং ইলেকট্রন মাইক্রোস্কোপ (SEM) ব্যবহার করে Surface morphology এবং মাইক্রোস্ট্রাকচার বিশ্লেষণ করা হয়েছে । FTIR ডাটা থেকে, অ্যালুমিনিয়াম এর পরিমান বৃদ্ধির সাথে বল ধ্রুবক, কঠোরতা ধ্রুবক, স্থিতিস্থাপক মডিউলি, তরঙ্গ বেগ এবং ডিবাই তাপমাত্রাসহ স্থিতিস্থাপক বৈশিষ্টগুলি নির্ণয় করা হয়েছে । ভৌত বৈশিষ্টের পরিমাপ ব্যবস্থা (PPMS) ব্যবহার করে কক্ষ তাপমাত্রায় অভ্যন্তরীণ চৌম্বকীয় হিসটেরেসিস প্যারামিটার এবং তাপমাত্রা নির্ভর চৌম্বকীয়করণ পরিমাপ করা হয়েছে। তাত্ত্বিক বিশ্লেষণের জন্য Law of Approach পদ্ধতি প্রয়োগ করা হয়েছে এবং সেই সাথে চৌম্বকীয় ক্যালোরিক রেফ্রিজারেশন প্রয়োগের জন্য আপেক্ষিক শীতলকরণ শক্তি নির্ণয়ের জন্য চৌম্বকীয় এনট্রপির পরিবর্তন পরিমাপ করা হয়েছে। অপটিক্যাল বৈশিষ্ট পরিমাপ ব্যবহার করে, প্রতিসরাঙ্ক (n) এবং extinction coefficient (K) নির্ণয় করার জন্য Kramers-Kroning (K-K) পদ্ধতি প্রয়োগ করা হয়েছে । উচ্চ ফ্রিকুয়েন্সি প্রয়োগ বোঝার জন্য Impedance Analyzer দ্বারা Initial permeability বর্ণালী ২০ থেকে ১০ মেঘা হার্জ পর্যন্ত নেয়া হয়েছে । Impedance Analyzer ডাটা ব্যবহার করে ডাইইলেকট্রিক, ডাইইলেকট্রিক লস ট্যানজেন্ট এবং এসি কনডাকটিভিটি পরিমাপ করা হয়েছে । Impedance ডাটা থেকে complex impedance এবং modulus spectrum নির্ণয় করা হয়েছে , সেই সাথে Z-sim সফটওয়ার ব্যবহার করে grain এবং grain boundary প্যারামিটার Rg, Rgb, Cg, Cgb এর তাত্ত্বিত বিশ্লেষণ করা হয়েছে ।

Table of Contents

Declaration of Candidate		I
Declaration of Supervisor		IV
Acknowledgment		V
Abstract		VI
বিমূর্ত		VII
Table of Contents		VIII
List Figures		XIII
List Tables		XVI
Chapter 1:	**INTRODUCTION**	Page: 1
1.1	Background	2
1.2	Aims and Objectives	4
1.3	Thesis Outline	6
Chapter 2:	**LITERATURE REV**	**Page: 7**
2	General	8
2.1	Theoretical Background	8
2.1.1	Ferrites	8
2.1.2	Classification	8
2.1.3	Soft Ferrite	8
2.1.4	Hard Ferrite	8
2.2	Spinel Ferrite	8

2.3	Tetrahedral Sites	9
2.4	Octahedral Sites	10
2.5	Spinel Ferrite According to Cation Distributions	11
2.6	Cation's Magnetic Moment	12
2.7	Applications of Ferrite	12
2.8	Hysteresis and Magnetism	12
2.9	Magnetic Domain Behavior with Particle Size	13
2.10	Magnetic anisotropy	14
2.11	Curie PointTemperature	15
2.12	Magnetocaloric Effect	15
2.13	Rietveld Refinement	16
2.14	Optical Properties	17
2.15	Elastic Properties	18
2.16	Dielectrics	18
2.16.1	Dielectric Properties	18
2.16.2	Dielectric Polarization	18
2.16.3	Complex Dielectric Constant	19
2.16.4	Dielectric Loss Tangent	19
2.16.5	Frequency Dependent Dielectric Constant	20
2.16.6	Modulus Spectroscopy	21
2.16.7	Impedance Spectroscopy	21
2.16.8	AC Conductivity	22
2.17	Previous Work	22

Chapter 3: MATERIALS AND METHODOLOGY Page: 25

3.1	Synthesis of Nanoparticles and Bulk ferrite Preparation	26
3.2	Structural Analysis	27
3.2.1	X-ray Diffraction and Parameters	27
3.2.2	Crystallite Size Analysis	31
3.2.3	FTIR and Elastic Properties Analysis	31
3.3	Scanning Electron Microscope	33
3.4	Optical Properties Measurement	34
3.5	Magnetic Property Analysis	35
3.6	Impedance Analyzer	37
3.6.1	Complex Initial Permeability Measurement	37
3.6.2	Dielectric Measurement	38
3.6.3	Electric Modulus Analysis	39
3.6.4	Impedance Analysis	39
3.6.4	AC Conductivity Analysis	39

Chapter 4: RESULTS AND DISCUSSION **Page: 40**

4	General	41
4.1	XRD Analysis	41
4.1.1	Structural Properties	41
4.1.2	Rietveld Refinement	43
4.1.3	Crystallite Size and Strain	44
4.1.4	Cation Distribution and Crystal Shape Formation	47
4.1.5	Electron Density Method	48
4.2	Surface Morphology	52
4.3	Optical Properties	53
4.4	FTIR and Elastic Properties Analysis	54
4.6	Magnetic Properties	60
4.6.1	Magnetic Hysteresis	60
4.6.2	Temperature-dependent Magnetization and Curie Point.	63
4.6.3	Magnetocaloric Effect	64
4.6.4	Complex Initial Permeability	65
4.6.5	Quality Factor	66
4.7	Dielectric Properties	67
4.7.1	Complex Dielectric Constant	67
4.7.2	Dielectric Loss Tangent	70
4.7.3	Electrical Modulus Analysis	70
4.7.4	Impedance Analysis	71
4.7.5	Cole-Cole Plot	72

4.7.6 AC Conductivity 74

Chapter 5: CONCLUSIONS **Page: 76**

5.1 General 77

5.2 Key Findings 77

Limitations of the Study 78

Partial Implication 78

Recommendation for Further Study 78

Bibliography 79-84

List of Figures

Fig No.	Figure Caption	Page No.
2.1	FCC lattice Tetrahedral (A) and Octahedral (B) sites	9
2.2	FCC lattice A sites	10
2.3	FCC lattice B sites	10
2.4	Magnetic hysteresis loop	12
2.5	Coercivity with size of magnetic particle	13
2.6	Easy and hard direction of magnetization.	14
2.7	The Curie temperature of Ferromagnetic materials.	15
2.8	Magnetocaloric effect	16
2.9	Frequency Dependence Polarizability	18
3.1	Diagram of $Ni_{0.65}Cd_{0.35}Fe_{2-x}Al_xO_4$ bulk ferrite specimen preparation process	26
3.2	Bragg's X-ray diffraction mechanism	27
3.3	FTIR , (PerkinElmer) Postgraduate lab, Physics, CUET	31
3.4	Scanning Electron Microscope, MIST, Dhaka.	34
3.5	UV-vis Spectrometer Lambda 365, Physics,	35
3.6	Physical Property Measurement System (Atomic energy commission, Dhaka.	36
3.7	Impedance Analyzer Wayne Kerr 6500B	37
4.1	Rietveld refinement of XRD data of $Ni_{0.65}Cd_{0.35}Fe_{2-x}Al_xO_4$ bulk ferrite	43

4.2	Crystallite size determination of $Ni_{0.65}Cd_{0.35}Fe_{2-x}Al_xO_4$ bulk bulk ferrite by modified Scherrer's Approach	44
4.3	Crystallite size determination of $Ni_{0.65}Cd_{0.35}Fe_{2-x}Al_xO_4$ bulk bulk ferrite by Williamson-Hall Method.	45
4.4	Crystallite size determination of $Ni_{0.65}Cd_{0.35}Fe_{2-x}Al_xO_4$ bulk ferrite by Size Strain Method.	46
4.5	Crystal shape (a-b) as space filling and (c-d) as polyhedral	47
4.6	Fill contour 2D representation of $Ni_{0.65}Cd_{0.35}Fe_{2-x}Al_xO_4$ bulk ferrite.	49
4.7	3D representation of $Ni_{0.65}Cd_{0.35}Fe_{2-x}Al_xO_4$ bulk ferrite.	50
4.8	SEM images of $Ni_{0.65}Cd_{0.35}Fe_{2-x}Al_xO_4$ bulk ferrites.	52
4.9	Optical Absorbance and Reflectance of $Ni_{0.65}Cd_{0.35}Fe_{2-x}Al_xO_4$ bulk ferrites	53
4.10	Curves of (a) n Vs λ , and (b) k vs. hν for $Ni_{0.65}Cd_{0.35}Fe_{2-x}Al_xO_4$ bulk ferrite using K-K model.	54
4.11	FTIR spectra of $Ni_{0.65}Cd_{0.35}Fe_{2-x}Al_xO_4$ bulk ferrite.	55
4.12	Variation of (a) force constant (b) stiffness constant with of $Ni_{0.65}Cd_{0.35}Fe_{2-x}Al_xO_4$ bulk ferrites.	57
4.13	Changes of Elastic Modulii (B, G and E) with Al content.	58
4.14	Changes wave velocities (V_l, V_t ,V_m) of Al content in $Ni_{0.65}Cd_{0.35}Fe_{2-x}Al_xO_4$ bulk ferrite.	58
4.15	Debye temperature (θ_D) variation of $Ni_{0.65}Cd_{0.35}Fe_{2-x}Al_xO_4$ bulk ferrites.	59
4.16	(a) Hysteresis loops and (b) LAS fitted curves of $Ni_{0.65}Cd_{0.35}Fe_{2-x}Al_xO_4$ bulk ferrites.	60

4.17	(a) Magnetic moment with Al and (b) Canting angle effect with saturation magnetization.	61
4.18	(a) Temperature dependent Magnetization (M) and (b) The inverse of susceptibility with T of $Ni_{0.65}Cd_{0.35}Fe_{2-x}Al_xO_4$ bulk ferrites.	63
4.19	The magnetic entropy changes depending with temperature.	64
4.20	Demonstrates (a) the real portion and (b) imaginary portion of the complex initial permeability.	65
4.21	Demonstrates (a) the real portion and (b) imaginary portion of the dielectric.	67
4.22	Fitted curve of modified Debye equation of dielectric constant.	69
4.23	Reveals tanδ variation with frequency.	70
4.24	Changes of (a) the real portion and (b) imaginary portion of modulus.	70
4.25	Demonstrates (a) the real portion and (b) imaginary portion of impedance.	71
4.26	Cole-Cole fitted plot of $Ni_{0.65}Cd_{0.35}Fe_{2-x}Al_xO_4$ bulk ferrites	72
4.27	AC conductivity with frequency	74
4.28	Fitting to Jonscher's Law of AC conductivity	75

List of Tables

Table No.	Table Caption	Page No. 42
4.1	Structural parameters from XRD	42
4.2	Various parameters structural parameters from XRD	42
4.3	Fitting parameters for Ni-Cd-Al bulk ferrite.	43
4.4	Crystallite size "D" and Strain using the Scherrer's formula Williamson-Hall plot and Size-Strain Plot.	46
4.5	A sites and B sites cation distribution of $Ni_{0.65}Cd_{0.35}Fe_{2-x}Al_xO_4$ bulk ferrites.	47
4.6	Electron distribution densities of $Ni_{0.65}Cd_{0.35}Fe_{2-x}Al_xO_4$ bulk ferrites.	51
4.7	Inter atomic cation-cation and cation-anion bond length.	56
4.8	Bond angles of $Ni_{0.65}Cd_{0.35}Fe_{2-x}Al_xO_4$ bulk ferrites.	56
4.9	Absorption wave number (ν_1, ν_2), force constant (K), stiffness constant (C_{11}), and elastic constant (B, G, E) of NCA.	57
4.10	Wave velocities, Poisson ratio (σ), and Debye temperature (θ_D) of $Ni_{0.65}Cd_{0.35}Fe_{2-x}Al_xO_4$ bulk ferrites.	59
4.11	Magnetic parameters	61
4.12	Theoretical dielectric fitting parameters of $Ni_{0.65}Cd_{0.35}Fe_{2-x}Al_xO_4$ bulk ferrites.	69
4.13	Grain and grain boundary parameters of $Ni_{0.65}Cd_{0.35}Fe_{2-x}Al_xO_4$ bulk ferrites.	73

LIST OF SYMBOLS AND ABBREVIATIONS

XRD	X-Ray Diffraction
ρ_B	Bulk density
ρ_x	X-ray density
a	Parameter of lattice
F(θ)	Nelson-Riley function
P_{intra}	Intra-granular porosity
P_{inter}	Inter-granular porosity
SEM	Scanning Electron Microscopy
M_S	Saturation magnetization
FWHM	Full width at half maximum
K	Anisotropy constant
tanδ	loss factor or loss tangent
μ_B	Magnetic moment in Bohr magneton.
μ	Permeability
Q	Quality Factor
μ''	Imaginary part of the complex permeability
χ	Magnetic Susceptibility
ε"	Imaginary part of the dielectric constant
H_c	Coercive force
D	Size of grain
Φ	Magnetic Flux
B	Magnetic induction
H	Magnetic field
M_r	Remanent magnetization
λ	X-ray wave length
(hkl)	Miller Indices
μ'	Real part of the complex permeability
ε'	Real part of the dielectric constant

CHAPTER 1

INTRODUCTION

Chapter 1: INTRODUCTION

1.1 BACKGROUND

The magnetic ceramic compound like oxide ferrite materials which is a combination of major iron oxide and one or more additional metal having moderate characteristics as well as high resistivity [1]. Right now, the most promising materials for nanotechnology are spinel ferrites. The chemical equation AB_2X_4 represents the cubic spinel structure, where X represents the anions, A tetrahedral sites and B octahedral sites. Ferrites are distinguished as soft and hard ferrites [2]. Spinel structure known as face centered cubic crystal is formed by the combination of eight A sites and sixteen B sites occupied by cations only out of available 64 A sites and 32 B sites. A spinel ferrites unit cell is made up of 32 oxygen anions, 8 divalent cations, and 16 trivalent cations. Two interstitial spaces in the spinel structure are occupied by metal cations with oxygen coordination on their B and A atoms [2-3]. Which magnetic ions are present on the A and B sites, as well as the relative concentration of the inter (JAB) and intra-sublattice (J_{AA}, J_{BB}) exchange contracts, control the magnetic characteristics of spinel ferrites [4]. A substantial amount of iron (Fe) combined with minute amounts of metallic metals like Aluminium (Al), Lanthanum (La), Gadolinium (Gd) and Holmium (Ho) shows unique properties having potential applications [5-6]. However, rather than nanoparticles, a high density solid is needed for many electronic applications [7]. Optical materials with spinel structure are thought to be very advantageous for solar energy applications. Soft spinel ferrites are magnetic materials with substantial technical applications that are widely employed in a variety of fields . Due to their fabrication moderate optical, superior magnetic and microwave capabilities spinel type of ferrites are a good competitor for device [8-9], magnetic read-write head cores for fast digital tape or disk recording [10], microwave absorbers and magnetostrictive [6]. MRI, thermotherapy and biotechnological applications, satellite communication, transformers, memory storage device [11]. Making multilayer ferrite chip components is crucial for the downsizing of several devices in the fields of electronic device and energy storage appliances.

Among the aforementioned technological applications of ferrite, magnetic refrigeration is seen as an ideal technology to replace conventional refrigeration technology due to its potential impact on environmental issues and energy savings [12]. The effects of substitution on the structural and magnetic characteristics of Ni-based bulk ferrite investigated by researcher. The impact of Al substitution on the structural and magnetic characteristics of various ferrites examined by numerous researchers. Effect of lightly Al doping also raises the saturation magnetization, magnetic and optical characteristics. Due to its inert gas (trivalent) behaviour the structural, magnetic and optical properties i.e. offers interest to the scientific community [1-2, 5].

Nath et al. [4] observed the maximum magnetic moment in $Ni_{1-x}Cd_xFe_2O_4$ for x = 0.35. So, we chosen $Ni_{0.65}Cd_{0.35}Fe_{2-x}Al_xO_4$(NCA) ($0 \leq x \leq 0.060$) series to prepare dense ferrites with specific Ni and Cd composition to explore the structural, magnetic, magnetocaloric and optical properties.

Mannan et al. [1] observed an enhancement of magnetic moment and saturation magnetization (Ms) with Al content up to x = 0.030. Such enhancement of magnetic properties observed in $Ni_{0.4}Cu_{0.2}Zn_{0.4}Al_xFe_{2-x}O_4$ [5], as well as the improvement of magnetic properties in $Co_{0.425}Mn_{0.425}Zn_{0.150}Al_xFe_{2-x}O_4$ [13], $Cu_{0.65}Zn_{0.35}Al_xFe_{2-x}O_4$[14] and decrease the Curie temperature and grain size in $CoFe_{2-x}Al_xO_4$[15], $ZnFe_{2x}Al_xO_4$[16], $Co_{0.5}Zn_{0.5}Al_xFe_{2-x}O_4$[17], $Ni_{0.4}Zn_{0.5}Co_{0.1}Al_xFe_{2-x}O_4$[18], $Ni_{0.50}Co_{0.50}Al_xFe_{2-x}O_4$[19] also studied optical study and found increasing band gap $CoFe_{2-x}Al_xO_4$ [20].

Magnetic refrigeration relies on the magnetocaloric effect (MCE). Magnetic materials exhibit this behavior due to changes in alignment of magnetic moments when subjected to an applied magnetic field. The use of MCE based magnetic refrigeration technologies has led to much research into these materials. A magnetic system's MCE is extremely strongly tied to its magnetic behavior near its TC. It will also provide an in-depth insight of the microscopic process of MCE near phase transitions since at this critical temperature the material converted from ferromagnetic to paramagnetic. Since this is operating temperature of the refrigerator one expects at maximum entropy change, this is a important parameter as far as applications are concerned. A fundamental understanding of their magnetic and magnetocaloric properties is necessary to utilize them for applications in the field of magnetic refrigeration [12].

Having investigated the magnetic properties of Ni based ferrites, it is thought that the MCE properties of these compounds would be fascinating which has carried out with a view to finding out the prospective of these materials as magnetic refrigerants. Khan et al. [21] examined Ni-Cu-Cd spinel ferrite Bulk Ceramics for MCE. They found RCP values from (53.82 - 37.79) Jkg^{-1} at applied magnetic field of 3T. The impact of Al dope on the dielectric and the loss tangent decreased as well as conduction mechanism was observed of the spinel ferrite NiCdAl [22], NiCuCdAl [1], NiCuZnAl [23] , NiCoZnAl ($0 \leq x \leq 0.12$) [24], and CoZnAl [14].

Hence, the scientific community encouraged investigating the structural, magnetic magnetocaloric and optical effect in these kinds of magnetic materials due to the potential applications and their remarkable capacity to rotate their electromagnetic properties by non-magnetic materials. The structural and magnetic with magneto-caloric properties of spinel ferrites is the subject of extensive investigation now-a-days, with non-magnetic Al content being used as light substitution. The aim of this current study to prepare NCA spinel ferrite nanoparticles by using sol gel method and subsequent dense specimen ferrites to study the effect of Al substitution on the structural, magnetic , MCE , optical dielectric and electric properties of bulk NCA compound.

1.2 AIMS AND OBJECTIVES

NCA are selected to fabricate bulk ferrite through sol-gel auto-combustion method that to enhance materials properties to modify magnetic and electrical properties including possess low magnetic losses, low dielectric loss, high resistive, easy and ecofriendly materials are suitable for various electromagnetic device applications including microwave absorbers and magnetic cores in power converters, offer good magnetic permeability and low losses as well as good χ^2 fitting value by using Rietveld Refinement technique. The material's coercivity, permeability, and other magnetic properties may be tailored to fit particular requirements by replacing Fe with Al in the ferrite structure.

The main objectives of the present research are as follows:

- To synthesis of $Ni_{0.65}Cd_{0.35}Fe_{2-x}Al_xO_4$($x = 0, 0.015, 0.03, 0.045, 0.06$) ferrite nanoparticles and dense bulk disc and toroid shape specimen are prepared by sintered at 1150 ˚C.

- Structural characterization of various compositions is executed by X-ray diffraction (XRD). Density and porosity are found form the XRD results.
- Study of the surface morphology and estimation of grain size is carried out by SEM.
- Magnetic hysteresis parameters like M_S, H_c , M_r are observed using Physical Properties Measurement System (PPMS).
- Initial permeability spectra is investigated of prepared compound for all compositions.
- Frequency dependent dielectric and electrical properties, dielectric constant, ac conductivity, impedance spectra and modulus spectra (Cole-Cole plot) are investigated of all composition.

Possible outcome of the research is as follows

Homogeneous nanocrystalline powders are forecasted to facilitate the preparation of bulk ferrites. The preparation of bulk specimen at lower sintering temperature with optimum densities and superior quality materials is of significant interest, especially regarding their microstructures, initial permeability, saturation magnetization, optical, electric and dielectric properties, along with grain and grain boundary resistances analysis. Scientists and technologists have successfully applied the findings to manufacture an array of devices utilizing these ferrites.

1.2 THESIS OUTLINE

Chapter 1: The "*INTRODUCTION*" express an overview of the research related to the problem statement is presented, along with the justification for the investigation, the objectives and scope of the study, and the anticipated outcomes.

Chapter 2: The "*LITERATURE REVIEW*" chapter explored the theoretical basis of the current research paradigm and included review of various works that have been published in the past.

Chapter 3: The "*MATERIALS AND METHODOLOGY*" chapter details the synthesis of the prepared samples and offers a brief summary of different characterization techniques, including X-ray Diffraction (XRD), Magnetic properties, UV-Vis spectroscopy, FTIR Spectroscopy , Impedance Spectroscopy.

Chapter 4: The "*RESULTS AND DISCUSSION*" chapter, the outcomes of the investigative work are presented and interpreted in relation to existing theoretical frameworks.

Chapter 5: The "*CONCLUSIONS*" chapter insights from the overall experimental data are highlighted, accompanied by suggestions for additional studies.

In conclusion, here is a concise compilation of conferences and publications associated with the ongoing research.

CHAPTER 2

LITERATURE REVIEW

Chapter 2: LITERATURE REVIEW

2 GENERAL

This section provides an extensive summary of the research, detailing the main theories of the thesis, which will be discussed further in the literature review.

2.1 Theoretical Background

2.1.1 FERRITES

Ferrites are characterized as non-conductive ceramic compounds that exhibit ferrimagnetic properties. It typically originates from Fe oxides like Fe_3O_4 or Fe_2O_3 along with other metal oxides [1].

2.1.2 CLASSIFICATIONS

Depending on different attributes, ferrites can be divided into multiple categories. Ferrites are categorized into two groups according to their magnetic coercivity [25].

2.1.3 SOFT FERRITES

Soft ferrites can be easily magnetized and demagnetized. This evidently demonstrates that soft ferrites possess high magnetization and low coercive field. Soft ferrites, owing to their high magnetic permeability and minimal coercivity, are extensively utilized in electronics as effective magnetic cores for high-frequency applications such as inductors, transformers, microwave components and EMI filters [26].

2.1.4 HARD FERRITES

Ferrites are resistance to demagnetization, are utilized as permanent magnets in various applications including electric motors, magnetic separators and loudspeakers, and where a robust and stable magnetic field is required [27].

2. 2 SPINEL FERRITES

Spinel ferrites, characterized by the general formula MFe2O4, are categorized according to cation arrangement into normal, inverse, and mixed structures. They go by the name cubic ferrites as well spinel is the most well-known ferrites family. These materials are perfect due to use at high frequencies of their high electrical resistance values and minimal eddy current losses. Ferrites' spinel structure was first identified by Bragg and Nishikawa as represented by the mineral spinel $MgAl_2O_4$ in 1915 [28-30].

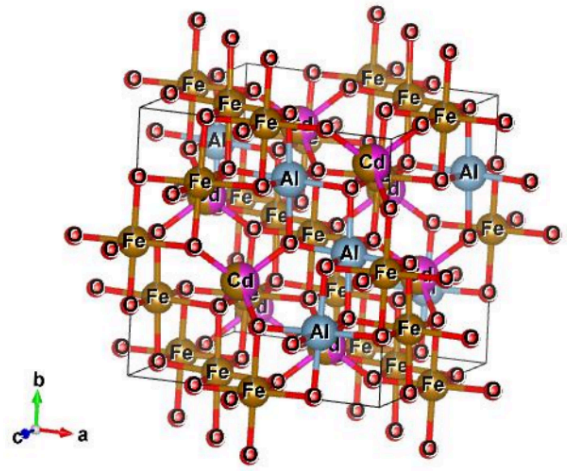


Fig. 2.1: FCC lattice Tetrahedral (A) and Octahedral (B) sites.

It has a common chemical formula of MFe_2O_4, where M is one of the divalent metal ions Ni^{2+}, Cd^{2+}, Co^{2+}, Zn^{2+}, Mg^{2+}, or a mixture of these ions. Spinel ferrites have a unit cell known as FCC that contains eight formula units. The equation is $M_8Fe_{16}O_{32}$. The largest ions are anions, which also form an FCC lattice. The metallic cations are present in two different sorts of interstitial places within these lattices. The unit cell includes 96 interstitial sites, including 64 tetrahedral (A) and 32 octahedral (B) sites. Fig. 2.1 is shown FCC lattice tetrahedral (A) and octahedral (B) sites of spinel ferrites

2.3 TETRAHEDRAL SITES

The interstitial is located in the center of a tetrahedron made of four lattice atoms in the tetrahedral (A) site. Three anions are on a plane, touching one another. In the middle of the three anions, the fourth anion is positioned symmetrically on top. These four anions form a vacuum, where the cation is located. The tetrahedral arrangement involves a cation occupies cube's body center and four anions filling four corners of the cube. Anions A, B, and C form a triangle in the plane, with anion D above the center. The cation fills the space left vacant middle of the cube. In the FCC crystal structure, only 8 of the 64 tetrahedral (A) sites are occupied by cations, ensuring charge neutrality. In the FCC lattice, the tetrahedral position is depicted in Fig. 2.2

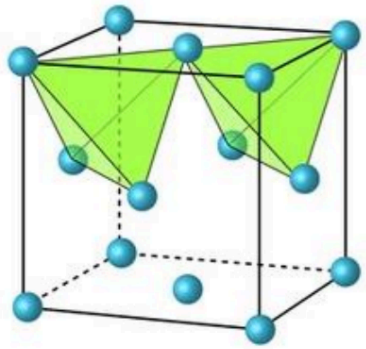


Fig. 2.2 : FCC lattice A sites [31].

2.4 OCTAHEDRAL SITES

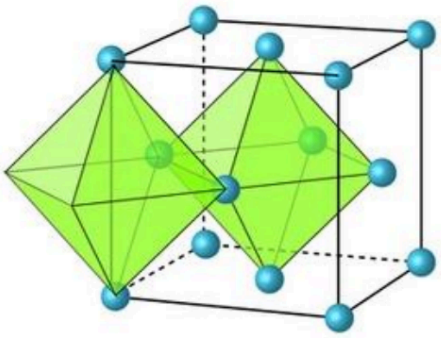


Fig. 2.3 : FCC lattice B sites [31].

The interstitial is located in the core of an octahedron made of six lattice anions at an octahedral (B) site. The plane is made up of four anions that are in contact with each other, and two additional anions that are symmetrically positioned above and below the center of the plane. Six anions form an octahedral shape, and the cation fills the space left behind.

2.5 SPINEL FERRITES ACCORDING TO CATION DISTRIBUTION

The positioning of cations at the A and B sites has made it possible to classify spinel ferrites into three unique groups. These are listed in the following order:

a) Normal spinel structure b) Inverse spinel structure

c) Mixed spinel structure

2.5.1 NORMAL SPINEL

In this type of spinel ferrites configuration, all Me^{2+} ions are presents in A site. These ferrites have the structural formula $(Me^{2+})[Fe_2^{3+}]O_4^{2-}$. Zinc ferrites $(Zn^{2+})[Fe_2^{3+}]O_4^{2-}$ exhibit this type of distribution. The illustration below shows the distribution within the typical spinel structure.

(A) [B]

$(Me^{2+})\ [Fe_2^{3+}]\ O_4^{2-}$

2.5.2 MIXED SPINEL

When cations Me^{2+} and Fe^{3+} occupy both A and B sites, the spinel structure is said to be mixed. The composition of like ferrite represent as $(Me_{1-\delta}^{2+}Fe_{\delta}^{3+})[Me_{\delta}^{2+}Fe_{2-\delta}^{3+}]O_4^{2-}$, wherever δ represents the degree of inversion. $MnFe_2O_4$ is type of mixed spinel and its structure stands $(Mn_{0.80}^{2+}\ Fe_{0.2}^{3+})[Mn_{0.2}^{2+}Fe_{1.8}^{3+}]\ O_4^{2-}$.

(A) [B]

$(Me_{1-\delta}^{2+}\ Fe_{\delta}^{3+})\ [Me_{\delta}^{2+}Fe_{2-\delta}^{3+}]\ O_4^{2}$

2.5.3 INVERSE SPINEL

All of the Me^{2+} are in B-positions in the inversed spinel structure. The distribution of Fe^{3+} ions between the tetrahedral (A) and Octahedral (B) sites is equal. These ferrites have the structural formula is $(Fe^{3+})\ [Me^{2+}Fe^{3+}]O_4^{2-}$. $NiFe_2O_4$, $CoFe_2O_4$, and magnetite Fe_3O_4 all have an inverse spinel structure [30]. One half of the Fe^{3+} is positioned in the B-sites and the rest of half in the A-sites in the inversed ferrites.

(A) [B]

$(Fe^{3+})\ [Me^{2+}Fe^{3+}]\ O_4^{2-}$

2.6 CATIONS' MAGNETIC MOMENT

The orbital and spin movements of electrons in an atom's incomplete subshell are proportional to the magnetic moment of a free atom.The magnetic moment associated with a cation is established by the number of its unpaired electrons. The spin-only magnetic moment of an atom, ion, or molecule is represented by the symbol $\mu = n\sqrt{(n+2)}$, here n stands for the number of unpaired electrons [25].

2.7 APPLICATION OF SPINEL FERRITES

Spinel ferrites, owing to their distinctive magnetic and electrical characteristics, are utilized in various fields such as energy storage, electronics, biomedicine, and encompassing data storage, environmental remediation, catalysts, drug deliver and sonsors [32-34].

2.8 HYSTERESIS AND MAGNETISM

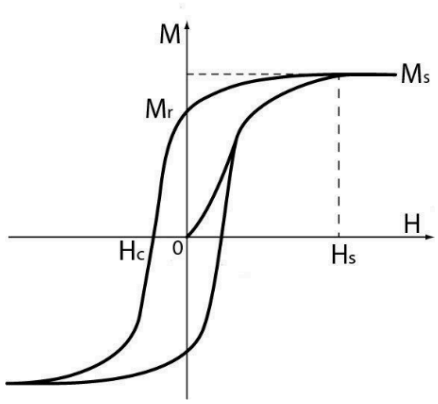


Fig. 2.4 Magnetic hysteresis loop [35].

A magnetic substance fails to return to a zero magnetization state after the removal of the applied magnetization. To bring it back to zero, a negative magnetic field must be introduced. When subjected to an alternating magnetic field, the magnetization of the material will exhibit a characteristic known as a hysteresis loop.

The graph in Fig. 2. 4 shows as an example of the typical relationship between magnetization and the applied magnetic field. The stability of magnetic domains contained within the material correlates with the hysteresis loop. A substantial amount of energy is needed for the magnetic domains to return to their original orientation following a change. The magnetic memory attributes of iron oxides are notably useful for recording audio on tape and for the magnetic storage of data on computer drives. When a material is demagnetized, its spins are oriented randomly, leading to the cancellation of any associated magnetic fields and producing a net magnetic field of zero. The existence of multiple types of magnetic domains is a result of the lower energy configuration found in ferromagnetic materials. The phenomenon of magnetization flips is referred to as domain walls, situated at the borders between two domains. When a ferromagnetic material encounters an external magnetic field, the domains within the material increase in size at the boundary of the neighboring domain, which is oriented roughly perpendicular to the applied field. This event is described as the motion of the domain wall.

2.9 MAGNETIC DOMAIN BEHAVIOR WITH PARTICLE SIZE

The coercive field H_c, a crucial characteristic of magnetic samples and which depends on the size of the particle to characterize the various magnetic regimes, can be used to demonstrate the importance of the particle size to its magnetic behavior. Fig. 2.5, which plots Hc against particle diameter, depicts this schematically.

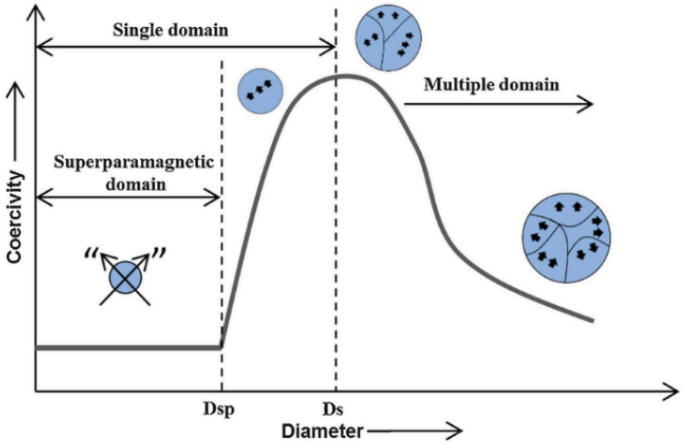


Fig 2.5: Coercivity with size of magnetic particle.

The graph shows four distinct regions [36]. Since the magnetic moment is unstable for very small dimensions, usually a few nanometers, Hc = 0 is reached below the superparamagnetic (Dcr spm) limit. For an intermediate diameter, the moment is steady, the particle is single-domain, and the coercivity increases with D (usually 20 nm <D<100 nm, due to a soft magnetic material). Finally, there may be an area where coercivity decreases because to vortex magnetic order, depending on the magnetic hardness. The multidomain regime enters for greater diameters, usually over several μm, and the coercivity decreases as diameter D increases.

2.10 MAGNETIC ANISOTROPY

Crystal anisotropy can be defined as the force that maintains the magnetization (Ms) in a crystal along specific equivalent crystallographic directions within the crystal. When the rotation process has finished, the domain wall vanishes, and the crystal becomes saturated. Because the external field has to perform work against the anisotropy force to rotate the magnetization vector from an easy direction, there has to be energy stored in any crystal where M_s is oriented in a non-easy direction.This is referred to as the crystal anisotropy energy E.

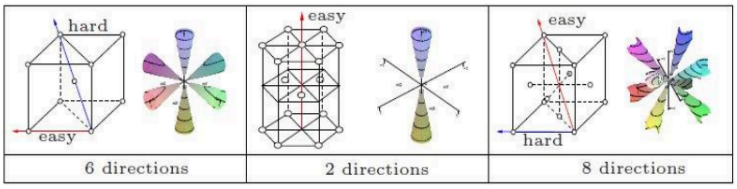


Fig 2.6: Easy and hard direction of Magnetization [37].

The Russian physicist Akulov demonstrated in 1929 that E can be represented through a series expansion of the direction cosines of Ms concerning the crystal axes.

In a cubic crystal, let Ms form angles a, b, c with the crystal axes, and let α_1, α_2, α_3 represent the cosines of these angles, which are referred to as direction cosines. Then,

$$E = K_0+K_1(\alpha_1^2\,\alpha_2^2+\alpha_2^2\,\alpha_3^2+\alpha_3^2\,\alpha_1^2) + K_2(\alpha_1^2\,\alpha_2^2\,\alpha_3^2)+\ldots. \quad (2.1)$$

where K_0, K_1, K_2,. . . are constants specific to a certain material at a specific temperature and are represented in J/m^3(SI).

Higher powers are typically unnecessary, and sometimes K_2 is so low that the related terminology can be overlooked. The initial term, K_0, does not depend on angle and is typically disregarded [37-38].

2.11 CURIE POINT TEMPERATURE

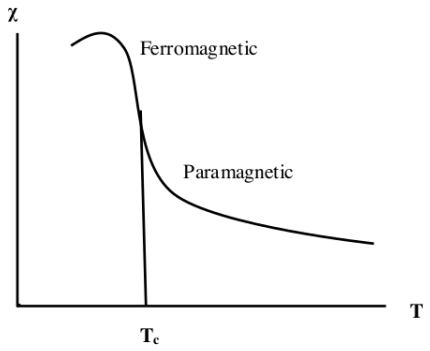


Fig. 2.7 The Curie temperature of Ferromagnetic materials.

The Curie temperature, referred to as the Curie point, is the temperature at which a ferromagnetic or ferrimagnetic material loses its lasting magnetic characteristics and transforms into a paramagnetic substance. Below the Curie temperature, adjacent magnetic spins orient parallel to one another in a ferromagnet without an external applied field. Above the Curie temperature, the magnetic spins are arranged randomly in a paramagnet unless a magnetic field is introduced [38].

2.12 MAGNETOCALORIC EFFECT

The magnetocaloric effect (MCE) refers to a scientific phenomenon wherein specific materials increase in temperature when subjected to a magnetic field. The heating occurs because of changes in the internal condition of the substance that is emitting heat. The magnetic moments (spins) in the material tend to align with the applied magnetic field. This alignment reduces the magnetic entropy (S) because the system becomes more ordered. If the process is adiabatic, as the magnetic entropy (S) decreases, the lattice entropy or temperature must increase , so the material heats up.

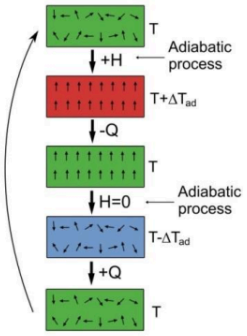


Fig. 2.8 : Magnetocaloric effect.

If the process is isothermal, heat is released to the surroundings to keep temperature constant as magnetic entropy (S) decreases. When the field is removed: The magnetic moments randomize. S increases (more disorder). In an adiabatic process, the material cools down as the total entropy stays constant [38-39].

2.13 RIETVELD REFINEMENT

Rietveld refinement is an important method utilized in the characterization of crystalline materials. The characterization of reflection-based patterns in X-ray diffracted powders can be optimized to yield precise parameters, including the height and width of peaks, as well as the locations of these reflections at different intensity values. The significance of these parameters is considerable in the context of numerous structural studies of materials. The Rietveld method employs a least squares approach to refine a line generated from the theoretical profile, contingent upon a close match between the measured and theoretical profiles [40]. The parameters that define the quality of refining are presented as follows.

2.13.1 GOODNESS OF FITTING

The primary parameter that indicates the success of the refining process is referred to as goodness of fit, denoted by the symbol $\chi 2$. The $\chi 2$ can be obtained through the use of the following formula;

$$\chi^2 = (\sum((Y_i^{obs} - Y_i^{calc})^2 / (n-p)) = Rwp/Rexp \quad (2.2)$$

2.13.2 PROFILE RESIDUAL

The dependability factor, also known as the profile residual, associated with a refining process can be defined as follows;

$$R_p = \sum(|Y_i^{obs} - Y_i^{calc}|/\sum^n Y^{obs})\times 100\% \quad (2.3)$$

Y_i^{obs} stand for the intensity profile that is observed, Y_i^{calc} correspond the profile intensity that is calculated at the i^{th} point, and in this context, n signifies the overall number of data points .

This generates the weighted residual profile;

$$R_{wp} = (\sum^n(\omega_i(Y_i^{obs} - Y_i^{cal})^2 / \sum^n \omega_i (Y^{obs})^2)^{1/2}\times 100\% \quad (2.4)$$

For where the weight is ω_i. The characteristics of the Bragg residual profile are outlined as follows;

$$R_B = \sum(|I_j^{obs} - I_j^{calc}|/\sum^n I^{obs})\times 100\% \quad (2.5)$$

The integrated intensities of the j^{th} observed and measured Bragg peak are denoted by I_j^{obs} and I_j^{calc}, respectively. The predicted residual profile can be found using;

$$R_{exp} = ((n-p) / \sum^n \omega_i (Y^{obs})^2)^{1/2}\times 100\% \quad (2.6)$$

where the phase is indicated by p.

2.14 OPTICAL PROPERTIES

UV-Vis spectroscopy is an analytical method utilized to quantify the specific wavelengths of ultraviolet or visible light that are either absorbed by or transmitted through a sample, in relation to a reference or blank sample. The characteristics of this property are affected by the composition of the sample, which can yield insights into its constituents and their respective concentrations. Given that this technique is based on light interaction, it is essential to first examine the properties of light. UV-visible (UV-Vis) spectrophotometers function by using a light source to illuminate a sample with light that covers the ultraviolet to visible wavelength spectrum, usually from 200 to 1100 nm. The instruments measure the light that is absorbed, transmitted, or reflected by the sample at each wavelength [41].

2.15 ELASTIC PROPERTIES

By measuring the absorption of infrared radiation, Fourier Transform Infrared (FTIR) Spectroscopy, a widely used analytical technique, identifies the presence and kind of functional groups in a sample. The method relies on generating a distinct spectral fingerprint by transmitting infrared radiation through a sample and analyzing the frequencies at which the sample absorbs [42]. Elastic properties including force constant, stiffness constant, elastic moduli, wave velocities and Debye temperature of Al substituted spinel ferrite can be studied using FTIR absorption data.

2.16 DIELECTRICS

Dielectric electrical insulators are characterized by the absence of free charge, with all atoms being held in place by their nearest neighbors. When an external electric field is applied, the centers of the electron clouds experience a slight displacement, resulting in the positive cores of the ions behaving as electric dipoles.

2.16.1 DIELECTRIC PROPERTIES

2.16.2 DIELECTRIC POLARIZATION

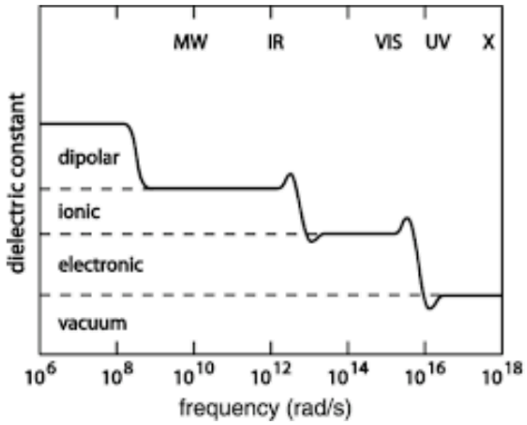


Fig. 2.9 : Frequency dependence polarizability [43].

2.16.3 COMPLEX DIELECTRIC CONSTANT

The definition of relative permittivity is the ratio of the capacitance of a capacitor containing a material (C) to that of a vacuum capacitor (C_0). This concept applies to both liquids and solids and is also referred to as the dielectric constant or specific inductive capacity. The insulating characteristics of electrical materials are highlighted by their significant dielectric properties at the atomic level, as opposed to exhibiting a consistent electrical behavior. The relation of dielectric constant as follows

$$\varepsilon' = \frac{C}{C_0} \tag{2.7}$$

In this context,

$$C_0 = \frac{\varepsilon_0 A}{d} \tag{2.8}$$

The dielectric constant is a parameter that reflects the extent to which a material can sustain polarization in the presence of an external electric field. There are four main types of polarizing sources: space charge, dipolar charge, atomic charge, and electronic charge. The two varieties mentioned last affect the microstructure of ferroelectric materials, while the first two types show no significant impact. A way to represent the frequency-dependent complex dielectric constant is as follows [43].

$$\varepsilon^* = \varepsilon' - j\varepsilon'' \tag{2.9}$$

The real aspect of the dielectric constant (ε') corresponds to the energy that is accumulated, while the complex aspect of the dielectric constant (ε'') pertains to the factor of energy dissipation. The equation indicated above combines these two terms. The following text describes their association with the capacitance measurements of capacitors.

$$C = \frac{C_p\, d}{\varepsilon_0\, A} \tag{2.10}$$

In this scenario, A is defined as the pellet's cross-sectional area, d is the thickness of the pellet, ε_0 is the free space permittivity, quantified as 8.854×10^{-12} $C^2N^{-1}m^{-2}$, and C_p denotes the capacitance of the pellet.

2.16.4 DIELECTRIC LOSS TANGENT

The dielectric loss tangent is characterized by the ratio of energy that is wasted compared to the energy that is consumed. This can be described as follows

$$\varepsilon'' = \varepsilon' \tan\delta \quad (2.11)$$

The dielectric loss tangent (tanδ) [42] is shaped by compositional factors such as structural homogeneity, stoichiometry, and the level of ferrous concentration. It is also reliant on the temperatures used during the sintering process.

2.16.5 FREQUENCY DEPENDENT DIELECTRIC CONSTANT

a) COMPOSITION

The ε′ in ferrites is determined by several microstructural and structural variables.

It has been found that the value of ε reduces as the aluminum content in Ni-Cd ferrites increases. In addition, Ni is associated with the B-sites, while Cd is associated with the A-sites. The ions Fe^{2+} and Fe^{3+} can occupy positions in both the A-site and the B-site. The substitution of a small fraction of Al with Fe^{3+} results in the conversion of some Fe^{3+} into Fe^{2+}, while maintaining the overall neutral charge.

b) FREQUENCY

The relationship between ε′ and frequency is contingent upon distinct polarizations. With an increase in frequency, ε′ tends to decrease, while at lower frequencies, it maintains a notably high value. Conversely, at higher frequencies, it becomes remarkably small, akin to being independent of frequency.

The two-layer framework articulated by Maxwell and Wagner [23] is a highly effective means of explaining the discrepancies in ε′. This theory indicates that the structure of dielectric materials is constituted by an insulating matrix or grain borders, in conjunction with the highly conductive phase or grains interspersed among them. The heterogeneous nature of the material has led to the formation of space charge polarization. When an external alternating current electric field is applied at the grain boundaries, it induces a local accumulation of charge.

The significant resistance at the grain border causes electrons to group together, which in turn produces polarization. The time it takes for space charge carriers to align with the alternating field is limited. Unfortunately, when the frequency of the reversing field increases, these carriers are unable to orient themselves in the direction of the electric field because of a shortage of charge carriers at the grain boundary. The flow of carriers is oriented in the opposite direction to that of the external field as a consequence.

As polarization diminishes due to a decrease in charges at the grain boundaries, the permittivity (ε′) similarly decreases. Consequently, an increase in the frequency of the field prompts space charge carriers to advance ahead of the reversing field, suggesting that dielectric materials do not facilitate polarization.

2.16.6 MODULUS SPECTROSCOPY

The complex electric modulus is a crucial approach for investigating the dielectric properties of polymeric insulators. It becomes particularly advantageous when high temperatures result in a more intricate permittivity. This increase in complex permittivity is primarily due to electrode polarization and the mobility of carriers.

As it is inversely related to complex permittivity, the complex electric modulus is effective for measuring dielectric properties at elevated temperatures. The complete complex electric modulus is comprised of its real component (M′) and its imaginary component (M″).

$$M^* = M' + jM'' \tag{2.12}$$

The following relationships between electric modulus and the dielectric constant for the real as well as imaginary portion of electric modulus such as

$$M' = \frac{\varepsilon'}{\varepsilon'^2 + \varepsilon''^2} = \omega C_0 X \tag{2.13}$$

and

$$M'' = \frac{\varepsilon''}{\varepsilon'^2 + \varepsilon''^2} = \omega C_0 R \tag{2.14}$$

Where C_0 defines geometrical capacitance equals to $\varepsilon_0 A / t$, where $\varepsilon_0 = 8.854\ 10^{-14}$ F/Cm is the free space permittivity [43-44].

2.16.7 IMPEDANCE SPECTROSCOPY

The effective resistance Z of dielectric materials can be calculated using the subsequent formula when they are exposed to an external alternating electric field,

$$Z = R + jX \tag{2.15}$$

where resistance and reactance denoted by R and X respectively. The complex impedance is created by the combination of resistance and its corresponding reactance. The resistance and reactance part of impedance can be calculated using the following formula,

R = Z′ = Rs and

$$X = Z'' = \frac{1}{\omega C_P} \quad (2.16)$$

where f is the frequency of the applied electric field [43-44].

2.16.8 AC CONDUCTIVITY

AC conductivity is a type of investigation conducted on solids to define the overall resistance of the crystalline sample. Measurement of alternating current conductivity can be carried out using various methods. The technique currently in use is the complex impedance spectroscopy. The relationship between conductivity and frequency is expressed by Eq. 2.17

$\sigma_{ac} = \varepsilon' \varepsilon_0 2\pi f \tan\delta$, Here, f denotes frequency [1] (2.17)

The total conductivity of the samples being examined can be regarded as the sum of both the direct current (DC) and alternating current (AC) components, represented as $\sigma = \sigma_{dc} + \sigma_{ac}$. The conductivity of direct current is mainly attributed to the excitation of electrons in localized states within the conduction bands.The conductivity arises from hopping conduction, in which electrons transfer charge by moving between octahedral cations. Across a wide range of frequencies, the theoretical behavior of the bulk ferrite can be fitted to Jonscher's power law, $\sigma = \sigma_{dc}(T) + A\omega^n$. The first term of $\sigma_{dc}(T)$ conductivity is independent of frequency and $A\omega^n$, the second term, is connected to pure ac conductivity, which varies with temperature and frequency, and is related to the dielectric relaxation resulting from localized charge carriers. The parameter 'n' provides details about the relationship between charge carriers and their surrounding environment. The value of n can be either above 1 or below 1, contingent upon the frequency range applied in the measurement of conductivity. When 'n' >0, the conduction is influenced by frequency. The variation from the n values greater than 1 is a result of multiple factors, such as the microstructural characteristics of the material, temperature, and its composition.

2.17 PREVIOUS WORK ANALYSIS

A brief overview of the influential literature that attribute this study is outlined in the following paragraphs. Various techniques are employed to prepare spinel ferrites, including co-precipitation, hydrothermal synthesis, solid-state reactions, and sol-gel auto-combustion. Many researcher investigated structural, magnetic and dielectric properties of Al substitute spinel ferrites using sol-gel approach. The same approach were utilized to prepare different spinel ferrites, like MnZn [45], NiMnCu [46], NiMgCo [47], NiBaCo [48], Li(NiCo) [49] and NiZnCo [50].

In general, this method employs metal nitrate salts as reactants and involves fuel for the auto-combustion reaction. The fuels are most commonly use including Citric acid [51], Amonia [52] and Uria and and glycine [7]. Ammonia is the best to other substances because it accelerates the reaction more effectively. While utilizing citric acid assists in reducing the surplus pollution from N_2 gas, it also decreases the speed of the reaction, which affects the prepared chemical. Because of its simplicity and low cost, this technology has primarily been recognized by the scientific community for the synthesis of ferrites [7]. However, Al substituted ferrites have been synthesized using solid state reaction methods in other research [53-54].

Many metal oxides are mixed using this technique through grinding and calcination to fabricate ceramic ferrites. It's challenging to regulate this mechanical mixing, and every preparation step has experienced variations that may persist after sintering. Additionally, the calcination process in this method requires high temperature, which may cause some metal ions to evaporate ultimately results in defects in the manufactured products. Co-precipitation is another method for producing spinel ferrite specimens CoMg [55], ZnAl [56], CoMnZn [57]. The hydrothermal method is the newest technique for producing nanoparticles $NiAl_xFe_{2-x}O_4$ [58]. In this process, the synthesis produces application of the hydrothermal effect. The cavity and additional instruments needed for this procedure are very expensive. Additionally, the operation is very risky because the generated molecule is frequently harmed because the generation is not realized promptly. The chemical synthesis method is expensive and necessitates numerous modes of operation that are time-consuming. On the other hand, sol-gel auto combustion has advantages over chemical methods because it requires inexpensive equipment, consumes less energy, and produces uniform, highly reactive, nanosized outcomes.

By replacing a small non-magnetic element, such as Al, the ferrite samples' structural, magneto-electric, and dielectric properties can be altered. This change can also affect the cation distribution and magnetocrystalline anisotropy. Relative coercivity changes in tandem with the inclusion of Al similar to the magnetocrystalline anisotropy. Al doped spinel ferrites have piqued interest lately due to their great electrical resistivity and low dielectric loss [59]. These characteristics are beneficial in microwave devices.

Khan et al. [21] were fabricated $Ni_{0.5-y}Mg_yCu_{0.2}Cd_{0.3}Fe_2O_4$ (NMCC) and observed magnetocaloric effect of NMCC bulk specimen. They were found RCP values in the range of 53.82 Jkg^{-1} to 37.79 Jkg^{-1}. The band gap has been discovered to range from 1. 4 to 1. 6 eV and is rising with the amount of Mg content.

Mohammed and Wahba [45] were prepared $Mn_{0.5}Zn_{0.5}Fe_{2-x}Al_xO_4$ and found the formation of a pure cubic spinel phase for the whole samples using FTIR analysis. They were also studied that Al substitution has improved the elastic properties of the Mn–Zn ferrites. Saturation magnetization was found to increase upto x = 0.10.

Nafees et al.[49] were fabricated $Li_{0.6}(NiCo)_{0.2}Al_xFe_{2.2-x}O_4$ using sol gel method. The lattice, X-ray density, bond lengths, and crystallite size parameters decline as the Al^{3+} concentration rises. With increasing Al^{3+} concentration, both the activation energy and the room temperature resistivity rise. The saturation magnetization was increased up-to x = 0.030 , then decreased with Al content.

Solyman et al.[55] were investigated using the co-precipitation method. They discovered that the crystallite size and magnetic properties reduced due to a rise in nonmagnetic Al^{3+} ions. As the anisotropy constant decreases with higher Al^{3+} concentration, it is observed that the magnetic permeability increases. The validation of the materials' nanocrystalline formation was provided by the reduction in crystallite size from 55 to 29 nm with Al^{3+} substitution. The dielectric properties of these generated nanoparticles show that they may be used in the production of electronic gadgets and the fabrication of high-frequency devices.

Wasnik et al.[59] were prepared $Ni_{0.5}Cu_{0.5}Al_xFe_{2-x}O_4$ using Microwave-assisted Sol-gel method. The average crystallite size calculated from XRD data showed a decrease from 45.21 nm to 37.34 nm with rising Al^{3+} substitution. It was discovered that the observed saturation magnetization (M_s) and coercivity (Hc) first rise until x = 0.04, then decreased with Al content.

Arrasheed et al. [60] $NiAl_xFe_{2-x}O_4$ was effectively synthesized using the flash auto combustion. They were analysed the FTIR spectra. They were found significant modification of the elastic and electrical proper due to the incorporation of Al content. The values of Debye temperature found to rises with the substitution of Al.

Rabil et al [61] $Ni_{1-x}Zn_xFe_2O_4$ was successfully synthesized using co-precipitation method, where x=0.4, 0.5, 0.6, and 0.7. At room temperature, they noted high resistivity values, minimal dielectric loss, and low dielectric constant. The Curie temperature was observed to drop from 619 to 350 K as x increased from 0. 4 to 0. 7. They were measured RCP values in the ranges of (90-97.9)Jkg^{-1}.

CHAPTER 3

MATERIALS AND METHODOLOGY

Chapter 3: MATERIALS AND METHODOLOGY

This chapter outlines the methods used in the experiments to prepare samples of Al-substituted NiCd dense ferrites. We also go over the methods for preaparing Ni-Cd-Al ferrites and the sintering procedure, which has the general formula $Ni_{0.65}Cd_{0.35}Al_xFe_{2-x}O_4$. The sample was prepared using the sol-gel process.

3.1 SYNTHESIS OF NANOPARTICLES AND BULK FERRITE PREPARATION

Initially analytical grade ingredients of $Ni(NO_3)_2.6H_2O$, $Fe(NO_3)_2.9H_2O$, $Cd(NO_3)_2.4H_2O$, $Al(NO_3)_2.9H_2O$ chemicals as precursors to synthesis $Ni_{0.65}Cd_{0.35}Fe_{2-x}Al_xO_4$(NCA) nanoparticles without further purification and all are collected from Sigma-Aldrich. Nanoparticles of Ni-Cd-Al bulk synthesized using the sol-gel auto-combusted method and Fig.1 shows the flow chart of synthesis procedure. The stoichiometric raw materials were dissolved in ethanol and combined to prepare a homogeneous solution. A magnetic stirrer used to agitate the solution continuously for homogeneous mixing and the pH of the solution kept at 7.

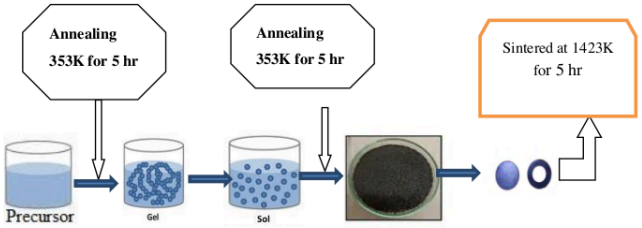


Fig. 3.1 Diagram of Ni-Cd-Al bulk ferrite specimen preparation process.

Liquid ammonia (NH_4OH) added and stirred vigorously. This combination placed in a hot water bath at 353 K and kept there until the gel formed at a constant temperature for 24 hr. The resulting gel heated at 523 K for 2 hr, then subjected to the self-ignition process to transform into a fluffy loose powder.

The ferrite powder was meticulously hand-milled for a period of 2hr to produce fine and uniform particles. The necessary amount of polyvinyl alcohol (PVA) has been utilized to granulate the powder effectively.The hydraulic press machine has been employed to compress the granulated ferrites, resulting in the formation of the required disc and toroid-shaped samples.The disc and toroid samples were subjected to a pressure of 600 psi for a duration of two minutes during the pressing process.Subsequently, the specimen was subjected to sintering at a temperature of 1423 K within the furnace for a duration of 5 hr. The samples underwent sanding with sandpaper to prepare them for the subsequent experiment.

3.2 STRUCTURAL ANALYSIS

3.2.1 X-RAY DIFFRACTION AND PARAMETERS.

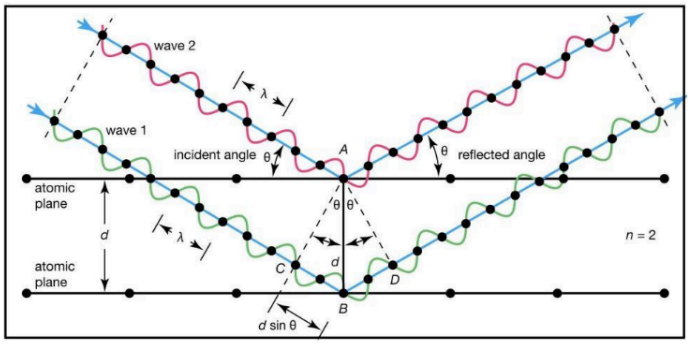


Fig. 3.2: Bragg's X-ray diffraction mechanism [62].

Structures were assessed using the Rietveld refinement method and Fullprof software from the experimentally obtained XRD data. During refining, the symmetry of the space group Fd-3m and the Pseudo Voigt peak form applied to each motif. Except for oxygen, all atoms are thought to have fixed atomic locations throughout the refinement process. As open parameters, the atomic scenarios are employed. The backdrop was also enhanced using the Pseudo-Voigt function.

Different settings were chosen for obtaining the best fitting as well as a good χ^2 value. After achieving the best fitting value, the structural parameters like lattice constant, electron density, cation distribution, and crystallite size. Additionally, each set traveled for analysis of the Electron Density Method (EDM). The results of the Rietveld refinement method were also used to find bond structures. For step size 0.015, the crystal structure was created using the VESTA software. The perpendicular distance (dhkl) of the adjacent of inter-planer spacing of (hkl) parallel plane calculated using the Bragg's relation, $d_{hkl} = (n\lambda/2\sin\theta)$ where the value of n is only for 1, which is the diffraction order. The interplaner spacing value and the related (hkl) parameters used to derive the lattice constant (a) for various spinel phases using following relation

$$a = d_{hkl}\sqrt{h^2 + k^2 + l^2} \quad (3.1)$$

In order to calculate the precise lattice constant for each sample, the Nelson-Riley extrapolation function was empployed [2] ,

$$F(\theta) = \frac{1}{2}\left(\frac{\cos 2\theta}{\sin\theta} + \frac{\cos 2\theta}{\theta}\right) \quad (3.2)$$

The X-ray(ρx) and experimental (ρB) density have computed applying following equations

$$\rho_x = \frac{8M}{a^3 N} \quad (3.3)$$

$$\rho_B = \frac{M}{\pi r^2 l} \quad (3.4)$$

where M and N stand for the samples' molecular weights and Avogadro's number and l, M and r stand for the thickness, masses and radius of samples respectively.

The following expression could be used to determine the density of dislocation[2],

$$\delta = \frac{1}{D^2} \quad (3.5)$$

The lattice strain (ε_{LS}), stacking faults (SF), the micro strain (Emicrstrain) and the surface area of compound could be computed using relations respectively [2]

$$\varepsilon = \frac{\beta}{4\tan\theta} \quad (3.6)$$

$$SF = \frac{2\pi^2}{45\sqrt{3}\tan\theta} \quad (3.7)$$

$$E_{micro} = \frac{\beta \cos\theta}{4} \quad (3.8)$$

$$S = \frac{6000}{\rho_x D} \quad (3.9)$$

Estimation of RMS strain calculated by using following equation [63].

$$\varepsilon_{rms} = \sqrt{\frac{2}{\pi}} \quad (3.10)$$

The ionic radii of the A and B sublattices can be determined by [2] ,

$$r_A = a\sqrt{3}(u - 0.25) - r_0 \quad (3.11)$$

$$r_B = a\,(0.625 - u) - r_0 \quad (3.12)$$

The ionic radii of A and B sites, as well as the bond lengths of A , (A - O) and B, (B - O) of each composition calculated using Standley's equations ,

$$A - O = a\sqrt{3}(u - 0.25) \quad (3.13)$$

$$\text{and, } B - O = a\,(0.625 - u) \quad (3.14)$$

where denotes the oxygen radius (1.32 Å) and u = 3/8 is the parameter of Oxygen [9].

The hoping length determined for A-A sites, A-B sites and B-B sites using the following equations [6, 64-65].

$$L_{A-A} = \frac{a\sqrt{3}}{4} \quad (3.15)$$

$$L_{A-B} = \frac{a\sqrt{11}}{8} \quad (3.16)$$

$$L_{A-B} = \frac{a}{2\sqrt{2}} \quad (3.17)$$

where a stands for the lattice constant

The B site edges for shared and unshared (d_{BL}) and (d_{BEU}) as well as the A site edge (d_{AE}) can be evaluated applying relations [65].

$$d_{BE} = a\sqrt{2}(1 - 2u) \quad (3.18)$$

$$d_{BL} = a\sqrt{(3u^2 - \frac{11u}{4} + \frac{43}{64})} \quad (3.19)$$

$$d_{BEU} = a\sqrt{(4u^2 - 3u + \frac{11}{16})} \quad (3.20)$$

$$d_{AE} = a\sqrt{2}(2u - \frac{1}{2}) \quad (3.21)$$

The cation-cation bond length (Me - Me) b, c, d, e and f can be calculated using ,

$$b = \frac{a\sqrt{2}}{4} \quad (3.22)$$

$$c = \frac{a\sqrt{11}}{8} \quad (3.23)$$

$$d = \frac{a\sqrt{3}}{4} \quad (3.24)$$

$$e = \frac{a3\sqrt{3}}{8} \quad (3.25)$$

$$f = \frac{a\sqrt{6}}{4} \quad (3.26)$$

The parameters p, q, r, s were used to measure the length of the cation-anion bond (Me - O) , where u is the oxygen positional parameter 0.375.

$$p = a\left(\frac{5}{8} - u\right) \quad (3.27)$$

$$q = a\sqrt{3}\left(u - \frac{1}{4}\right) \quad (3.28)$$

$$r = a\sqrt{11}\left(u - \frac{1}{4}\right) \quad (3.29)$$

$$s = a\sqrt{3}\left(\frac{u}{3} + \frac{1}{8}\right) \quad (3.30)$$

The bond angle values were derived from following equations

$$\theta_1 = \cos^{-1}\left(\frac{P^2+q^2-c^2}{2pq}\right) \quad (3.31)$$

$$\theta_2 = \cos^{-1}\left(\frac{P^2+r^2-e^2}{2pr}\right) \quad (3.32)$$

$$\theta_3 = \cos^{-1}\left(\frac{P^2-b^2}{2p^2}\right) \quad (3.33)$$

$$\theta_4 = \cos^{-1}\left(\frac{P^2+s^2-f^2}{2pf}\right) \quad (3.34)$$

$$\theta_5 = \cos^{-1}\left(\frac{r^2+q^2-d^2}{2qr}\right) \quad (3.35)$$

3.2.2 CRYSTALLITE SIZE ANALYSIS

The Scherrer's formula $D = \frac{K\lambda}{\beta\cos\theta}$ has been applied to estimate the crystallite size where D is the crystallite size, β represents for the whole width half maximum, θ for the diffraction angle of crystal, λ stands for the wavelength of the Cu-Kα radiation (1.5405 Å, X-ray diffractometer, PW3040, PANalytical), and K denotes for the form factor here used for cubic (0.9).

3.2.3 FTIR AND ELASTIC PROPERTIES ANALYSIS

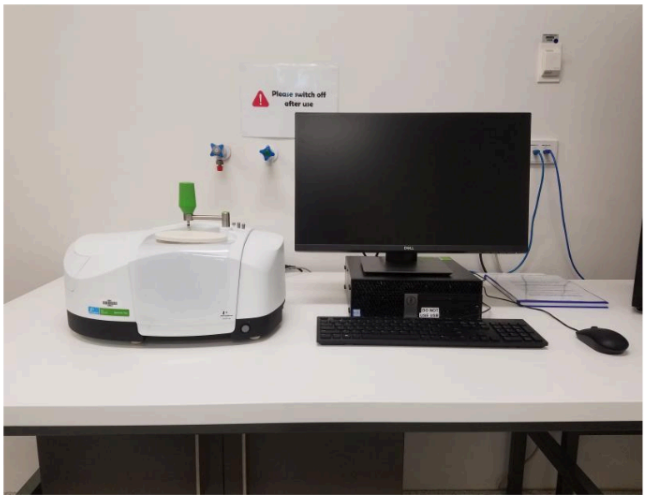


Fig.3.3 FTIR , (PerkinElmer, spectrum two) Postgraduate lab, Physics, CUET.

The absorption bands were recorded at room temperature using Fourier transform infrared spectroscopy (FTIR) (PerkinElmer, spectrum two).The ion force constants at the A and B sites (K_T and K_0) are associated with band frequencies of infrared (ν_A and ν_B) of the cations at the A and B sites. These can be written as follows:

$$K_T = 4\pi^2c^2\nu_1^2\mu \quad (3.36)$$

$$K_0 = 4\pi^2c^2\nu_2^2\mu \quad (3.37)$$

In this scenario, c is the symbol for the velocity of light, and μ represents the reduced mass, which we have derived from the following relationship, $\mu = \frac{m_1 m_2}{m_1 + m_2}$, here, the value of ($\mu$), representing the reduced mass, is computed in accordance with the distribution of cations, m_1 is defined as the weighted average of the atomic weights of the cations that occupy the A-site or B-site, while m_2 refers to the atomic weight of the oxygen anion [66, 68-69]. The stiffness constants C_{11} and C_{12} were measured [68] based on the following relation,

$$C_{11} = \frac{F_{av.}}{a} \quad (3.38)$$

$$C_{12} = \frac{\sigma C11}{(1-\sigma)} \quad (3.39)$$

In this context, ($F_{av.}$) represents the average force constant, calculated as

$$F_{av.} = \frac{(F_T + F_0)}{2} \quad (3.40)$$

The variable (σ) signifies Poisson's ratio, which is dependent on the pore fraction and is written as [70] $\sigma = \frac{(3B-2G)}{(6B+2G)}$ (3.41)

The different elastic moduli for cubic structures, which include Young's modulus (E), shear modulus (G), and bulk modulus (B), can be derived from the following formulas [45],

$$E = \frac{(C_{11}-C_{12})(C_{11}+2C_{12})}{(C_{11}+C_{12})} \quad (3.42)$$

$$B = \frac{1}{3(C_{11}+2C_{12})} \quad (3.43)$$

$$G = \frac{E}{2(\sigma+1)} \quad (3.44)$$

In the context of isotropic materials exhibiting cubic symmetry, such as spinel ferrites and garnets, C_{11} and C_{12} represent the components of the elasticity tensor. It is noteworthy that C_{11} is nearly equivalent to C_{12}, resulting in the relationship $B = C_{11}$ [2, 71]. The elastic wave velocities of the transverse (V_t), longitudinal (V_l), and the mean (V_m) were determined [45,71] through the application of the following equations,

$$V_l = \sqrt{\frac{C_{11}}{\rho_x}} \quad (3.45)$$

$$V_t = \frac{V_l}{\sqrt{\rho_x}} \quad (3.46)$$

$$V_m = \left[\frac{1}{3}\left(\frac{2}{V_t^3} + \frac{1}{V_l^3}\right)\right]^{\frac{-1}{3}} \quad (3.47)$$

The Debye temperature (θD), was calculated using the following equation [3]

$$\theta_D = \frac{\hbar c v_{av.}}{K_B} = 1.438 K_B \quad (3.48)$$

In this instance, $\nu_{av.}$ is the average wave number, ħ is identified as Planck's constant, KB denotes Boltzmann's constant, and C is the light speed. For ferrite materials, the value of ħC/KB is assumed to be 1.438 [3]. Thermal conductivity conductivity can be determined from the expression

$$K_{min} = K_B n^{\frac{2}{3}} \frac{(2V_l + V_t)}{2.48} \quad (3.49)$$

where Vm is the mean wave velocity, KB denotes Boltzmann's constant, n represent for number of atoms, and NA stands for Avogadro's number. The threshold energy (Eth) was determined by employing the relevant relationship, E_{th} = ħcvth [3]. The lattice energy, known as U_L , can be formulated as follows[72]

$$U_L = 3.108 (MV_m^2) \times 10^{-5} \quad (3.50)$$

3.3 SCANNING ELECTRON MICROSCOPE

SEM can generate high-resolution images of a sample surface. SEM images have a high depth of field due to the manner they are made, giving them a characteristic three-dimensional appearance that is beneficial for understanding the surface structure of a material. Large depth of field and a wide variety of magnifications are characteristics of the most popular imaging mode for specimens in the SEM. When inner shell electrons are ejected from the sample by the primary beam, distinctive x-rays are generated, which can be used to detect the elemental makeup of the sample. The sample's backscattered electrons can be utilized independently to create images or in conjunction with the distinct x-rays to reveal atomic number contrast clues regarding the sample's elemental composition.



Fig. 3.4: Scanning Electron Microscope at Nuclear Science and Engineering Department, MIST, Dhaka.

Scanning electron microscope (SEM) micrographs of the different compositions employed in the current study. We have used Imagej software to investigate grain size by analyzing surface morphology of the ceramics.

3.4 OPTICAL PROPERTY MEASUREMENT

UV-visible spectrophotometer (Perkin Elmer, USA, Lambda 365) used to record UV-visible absorbance spectra between (200-1100) nm. Band gap energy can be determined from the Tauc's equation, $(\alpha h\nu)^n = A(h\nu - Eg)$ and absorption coefficient relation $\alpha = 2.303 (A/t)$, where, t stands for sample thickness and A for sample absorbance, where α denotes absorption coefficient, depending on the type of electronic transition that caused the absorption, n= 1/2, 3/2, 2 or 3 are possible, and A is a constant [73]. UV-visible spectroscopy refers to the study of photons in the UV-visible spectrum. It uses both visible light and light with near-ultraviolet and near-infrared wavelengths. Molecules undergo electronic changes in this part of the electromagnetic spectrum.

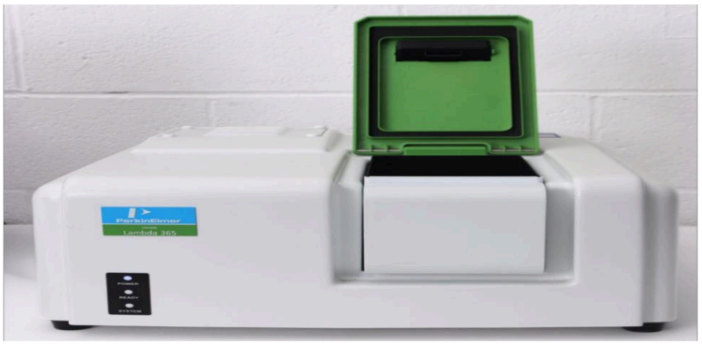


Fig. 3.5 UV-vis Spectrometer Lambda 365, Postgraduate lab, Physics, CUET.

The primary functions of spectrophotometers (UV-Vis) are the measurement of transmission, absorption and reflectance that occur in both the liquids and transparent or opaque solids. The refractive index n(ω) and extinction coefficient (k) for prepared materials, can be determined over the wavelength range of 250–800 nm by means of the Kramers–Kronig method, $N'(\omega) = n(\omega) + ik(\omega)$.[74]

3.5 MAGNETIC PROPERTY ANALYSIS

Physical Property Measurement System (PPMS) (DynaCool, USA, Quantum Design) used to take magnetic measurement of the temperature-dependent magnetization under 3T external magnetic field. The LAS expression can be represented as

$$M = M_s\{1 - \frac{8K_1^2}{105M_S^2H^2}\} \quad (3.51)$$

The M-H fitted curve produces the values of K_1 and M_S, and equation

$$K_1 = \frac{M_S H_c}{0.96} \quad (3.52)$$

which has allowed for the calculation of K1. The total magnetization of A site and B site can be determined from the equation ($M_s = M_B - M_A$) and the experimental magnetic moment can be obtained from the following expression

which has allowed for the calculation of K_1. The total magnetization of A site and B site can be determined from the equation ($M_S = M_B - M_A$) and the experimental magnetic moment can be obtained from the following expression

$$n_{exp}(\mu_B) = \frac{M \times M_S}{5585} \quad (3.53)$$



Fig. 3.6 : Physical Property Measurement System(Atomic energy commission, Dhaka).

The canting angle effect with Saturation magnetization can be found from the canting effect which related the relation $M_S = M_B\cos\gamma - M_A$ [1, 5, 14]. The magnetocaloric effect derived [61, 66] using Maxwell's thermodynamic relation

$$\nabla S_m = \int \frac{dM}{dT} dH \quad (3.54)$$

The magnetic properties of materials as a function of temperature and field are to be continuously recorded by the PPMS.

This type of magnetometer moves the sample up and down in an area bordered by several pickup coils. Thus, the magnetic sample behaves as a time-varying magnetic flux that varies within a certain fixed area. According to Maxwell's law, an electric field follows a time-varying magnetic flux to cause a voltage to be induced in pickup coils. A control unit system processes this alternating voltage signal to improve the signal-to-noise ratio. Measurement of the sample's magnetization is the outcome.

3.6 IMPEDANCE ANALYZER

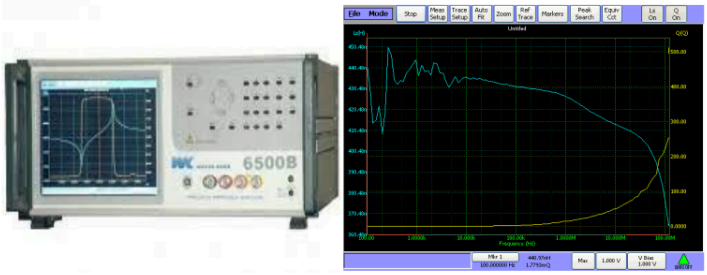


Fig. 3.7 Impedance Analyzer Wayne Kerr 6500B, Postgraduate lab, Physics, CUET.

The Wayne Kerr Technologies 6500B precision impedance analyzer, known for its reliability, is housed in the physics department of Chittagong University of Engineering and Technology in Chattogram. This device is particularly well-suited for measuring and analyzing the electrical properties of diverse electronic devices. Furthermore, the 6500B impedance analyzer (illustrated in Fig. 3.6) is an essential tool for the advancement of circuit designs and for the exploration and development of materials, encompassing both electrical and non-electronic types.

3.6.1 COMPLEX INITIAL PERMEABILITY MEASUREMENT

The frequency range of 20Hz–120MHz of a Wayne Kerr impedance analyzer (model no. 6500B) and the complex initial permeability ($\mu^* = \mu_i' + \mu_i''$) have been determined. The following relations were used to compute the real portion (μ_i') as well as the imaginary (μ_i'') portions of the complex initial permeability:

$$\mu_i' = \frac{L_s}{L_0} \quad (3.55)$$

$$\mu_i'' = \mu_i' \tan\delta \quad (3.56)$$

where Ls stands for the self-inductance of the sample core,

$$L_0 = \mu_0 \frac{N^2 r}{2\pi} \ln\left(\frac{R_2}{R_1}\right) \quad (3.57)$$

Here, N stands for the turns number of the coil, r stands for thickness, and R_2 and R_1 stand for the outer and inner radius of the toroid shape sample [23, 75].

3.6.2 DIELECTRIC MEASUREMENT

The following relation has been used to compute the dielectric constant with real ε′ as well as imaginary (ε") portion and the dielectric loss tanδ such as

$$\varepsilon^* = \varepsilon' - j\varepsilon'' \quad (3.58)$$

$$\varepsilon' = \frac{Cd}{\varepsilon_0 A} \quad (3.59)$$

$$\varepsilon'' = \varepsilon'(\tan\delta) \quad (3.60)$$

where ε′ denotes for energy consumption and ε″ denotes for energy dissipation. Where Cp is the pellet capacitance in farad, d is the pellet thickness in meter and tanδ =(1/2πfε′ε0ρ). A represents the flat surface cross-sectional area of the pellet, ε0 is the permittivity constant of free space [76] .

3.6.3 ELECTRIC MODULUS ANALYSIS

Electric dynamics process in the materials can be explained by the spectroscopy of the electric modulus (M* = M′+jM″), which is separated into two components as follows: M' stands for real and M"imaginary of complex electric modulus. The following relationships between electric modulus and the dielectric constant for the real as well as imaginary portion of electric modulus such as

$$M' = \frac{\varepsilon'^2}{\varepsilon'^2 + \varepsilon''^2} = \omega C_0 X \quad (3.61)$$

$$M'' = \frac{\varepsilon''^2}{\varepsilon'^2+\varepsilon''^2} = \omega C_0 R \quad (3.62)$$

C_0 defines geometrical capacitance equals to ε0A /t , where ε_0 = 8.854 10-14 F/Cm is the free space permittivity [64-65].

3.6.4 IMPEDANCE ANALYSIS

The effective resistance Z of dielectric materials can be calculated using the subsequent formula when they are exposed to an external alternating electric field, Z = R +jX, where resistance and reactance denoted by R and X respectively. The complex impedance is created by the combination of resistance and its corresponding reactance.

The resistance and reactance part of impedance can be calculated using the following formula R = Z′ = Rs and X = Z″ = 1/ωCp , where f is the frequency of the applied electric field [64-65].

3.6. 5 AC CONDUCTIVITY ANALYSIS

The correlation between ac conductivity and frequency is given by the expression $\sigma_{tot} = \sigma_0(T) + \sigma(\omega,T)$. Here, the initial term $\sigma_0(T)$ refers to band conduction, which represents the dc conductivity, and it is not influenced by frequency.

The first term is primarily important at low frequencies and high temperature, while the second term is chiefly significant at low temperatures and high frequencies.

Dense ceramic sample's ac electrical conductivity can be determined $\sigma_{ac} = \varepsilon' \varepsilon_0 2\pi f \tan\delta$, here ω = 2πf denotes angular frequency [1]. The AC conductivity of the sample can be fitted to Jonscher's power law, which is presented as follows, $\sigma_{ac} = \sigma_{dc}(T) + A\omega^n$. The value of the frequency exponent 'n' varies from 0 to 1. The significance of 'n' reveals important details about the interaction of charge carriers with their environment. For values of n less than 1, the main mechanism of conduction primarily involves interfacial charge transfer; on the other hand, for values of n greater than 1, other charge transfer processes may contribute to an increase in conductivity. This deviation from the n values illustrates a phenomenon influenced by various factors, including the material's microstructure, temperature, and composition.

.

CHAPTER 4

RESULTS AND DISCUSSION

4 GENERAL

This section reveals the outcomes of the research and discusses their potential implications. The interpretations of the experimental results, comprising X-ray diffraction (XRD), Rietveld refinement, magnetization, dielectric studies, modulus studies, and dynamic conductivity, are aligned with the objectives set forth in the study. Every section is thoroughly examined and appropriately referenced in academic literature.

4.1 XRD ANALYSIS

4.1.1 STRUCTURAL PROPERTIES

XRD data is used to examine the structural characteristics of Ni-Cd-Al bulk ferrites specimen to obtain the XRD pattern at room temperature for each composition in the 2θ range from 20° to 70° with scanning step 0.01. Identified diffraction planes are (220), (311), (222), (400), (422), (511), (440) and corresponding 2θ angle as 30.28˚, 35.65˚, 37.30˚, 43.35˚, 53.82˚, 57.35˚ and 62.97˚ respectively [2, 4, 77]. There are no extra peaks and the peaks are complying with the cubic spinel structure shown in Fig. 4.1. Single-phase spinel structure formed successfully. Table 1 revealed theoretical, Rietveld refinement method and experimental values of the lattice constant and volume as well as other structural factors of Ni-Cd-Al bulk compound [2, 76]. The Scherrer's formula used to estimate [78] the crystallite size of which found from (36-43) nm with a high intense peak corresponding to the (311) plane recorded in Table 1.

dislocation(δ), lattice strain (ε_{LS}), micro strain (ε_{rms}) and stacking faults (SF) are calculated and mentioned in Table 4.1 [2]. The density ρ_X and ρ_B with apparent porosity for various compositions shown in Table 4.1. Fe^{3+} (0.064 nm) has a greater ionic radius than Al^{3+}(0.054 nm). The density of substance affects its structural qualities. The porosity has shown decreased in this situation by substituting Al^{3+} for Fe^{3+}. The surface area, the hoping lengths and the ionic radii of the tetrahedral and octahedral sites determined for A-A sites, B-B sites, and A-B sites, octahedral edges of the shared and unshared (d_{BE}) and (d_{BEU}) as well as the tetrahedral edge (d_{AE}) which shown in Table 4. 2 [63]. As the Al content in the composition increases, the height of the peaks broadens, which implies a smaller crystallite size. Therefore, Al is an essential element for achieving reduced crystallite sizes and for enhancing the properties of the crystalline structure.

The identified sharp peaks correspond to the reference value and affirm the structure of spinel formation across all samples, suggesting a consistent crystalline homogeneous structure.

Table 4.1: Structural parameters lattice spacing(nm), lattice constant(A°), volume(nm^3), dislocation (lines/m^2), lattice strain, micro strain, stacking faults, RMS strain, density (kg/m^3), surface area (m^2/kg) and porosity, P (%) of $Ni_{0.65}Cd_{0.35}Fe_{2-x}Al_xO_4$ bulk ferrites.

Al Content	d (nm)	a_{th} (A°)	a_{exp} (A°)	V (A°)	δ $\times 10^{14}$	ε_{Ls} $\times 10^{-3}$	ε_{rms} $\times 10^{-4}$	SF	ρ_{th} $\times 10^{3}$	ρ_{exp} $\times 10^{3}$	P
0.00	0.25157	8.344	8.345	580.92	6.92	2.95	3.43	0.446	5.77	5.22	9.80
0.015	0.25170	8.350	8.348	582.18	6.57	2.92	3.37	0.452	5.75	5.27	9.44
0.030	0.25157	8.349	8.345	581.97	6.57	2.88	3.27	0.446	5.75	5.32	8.51
0.045	0.25150	8.347	8.345	581.55	7.30	3.09	3.78	0.446	5.75	5.33	9.58
0.060	0.25218	8.365	8.362	585.32	7.71	3.13	3.84	0.447	5.70	5.35	8.83

Table 4.2 : Structural parameters ionic radii(nm), bond length (nm), hopping length (nm), tetrahedral edge, dAE(nm), octahedral shared edge, dBE(nm) and octahedral unshared edge, dBEU (nm) of $Ni_{0.65}Cd_{0.35}Fe_{2-x}Al_xO_4$ bulk ferrite.

Al content	r_A	r_B	A- O	B-O	L_{A-A}	L_{B-B}	d_{BE}	d_{BEU}	d_{AE}
0.00	0.05	0.1	0.18	0.21	0.362	0.295	0.2950	0.2950	0.181
0.015	0.05	0.1	0.18	0.21	0.362	0.295	0.2952	0.2952	0.181
0.030	0.05	0.1	0.18	0.21	0.362	0.295	0.2951	0.2951	0.181
0.045	0.05	0.1	0.18	0.21	0.361	0.295	0.2951	0.2951	0.181
0.060	0.05	0.1	0.18	0.21	0.362	0.295	0.2957	0.2957	0.181

4.1.2 RIETVELD REFINEMENT

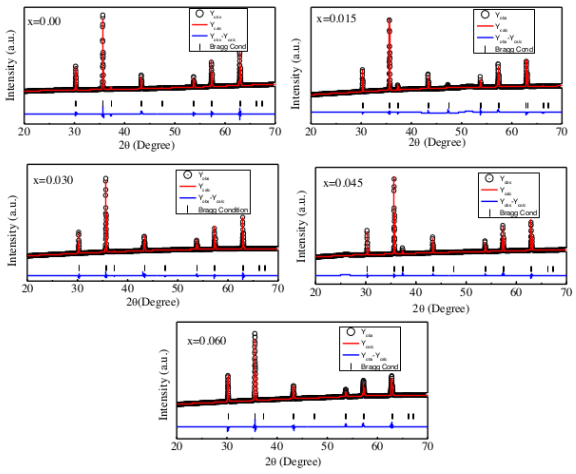


Fig. 4.1 Rietveld refinement of XRD data of $Ni_{0.65}Cd_{0.35}Fe_{2-x}Al_xO_4$ bulk ferrite.

The XRD data is traveled under the road of Rietveld refinement methods. The refined fitting patterns as well as original data shown in Fig.4. 2 where the experimental data represented by black hollow circle, the refined data are represented by solid red lines, the difference between the two data shown by blue curves, and the Bragg is shown by black bars. A good $\chi 2$ result obtained by repeating the refinement process several times. $\chi 2$ value is regarded as having a good fitting range of 1 to 3 [78].

Table 4.3: Fitting parameters for $Ni_{0.65}Cd_{0.35}Fe_{2-x}Al_xO_4$ structural analysis through Rietveld refinement.

Al content	R_p	R_{wp}	R_{exp}	R factors		$\chi 2$	Bragg contribution	DW-Stat
0.00	29.9	14.1	10.35	0.414	0.983	1.86	9.19	0.3053
0.015	48.1	15.1	9.12	0.667	1.11	2.75	13.08	0.1254
0.030	34.1	13.4	8.62	0.485	1.03	2.40	14.07	0.1982
0.045	49.1	14.6	9.08	0.651	1.10	2.60	15.21	0.1072
0.060	40.0	15.70	9.87	0.563	1.12	2.57	6.196	0.1068

Bulk composition of Ni-Cd-Al bulk ferrites for which $\chi 2$ values found within this range and good fitting.

Optimum data formed from structural study of cubic FCC phase of every compound observed. The symmetry corresponds to the space group Fd3m. R_{wp}, R_{exp} and $\chi 2$ along with other structural parameters provided in Table 4.3 [69]. The profile elements Rp are significant, as shown in Table 4.3. The Bragg contribution, often known as the global user goodness of fit value, used to substantiate that the goodness of fit $\chi 2$ values is lower and that the process of best fitting is satisfied. It is thought to be a suitable fitting parameter if the Bragg contribution is more than 10. Table 4. 3 presented that less than 2 result for domain wall-state.

4.1.3 CRYSTALLITE SIZE AND STRAIN

Fig.4.2 has been depicted about the modified Scherrer's formula used to estimate the size of which found from (36-43) nm with a high intense peak corresponding to the (311) plane recorded in Table 4. It is possible to draw a straight line with an intercept equal to ln (kλ/D) by plotting between lnβ and ln(1/cosθ) from modified Scherrer approach which was given crystallite size [79].

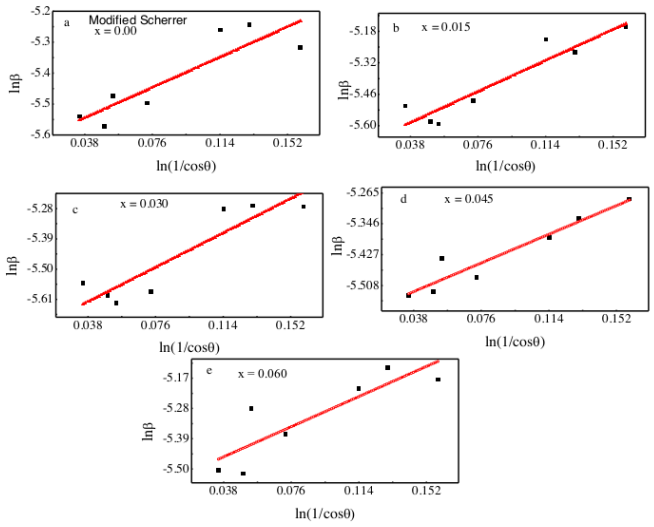


Fig. 4.2 (a-e) Crystallite size determination of $Ni_{0.65}Cd_{0.35}Fe_{2-x}Al_xO_4$ by modified Scherrer's approach.

Fig.4.3 was illustrated about the Williamson-Hall (W-H) formula used to measure the size of bulk ceramics of NCA which found from (46-60) nm shown in Table 4. When compared to the Scherrer approach, the Williamson-Hall analysis is a more straightforward integral breadth method that fluctuates with tanθ rather than following 1/cosθ dependency. The uniform deformation model asserted that strain is equal in all crystallographic orientations. The term (4sinθ) has used to plot the term ($\beta_{hkl}\cos\theta$) [80].

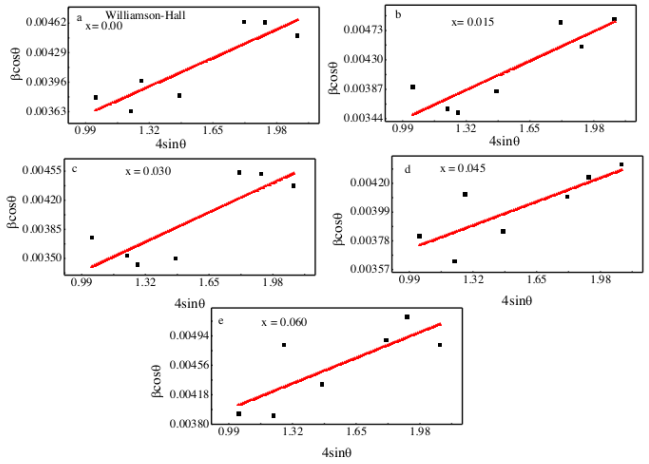


Fig.4.3 (a-e) Crystallite size determination of $Ni_{0.65}Cd_{0.35}Fe_{2-x}Al_xO_4$ bulk by Williamson-Hall Method.

The strain and crystallite size were determined by the fitted line's slope and vertical axes Y-intercept, respectively in Fig.4 [9, 79-80]. The W-H analysis shown in Table 4. 4. Fig.4.4 has demonstrated about the Size Strain Method (SSM) used to measure the crystallite size of NCA found from (38-44) nm.

The term $(d_{hkl}\beta_{hkl}\cos\theta)^2$ has plotted against the $(d_{hkl}^2\beta_{hkl}\cos\theta))$. Crystallite sizes have derived from the slope of the linearly fitted data from size strain method shown in Table 4.4.The Scherrer equation only takes into consideration significant peaks, whereas both the W-H approach [79] and the SSM plot, which also take into account the strain rectification component, result in further reductions in crystallite size.

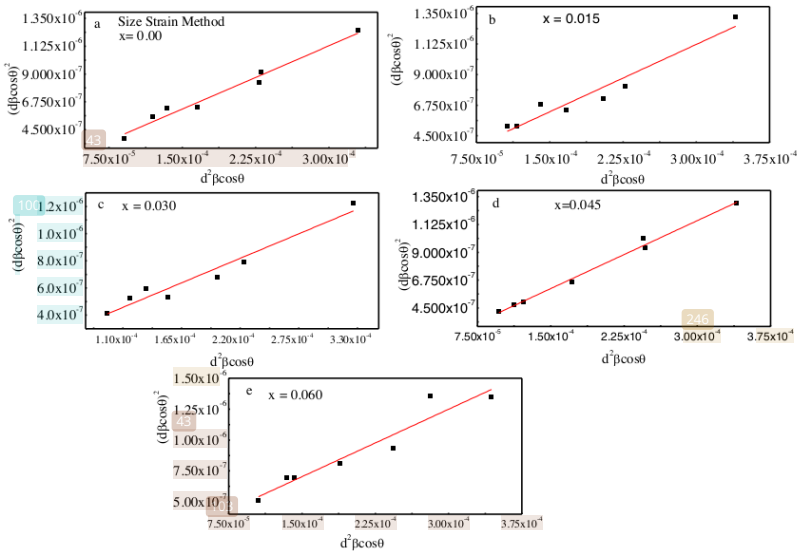


Fig.4.4 (a-e) Crystallite size determination of $Ni_{0.65}Cd_{0.35}Fe_{2-x}Al_xO_4$ bulk by Size Strain Method.

Table 4.4: Crystallite size "D" and Strain using the Scherrer's formula, Williamson-Hall plot and Size-Strain Plot.

Al content	The Scherrer's formula		Modified Scherrer		Williamson-Hall method		Size-strain plot	
	D(nm)	ε ×10⁻³	D(nm)	ε	D(nm)	ε ×10⁻³	D(nm)	ε ×10⁻³
0.00	38	2.95	39	2.58	46	0.70	40	1.07
0.015	39	2.92	39	2.58	64	1.29	44	1.31
0.030	39	2.88	43	3.62	60	1.07	42	0.97
0.045	37	3.09	37	1.98	43	0.52	38	0.58
0.060	36	3.13	36	2.88	46	1.00	38	1.59

4.1.4 CATION DISTRIBUTION AND CRYSTAL SHAPE FORMATION

According to the final results of the distribution of cation determine from XRD and Rietveld refinement, the Al^{3+} that replaced for the Fe^{3+} predominantly both occupy the B site. These findings concur with the results reported in Table 4.5. To balance the relative occupancy offered by the space group, some of the Fe^{3+} move from the B site to the A site at the same [80]. In spinel ferrites, Cd is known to have a high affinity for the A sites. Ni-Cd ferrite form by combining Ni^{2+} and Cd^{2+}. Fe^{3+}/Cd^{2+} complexes are found [81] in A sites, while Fe^{3+}/Ni^{2+} complexes are found in B sites. Fig.4.5 displayed the crystal structure with cationic position from output refinement process typical x = 0.00, 0.030 in which the Ni atom is depicted as blue, the Cd atom as green, and the Al atom as black, the Fe atom as pink, and the O_2 atom as red. All structures spinel cubic phase represents the bond between the atoms.

Table 4.5: A sites and B sites cation distribution of $Ni_{0.65}Cd_{0.35}Fe_{2-x}Al_xO_4$ bulk ferrite.

Al content (x)	A site	B site
0.00	$Ni_{0.20}Cd_{0.35}Fe_{0.78}$	$Ni_{0.45}Fe_{1.22}$
0.015	$Ni_{0.16}Cd_{0.35}Al_{0.002}Fe_{0.735}$	$Ni_{0.49}Al_{0.013}Fe_{1.25}$
0.030	$Ni_{0.18}Cd_{0.35}Al_{0.05}Fe_{0.75}$	$Ni_{0.47}Al_{0.025}Fe_{1.175}$
0.045	$Ni_{0.19}Cd_{0.35}Al_{0.010}Fe_{0.70}$	$Ni_{0.46}Al_{0.035}Fe_{1.255}$
0.060	$Ni_{0.20}Cd_{0.35}Al_{0.015}Fe_{0.70}$	$Ni_{0.45}Al_{0.045}Fe_{1.25}$

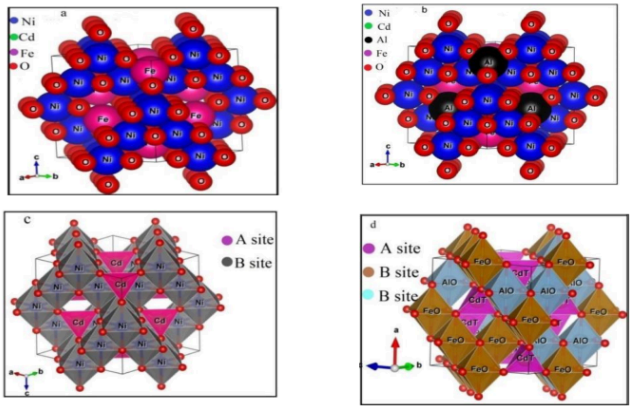


Fig. 4.5 Crystal shape (a-b) as space filling and (c-d) as polyhedral.

Fig. 4.5 is displayed the crystal structure with cationic position from output of Rietveld refinement process of x = 0.00, 0.030 in which the Ni atom is depicted as blue, the Cd atom as green, and the Al atom as black, the Fe atom as pink, and the O atom as red. All structures spinel cubic phase represents the bond between the atoms. Fig. 4.5 (a) is depicted the crystal structure as space filling of the main compound in without Al ions substitution. Fig. 4.5(b) is illustrated the structure of crystal as space filling with Al atoms. Al with step x = 0.015 has been substituted up to x = 0.060 in mother compound. Fig. 6 (c-d) is depicted basic crystal structure with atoms and bonds in the form of polyhedral, respectively. The occupied A and B sites of interacting atoms is displayed in Fig. . Ni atom is occupied by B sites which are dark grey and Cd is occupied by A site which represents pink color in Fig.4.5 (c). Fig.4.5 (d) is expressed that Cd strongly preferred by A site (tetrahedral). Fe and Al atom strongly preferred by B site which is brown color and Aqua color. Earlier study is explained and demonstrated comparable structure [82]. The substituting of Al in the Fe site has a significant influence on the structure of crystal, as is displayed by the analysis of these structures.

4.1.5 ELECTRON DENSITY METHOD

Fig.4.6 (a-e) are illustrated the electron density of the plane (311) with the highest intensity [80]. To investigate density by EDM mapping and comprehend EDM density distribution within the unit cell, the GFourier software from the FullProf package employed. The positions of the atoms that make up the constituent parts of the molecule contained within the unit cell could be found out by analyzing of the density. Electron density is the geometric structural factor's Fourier transform applied to the entire unit cell. The Fourier map of the electron scattering density might be two-dimensional (2D) or three-dimensional (3D). The electron density is described as a position-dependent periodic function, peaking at an atom's position and decreasing to a minimum value between the atoms. Here, red denotes a location with a high density of electron whereas blue denotes a region with a low density of electron. The typical 2D Fourier distribution of the density of electron of Fe^{3+}/Fe^{2+} and O atoms on the yz plane in the unit cell is shown in Figure 4(a-e). The electron distribution in valence d orbitals principally responsible for the thick and dense circular form of the contours encircling Fe^{3+}/Fe^{2+} [78] . The valence distribution orbital 2s and 2p electrons responsible for the outlines surrounding the Oxygen. Positive and some negative values also detected. These represented different forms of bonds between them. It emphasized that positive values are linked to covalent bonds, which bind two atoms together.

However, an ionic bond more precisely, a metallic ionic bond, which shown negative value when two atoms are joined by an exchange of charges.

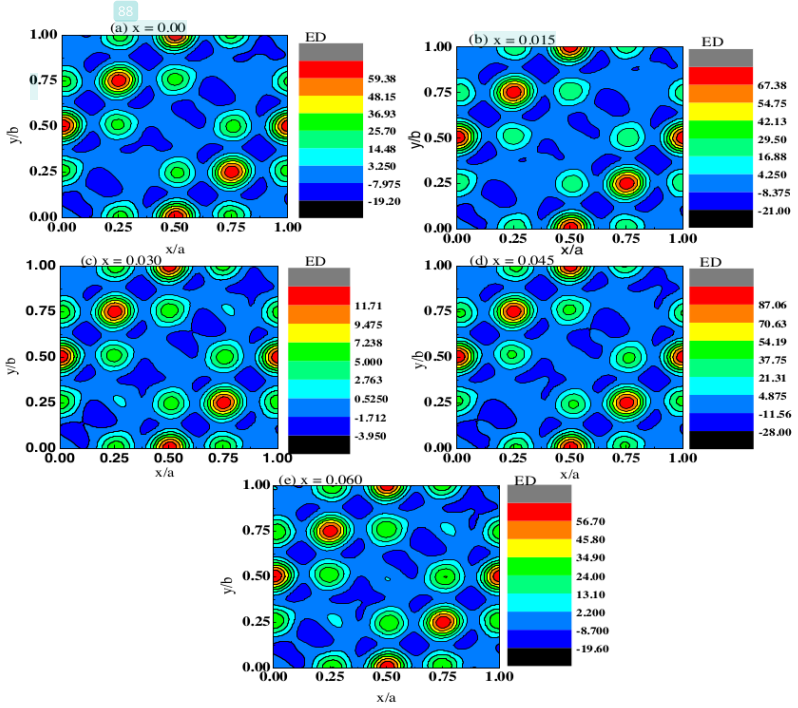


Fig. 4.6 Fill contour 2D representation of $Ni_{0.65}Cd_{0.35}Fe_{2-x}Al_xO_4$ bulk ferrite.

Strong covalent bonds observed in the atoms of various combinations in this investigation. For instance, the covalent link between Fe^{3+} and O^{2-} denoted by yellow and brown circles. The maps of remaining compounds displayed such trends as well. The density of electrons changes as shown due to the exchange of electrons. 3D representations of EDM examined in Fig. 4.7(a-e). The values of the three related axes are x/a, y/b, and z/c in three-dimensional represented. The combinations of these values allowed us to observe the overall densities of the compound. The matching values for each of the map's colors shown in the colored pattern legend to the right.

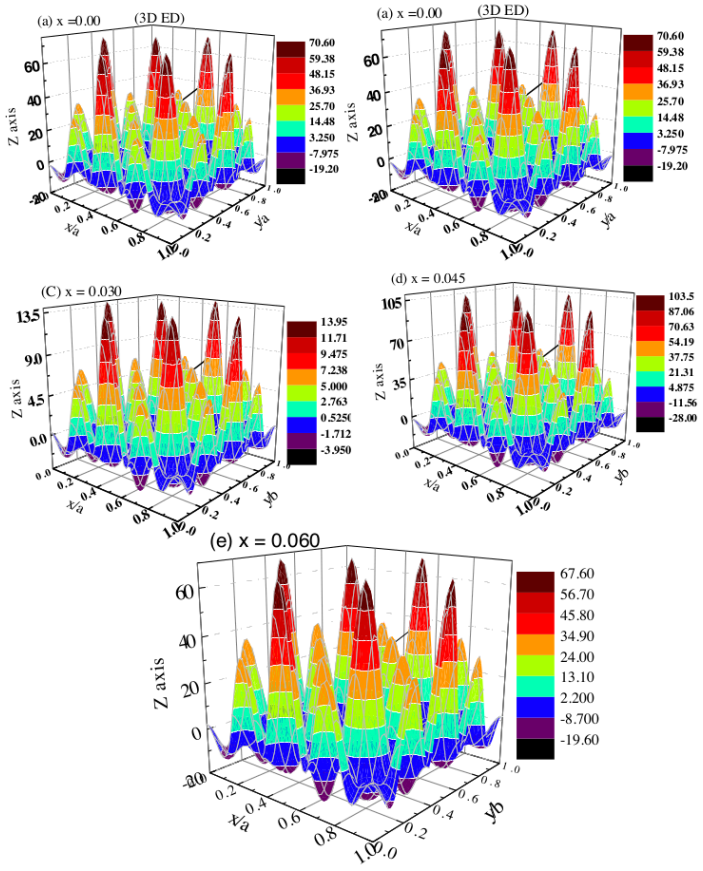


Fig. 4.7 3D representation of $Ni_{0.65}Cd_{0.35}Fe_{2-x}Al_xO_4$ bulk ferrite.

The blue line represented the lowest density numbers, while the red line the greatest values of density. Several negative values from found to represent the ionic forms that were previously mentioned [83]. The most intriguing result of this analysis is the lowering of ionic forms in dense ferrite ceramics caused by the emergence of Al^{3+} substituting on the Fe^{3+} sites.

As more Al is added, the covalent bonds grown stronger as a result. Aluminum tends to form covalent bonds rather than ions since it is a trivalent transitional substance. These 3D Maps satisfied this behavior. The Sigma density, Maximum density, and Minimum density determined using MEM and are shown in Table 4.6.

The most intriguing result of this analysis is the lowering of ionic forms in dense ferrite ceramics caused by the emergence of Al^{3+} substituting on the Fe^{3+} sites. As more Al is added, the covalent bonds grown stronger as a result. Aluminum tends to form covalent bonds rather than ions since it is a trivalent transitional substance. These 3D Maps satisfied this behavior. The Sigma density, Maximum density, and Minimum density determined using MEM and are shown in Table 4.6.

Table 4.6: Electron distribution densities of $Ni_{0.65}Cd_{0.35}Fe_{2-x}Al_xO_4$ bulk ferrite.

Al Contents x	Density max	Density min	Sigma density
0.00	75.11	-19.85	6.24
0.015	79.52	-22.23	6.20
0.030	15.95	-4.15	6.42
0.045	95.39	-24.75	6.53
0.060	79.45	-20.02	6.55

All maximum densities displayed as positive figures. Therefore, in these cases, covalent bonds take precedence, which supported the bulk ceramic ferrite structures depicted in Fig.4.6 and Fig.4.7. The fact that the lowest densities are all negative, however, shows that ions formed between the atoms. Finally, the density rate in this field revealed by the sigma density. It found the covalent bonding nature and strength of bonding from the electron density maps study. Bond strength are correlated with magnetization as well as with the mechanical stability and potential durability of the materials [84].

4.2 SURFACE MORPHOLOGY

Fig. 4.8 is demonstrated the SEM images carried out to observe the surface morphology, grain size, and shape of the bulk of Ni-Cd-Al bulk compound. It illustrated that the amount of Al substitution causes the grain size reduction. The grain size ranges from 4.00 to 1.00 µm found by analyzing Imagej software. As the amount of Al substitution increases, it shown that the grain size reduces, indicating that Al substitution prevents exact crystal formation. This is because that small amount of aluminum oxide Al_2O_3 might be separated at grain boundaries, preventing boundary movement as the second-phase in the final sintering stage [50].

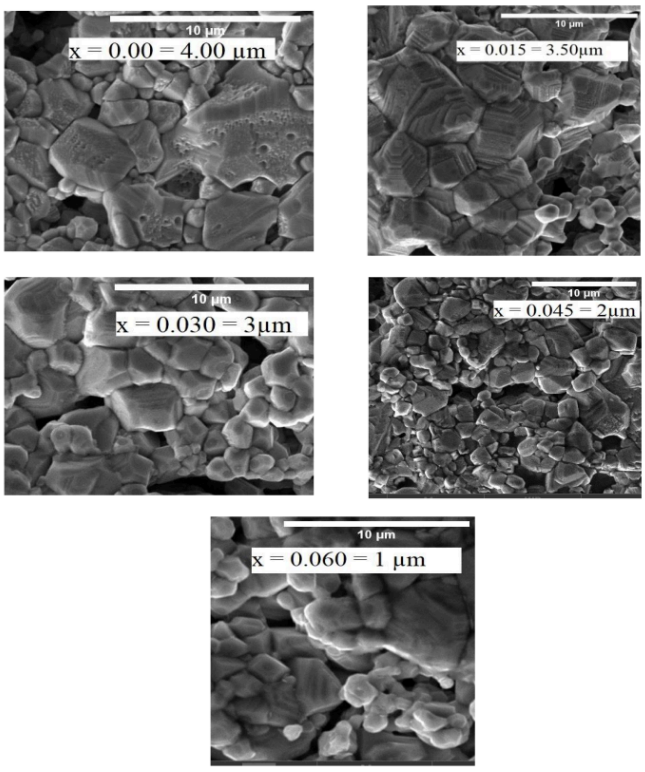


Fig.4.8 SEM images of $Ni_{0.65}Cd_{0.35}Fe_{2-x}Al_xO_4$ bulk ferrite.

Smaller grains aggregated as a result of the aluminum substitution because of the magnetic interactions between the nearby particles.In the molecular structure of the ferrite, the stoichiometric rate of Fe atoms decreases as Al content rise. The stoichiometric rate of aluminum on Fe led to smaller nanoparticles and limited development due to ionic radii and internal stress [85]. Similar variation in grain occurred when the amount of Al substitution increases [5, 17]. The average crystallite size tends to decrease as the Al content increases as confirmed by the XRD pattern.

4.3 OPTICAL PROPERTIES

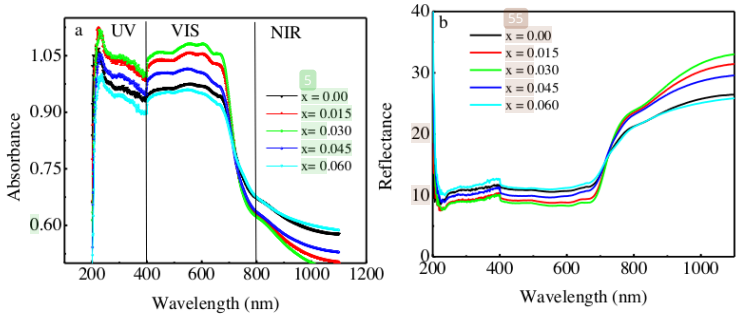


Fig.4.9 Optical Absorbance and Reflectance of $Ni_{0.65}Cd_{0.35}Fe_{2-x}Al_xO_4$ bulk ferrites.

Fig. 4.9 is depicted the optical absorbance and reflectance properties of Ni-Cd-Al bulk ferrite compound. In order to comprehend the optical characteristics of this compound, UV-visible spectrophotometer used. UV-visible absorbance spectra recorded between (200-1100) nm. It is reveal that Ni-Cd-Al bulk spinel ferrite exhibits characteristics UV and visible light absorption. From Fig., it is observed that absorbance increases in the range (300-700) nm up to x = 0.030 beyond that it decreases with Al content. For Fe^{3+} ions, the $3d^5$-$3d^4 4s^1$ transition, or photo-excitation of electrons between the valence and conduction bands occurred inside the investigated mixed ferrites [24]. By applying absorption coefficient relation, $\alpha = 2.303\ (A/t)$, wherever t stands for sample thickness and A for sample absorbance. Fig. was displayed that absorption decreased after 700nm where reflectance start with Al content. The refractive index n(ω) for prepared materials, plotted as a function of λ over the wavelength range of 250–800 nm by means of the Kramers–Kronig method, is shown in Fig.4.10a.

The refractive index (n) varies with λ among the ranges to be 0.30 to 1.05. It is evident that the enhancement of the refractive index in the UV-visible region and then decreases with increasing wavelength, which may be attributed to the normal dispersion law. In Fig. 7, variation among the n values is noted, which may be affected by the permeability characteristics of Ni-Cd-Al bulk or the specific impurities formed due to Al substitution [74].

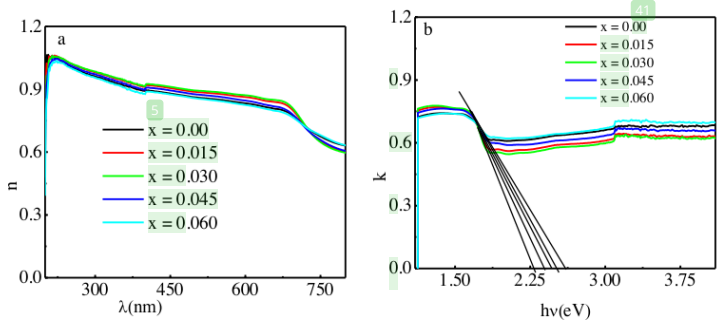


Fig.4.10 Curves of (a) n Vs λ , and (b) k vs. hν for $Ni_{0.65}Cd_{0.35}Fe_{2-x}Al_xO_4$ bulk ferrite using K-K model.

Fig.4.10b illustrates the changes in the extinction coefficient (k) for NCA as determined by the Kramers–Kronig method. It is clear that there exists a predominant broad k value approximately to be at ranges of 2.28 to 2.58 eV and wavelength of 475 to 550 nm within the UV–visible spectrum for NCA spinel ferrite. It is important to highlight that k values rise in two areas, which signifies a significant enhancement in photon absorption within these regions [74, 86].

4.4 FTIR AND ELASTIC PROPERTIES

The analysis is revealed two predominant absorption bands such as ν1, which in the range of (525–578) cm^{-1}, and ν2 situated between (407- 418) cm^{-1}, thus confirming the formation of the structure of the spinel ferrite. Table 4 lists the frequencies connected to the vibrational modes, υ1 and υ2. It is determined that the stretching at the interstitial tetrahedral (A) and octahedral (B) sublattices is responsible for the vibrational mode frequencies [87].

The υ1 peaks are known to be caused by the stretching of tetrahedral metal ions and their corresponds with oxygen, whereas the ν2 peaks are caused by the bending vibrations of cation-oxygen bonds located at the octahedral site [45]

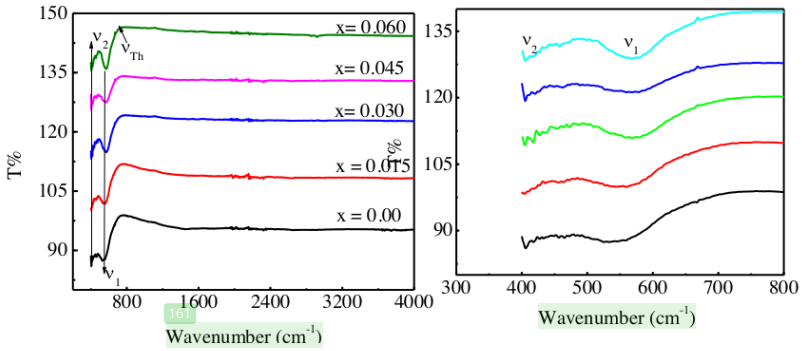


Fig.4.11 FTIR spectra of $Ni_{0.65}Cd_{0.35}Fe_{2-x}Al_xO_4$ bulk ferrite.

The FTIR spectra of the Ni-Cd-Al bulk compound is obtained at room temperature, as illustrated in Fig. 4.8. The data reveals the movement of the ν_1 shift to the higher values with the enhancement of Al substitution. In cubic spinel and spinel-like ferrite, the lengths of the cation–anion (Me–O) and cation–cation (Me–Me) bonds, as well as the associated bond angles, influence the interaction strength of magnetism [66, 88]. All of the computed bond lengths are listed in Table 4.7, and bond angles are included in Table 4.8. The table demonstrates that the average inter-ionic distances tend to decrease with an increase in Al content in the NCA compound. This phenomenon can lead to a decrease in the strength of super-exchange interactions, as a result of wave-function overlap, thereby reducing the Curie point. The reducing trend of Curie point has been published in our previous work [89]. The analysis of bond angles (θ_1, θ_2, θ_3, θ_4, θ_5) in relation to compositions indicates that the interactions of magnetic (A−O−B, A−O−A, B−O−B) exhibit strengthen and weaken between the anions and cations within the sub-lattices. The angles θ_1 and θ_2 signify the A−O−B interactions between the voids, whereas θ_3 and θ_4 denote the bond angles pertaining to the B−O−B exchange interactions. Moreover, θ_5 is related to the A−O−A interactions found within the complexes. The discrepancies in these angles demonstrate that cations are adjusted in relation to the aluminum content, which is affected by varying super-exchange interactions [24]. The calculated bond angles were mentioned in Table 4.8.

which indicates that θ_1, and θ_2 decreasing trend with Al^{3+} content, while bond angles θ_3 , θ_4 and θ_5 increasing trend with Al^{3+} substitution.

Table 4.7: Inter atomic cation-cation bond length Me – Me distances (Å), cation-anion bond length Me – O distances (Å) of Ni-Cd-Al bulk ferrite.

Al content	x	0	0.015	0.030	0.045	0.060
Me - Me distances	b	2.9500	2.9521	2.9518	2.9511	2.9507
(Å)	c	3.4592	3.4617	3.4613	3.4604	3.4600
	d	3.6130	3.6156	3.6152	3.6143	3.6139
	e	5.4195	5.4234	5.4228	5.4215	5.4208
	f	5.1096	5.1133	5.1126	5.1114	5.1108
Me - O distance	p	2.0860	2.0875	2.0875	2.0867	2.0865
(Å)	q	1.8065	1.8078	1.8076	1.8071	1.8069
	r	3.4592	3.4617	3.4613	3.4604	3.4600
	s	3.6130	3.6156	3.6152	3.6143	3.6139

Tabel 4.8: Bond angles of Ni-Cd-Al bulk ferrite.

Al content	θ_1(degree)	θ_2(degree)	θ_3(degree)	θ_4(degree)	θ_5(degree)
0	125.27	154.72	119.99	125.23	79.97
0.015	125.29	154.83	119.98	125.30	79.98
0.030	125.29	154.73	120.00	125.25	79.98
0.045	125.28	154.73	120.04	125.28	79.97
0.060	125.22	154.66	120.00	125.63	80.00

The observed behavior can be linked to the relative weakness of the A–B interactions, in contrast to the enhanced strength of the B–B and A–A exchange interactions [87].

In Fig. 4.11, the variation in (a) the force constants (kT, kO, and Kav) and (b) the stiffness constant in compound are presented as function of Al content. The force constant k (Nm−1), is derived from FTIR absorption spectra by employing standard formulas for the A-sites (kT) and B-sites (kO) cation distribution. Cation distribution was carried out in our previous work [87]. The estimated values pertaining to kT , kO and Kav. are detailed in Table 4.9. Both the force constants of the NCA compound are observed to rise with an

increase with Al content. The average value of Kav. was calculated from KT and KO in Fig. and Table. Fig. 4.12 has illustrated the changes in moduli including Young's (E), bulk (B), and rigidity (G) in relation to the Al content.

Table 4.9: Absorption wave number (ν_1, ν_2), force constant (K), stiffness constant (C_{11}) elastic constant (B, G, E) of $Ni_{0.65}Cd_{0.35}Fe_{2-x}Al_xO_4$.

x	ν_1	ν_2	Force constant (Nm^{-1})			Elastic constant (GPa)			
	(cm^{-1})	(cm^{-1})	K_T	K_O	$K_{av.}$	C_{11}	B	G	E
0	524.00	405.00	210.80	125.92	168.36	201.75	201.75	93.05	140.99
0.015	558.00	404.00	252.81	132.52	192.66	230.79	230.79	115.54	180.53
0.030	566.00	404.00	261.18	133.06	197.12	236.22	236.22	118.25	184.77
0.045	577.00	406.00	270.01	133.68	201.85	241.88	241.88	121.09	189.22
0.060	580.00	404.00	270.70	133.33	201.01	240.38	240.38	120.34	188.38

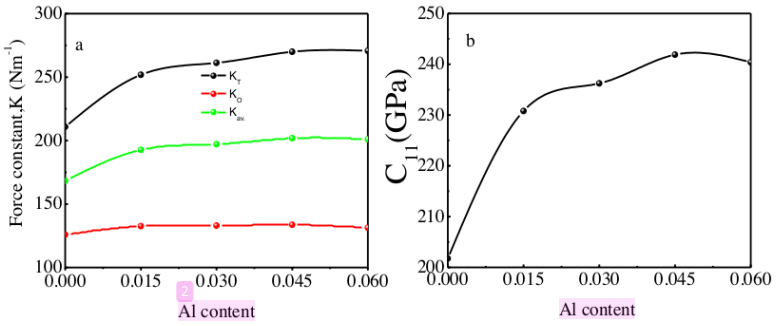


Fig.4.12 : Variation of (a) force constant(k_T , k_O and $K_{av.}$) and (b) stiffness constant of $Ni_{0.65}Cd_{0.35}Fe_{2-x}Al_xO_4$ bulk ferrite.

The calculated values of stiffness constant (C_{11}) is mentioned in Table 4.9. The elastic moduli associated with cubic structures, specifically bulk (B), Young's (E), and shear (G) were computed and are recorded in Table 4.9. Compound's elastic moduli and stiffness constant were observed to rise with increasing Al content [45, 87]. The increase in elastic properties with Al content can be attributed to the characteristics of inter-atomic bonding. Increasing of Al content in Ni-Cd-Al bulk ferrite leads to shorter in inter-atomic distances between cations, thus strengthen the bonds between them.

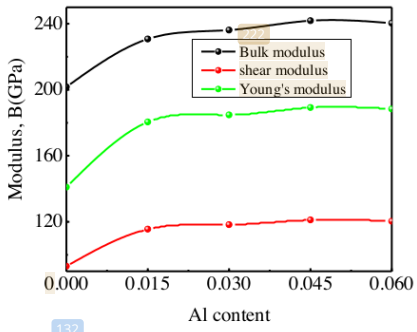


Fig. 4.13 Changes of bulk modulus (B) , modulus of rigidity (G) and Young's modulus (E) with Al content.

Our findings show that, σ varies slightly from the value of 0.28, which falls within the range of -1 to 0.5, suggesting a satisfactory elastic property [87].

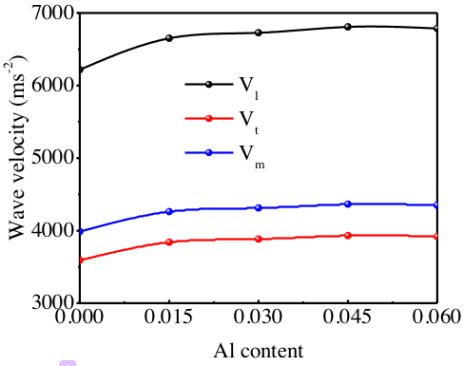


Fig. 4.14 Changes of longitudinal wave velocity (Vl), shearing wave velocity (Vt), and mean wave velocity (Vm) on the Al content in $Ni_{0.65}Cd_{0.35}Fe_{2-x}Al_xO_4$ bulk ferrites.

The variation in wave velocities including V_l, V_t, and Vm is shown in Fig.4.13. The velocities V_l and V_t were calculated using the density of compound and stiffness constant. The values of Vm calculation mainly relies on the parameters V_t and V_l .

The values of V_l, V_t, and V_m were found to increase as result of Al doping with step 0.015 [45,60]. The changes in the Debye temperature (θ_D) with Al content in Ni-Cd-Al bulk ferrites are shown in Fig.4.12. The graph clearly illustrates that an increase in Al corresponds with rise in (θ_D), indicating that lattice vibrations are obstructed as a result of Al substitution [45, 60]. The Debye temperature is a significant factor in the study of lattice vibrations within the field of solid-state physics. It indicates the temperature at which the maximum vibrational activity of the lattice occurs, thus streamlining the integration of thermal capacity. The values of V_l and V_t are used to compute the thermal conductivity of a given material. The Debye temperature, signifying the approximate temperature, where quantum effects become apparent, was calculated through various physical properties, resulting in a range of values [60]

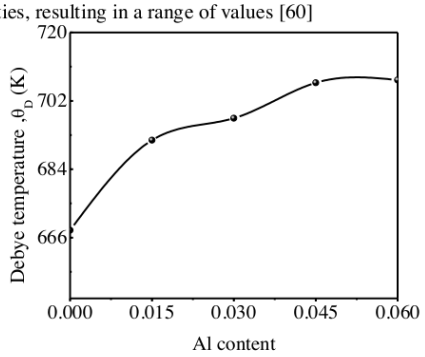


Fig.4.15 Debye temperature (θ_D) variation of $Ni_{0.65}Cd_{0.35}Fe_{2-x}Al_xO_4$ bulk ferrites.

Table 4.10 Longitudinal wave velocity (Vl), transverse (Shear) wave velocity (Vt), mean velocity (Vm) , Poisson ratio(σ), Debye temperature(θ_D) of Ni-Cd-Al bulk ferrites.

x	Wave velocity (ms^{-2})			Poisson ratio	Debye temperature (K)
	V_l	V_t	V_m	σ	θ_D
0	6216.91	3589.34	3984.84	0.30	667.95
0.015	6649.36	3839.01	4262.03	0.28	691.67
0.030	6727.05	3883.86	4311.83	0.28	697.43
0.045	6807.18	3930.12	4363.18	0.28	706.77
0.060	6786.12	3917.97	4349.69	0.28	707.50

4.6 MAGNETIC PROPERTIES

4.6.1 MAGNETIC HYSTERESIS

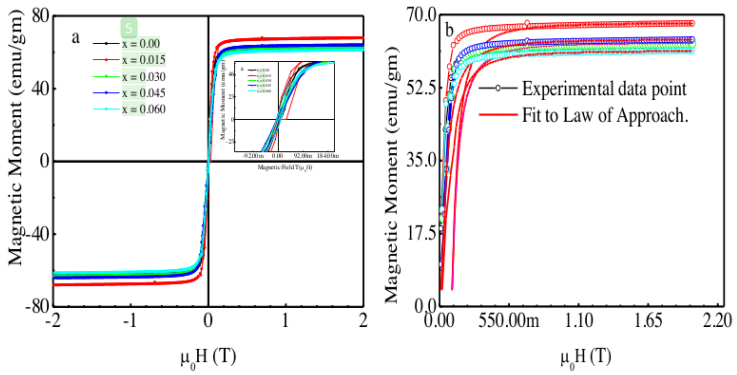


Fig. 4.16 (a) Hysteresis loops and (b) LAS fitted curves of $Ni_{0.65}Cd_{0.35}Fe_{2-x}Al_xO_4$ bulk ferrites.

Fig. 4.16 is presented magnetic hysteresis Fig. (a) and LAS fitting Fig.(b) using PPMS with an applied field of 3T (in μ_0H) at room temperature. The magnetization examined for all the compound and found to rise with magnetic field up to 0. 20 μ_0H (T).

Table 4.11 provided the M_s values for the samples with their theoretical and experimental magnetic moment. It observed that Ms increases up to x = 0.045 beyond that it decreased with the Al content. The hysteresis nature like soft ferrites with Al substitution exhibited the same behavior [1, 5, 13-14].This type of M variation with Al^{3+} content could be explained by the cation distribution with exchange interaction over A- and B-sites, which influences magnetic behavior of the compounds. The distance between the magnetic cations is reduced due to the substitution of a smaller ion Al^{3+}(0.53Å) compared to Fe^{3+}(0.64Å) which increases the A–B exchange interaction [1]. Furthermore, as the non-magnetic Al content rises beyond x = 0.045, decreases the magnetic moment more in the B-site than the enhanced exchange interaction. This results decreased in Ms. Analyzing every compound, from x = 0.00 to x = 0.060, Fig. 4.15(b) displayed the representative curves of M_S fitted to the Law of Approach to Saturation (LAS) to calculate the values of Ms and first anisotropy constant K_1 [Table 4.13]

Table 4.11: Theoretical magnetic moment (nth) and experimental magnetic moment (n_{exp}), saturation magnetization(emu/gm), LAS saturation magnetization(emu/gm), remanent magnetization(emu/gm), coercivity(emu/gm), Curie point (T_c), Curie-Weiss Temperature (Θ_{CW}), anisotropy constant (Jm^{-3}) and overall anisotropy constant (Jm^{-3}) of the $Ni_{0.65}Cd_{0.35}Fe_{2-x}Al_xO_4$ bulk ferrites.

Al content	n_B (th)	n_B (exp)	M_S	$M_{S\,(LAS)}$	M_r	H_C	Tc	Θ_{CW}	$K_1 \times 10^3$	K_{eff} $\times 10^5$
0.00	2.00	1.33	62.78	62.82	4.82	40.19	582.27	787.20	2.62	9.36
0.015	2.53	1.44	67.89	68.05	4.75	37.64	580.08	699.33	2.46	9.40
0.030	2.00	1.34	63.17	63.24	3.32	46.94	579.20	814.66	3.09	9.34
0.045	2.61	1.36	63.96	64.13	2.97	46.31	579.00	800.26	3.08	9.37
0.060	2.55	1.29	61.60	61.41	4.37	46.08	578.76	711.73	2.60	9.34

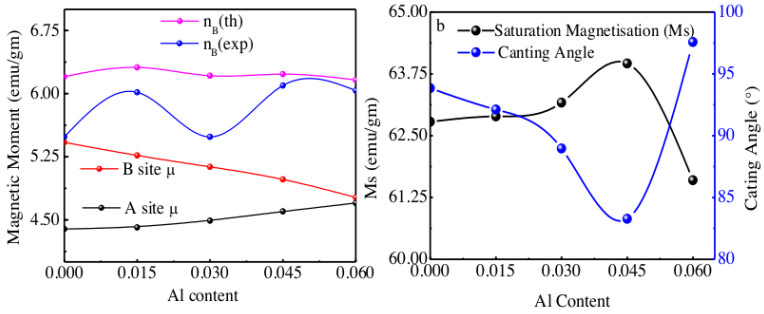


Fig. 4.17 (a) Magnetic moment with Al and (b) Canting angle effect with saturation magnetization.

K_1 has measured from 2.62×10^3 to 3.09×10^3 Jm^{-3} whereas overall anisotropy constant (K) from 9.34×10^5 Jm^{-3} to 9.40×10^5 Jm^{-3}[90]. It was observed that high M_s and low H_c from hysteresis loop indicate soft magnetic materials, which facilitate easy domain wall formation and movement [91]. Analysis of first anisotropy and effective anisotropy depicts the relation between smaller grain size and magnetic performance. M_s is related to anisotropy as per $Ms = 2k/\mu_0 H_C$. The expression K_{eff} represents the particle size-dependent anisotropy , $K_{eff} = K_v + K_s(6/d)$, where K_v and K_s are the material constants, and d represents particle size.

Anisotropy increases with decreasing particle size. The domain-grain size relation is proportionate with ds ∞(grain size)^{m}, when domain size and grain size are compared. The grains might not be completely ordered, yet it is clear that the crystallite regarded as fully ordered [92].

The cations distributed on the A and B sites using Hund's rule with the magnetic moments of Ni^{2+} (2μB), Cd^{2+}(0μB), Al^{3+} (0μB) and Fe^{3+} (5μB). Table 4.5 presented all of the cations in their respective places from the Rietveld analysis. With an increase of Al substitution for Fe^{3+} in the B-site, the total μ_B decreased in the B-site shown Fig.4.16(a). It is observed that Al occupied by the B-site dominantly and A-site very rare. As a result the expected value for the μ_B of Al^{3+} and Fe^{3+} reference value as well as the change in magnetization at the B-site. Thus, the B-A interaction eventually reduces, leading to a drop in the total magnetization ($M_S = M_B - M_A$). Therefore, it found that, with Al substitution, both the total magnetic moment and M_S reduced [14] beyond the value of x = 0.045 shown in Fig.4.17a. and Fig.4.17b. Table 4.11 has presented comparison of the theoretical and experimental values $n_{(th)}$ and $n_{(exp)}$ of the Bohr magnetron μ_B with Al^{3+} substitution.

Due to anti-parallel interaction, theoretical nth (μ_B) calculated using $n_{th}(\mu_B) = (M_B - M_A)\mu_B$ for the magnetic moment and cation distribution as well as using $n_{exp}(\mu_B) = (M \times M_S)/5585$ experimental magnetic moments have trends to increase up to x = 0.045 and then decrease with Al shown in Fig.4.16(a) and Table 4.11. The observed n_{exp} less than n_{th} obtained from Rietveld analysis and cation distribution . The difference between nth and n_{exp} could be explained that n_{exp} measured at room temperature (at 305 K), but nth gives at 0 K. The reason for the linear decrease in Ms is determined from the substitution of the non-magnetic Al^{3+} for the magnetic Fe^{3+} ion at the B-site. Since Al^{3+} is nonmagnetic ion, it does not participate in the exchange interaction with its closest neighbors in the A–B interaction, as a result both the magnetization at the B-site and the net saturation magnetization decrease. The increase of M_S could be interpreted using canting effect which related the relation $M_S = M_B\cos\gamma - M_A$, where M_S initially increases as a result of the canting angle decreasing shown in Fig. 4.16(b) [1,5,13-14]. The magnetization at the saturation point increases up to x = 0.045, when the canting angle γ smaller, i.e., increases cosγ. That is also result of Al^{3+} is smaller size than Fe^{3+} according to XRD study.

4.6.2 TEMPERATURE DEPENDENT MAGNETIZATION AND CURIE POINT

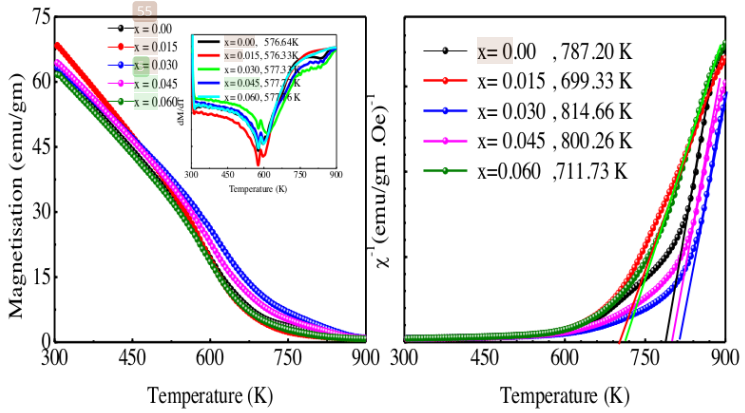


Fig 4.18(a) Temperature dependent Magnetization (M) and(b) The inverse of susceptibility with temperature of $Ni_{0.65}Cd_{0.35}Fe_{2-x}Al_xO_4$ bulk ferrites.

Fig. 4.18 is illustrated the temperature-dependent magnetization measurement under an external magnetic field 3T over a temperature (T) range of (300–900)K. It is observed that M gradually decreased with T. At the Curie point (Tc), all compounds shown ferromagnetic (FM) to paramagnetic (PM) phase transition from M-T curves. TC at which dM vs. dT indicated [24] minimum value. Tc decreased from (582.27 to 578.76)K with Al substitution shown in Table 7 and Fig. 9 [3,24]. TC found to decrease with Al shown in Table 4.11. When Al^{3+} ions are substituted, some ferromagnetic ordering within the system is distorted and decreases active magnetic interaction for each magnetic ion per formula unit, which reduced the Tc. Fundamentally, Neel's two-sublattice ferrimagnetism model predicts that in ferrite spinel, A and B sites interact magnetically in three different ways: A-A, A-B and B-B. The T_c of ferrites is the primary determined from the overall strength of the A-B exchange interaction. The ferromagnetic exchange between Fe^{3+}- O^{2-} - Fe^{3+} is influenced by the electronic configuration 2p6 of the nonmagnetic ion Al^{3+}. As a result, new coupling between Al^{3+} - O^{2-}- Al^{3+} forms without contributing the magnetic interactions. For that reason, the Tc dropped of Ni-Cd-Al bulk ferrites [3,18, 20,90]. Furthermore, because of the shifting valence states, the oxygen deficiency within the spinel has a significant impact on the magnetic structures.

The trend of reducing lattice parameters increasing the A–B exchange interaction. Due to the relatively strong exchange interaction, it constantly takes more energy to disorient the moment that corresponds to higher Tc values of the Ni-Cd-Al bulk ferrites decreases. Consequently, changes Tc signify the formation of new ferrites that have an overall increase in the phase transition temperature [20, 93]. This material is ideal for high-sensitivity magnetic stress sensors due to its strong magnetomechanical effect and high strain sensitivity [93].

Fig. 4.18(b) represented inverse susceptibility (χ^{-1}) with T which indicates transitions from ferromagnetic to paramagnetic. The susceptibility in the paramagnetic region follows the Curie-Weiss expression $\chi^{-1}(T) = (T- \theta_{CW})/C$ in T range, which is significantly above Tc, where θ_{CW} is the Curie–Weiss paramagnetic temperature, C is the Curie constant, and Tc is the Curie temperature. The obtained [24, 90] variation values from 699.33 to 800.26 K of θ_{CW} are higher than T_C, as shown in the Table 4.11. Magnetic inhomogeneity might be the main source of this disparity [3].

4.6.3 MAGNETOCALORIC EFFECT

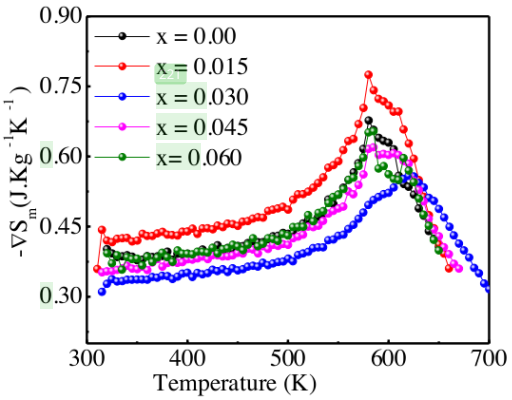


Fig. 4.19 The magnetic entropy changes depending with temperature of under an applied magnetic field of ΔH = 3 T of $Ni_{0.65}Cd_{0.35}Fe_{2-x}Al_xO_4$ bulk ferrites.

Fig. 4.19 is depicted the magnetic entropy changes (ΔSM) with temperature under an applied magnetic field 3T to examine the magnetocaloric effect (MCE) of the Ni-Cd-Al bulk compound.

To assess the MCE of Ni-Cd-Al bulk ferrites, a basic quality element in determining the magnetic refrigeration capacity is the magnetic entropy change. By analyzing the experimental M-T curves, indirect methods for MCE estimate are used to calculate the isothermal change in magnetic entropy (Δ_{SM}) for all compositions during transitions [94]. Isothermal magnetization curves around T_C measured in the magnetic field at 3T. ΔS_M is a fundamental property of magnetic materials used to calculate the MCE parameters. ΔS_M values derived [97] using Maxwell's thermodynamic relation ($\Delta S_M = \int(dM/dH)dH$) and the M-T curve in this investigation. The change of maximum $-\Delta S_M^{max}$ is (0.64, 0.72, 0.54, 0.62, and 0.60) $Jkg^{-1}K^{-1}$ respectively at or near T_C, from Fig. 4.18. Typically, we use the RCP to characterize material from the perspective of its practical applicability in MCE devices, here RCP = (- ΔS_M^{max}) × δT_{FWHM} is a result of the full width at half maximum (δT_{FWHM}) of the (- ΔSM) peak and the maximum values of (- ΔS_M^{max}) [61, 95]. RCP values found from (43.18, 56.12, 52.90, 53.68 and 56.97) Jkg^{-1}. Similar research results found in previous work [94, 96-97]. This characteristic offers on the applicability of the magnetic materials in magnetic refrigerator cooling technology.

4.6.4 COMPLEX INITIAL PERMEABILITY

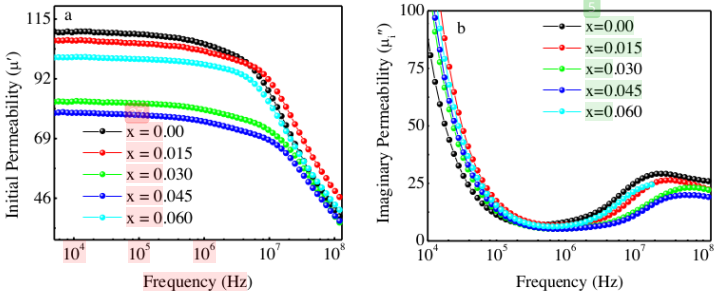


Fig.4.20 Demonstrates (a) the real and (b) imaginary portion of the initial permeability.

Fig. 4.20 a and b are revealed the real (μ_i') and imaginary (μ_i'') permeability of compound with frequency. Up to 8MHz frequency, the μi′ is pretty steady, but beyond that, it grows to a maximum and then quickly decreases with frequency.

The μ_i' parameter used to express the in phase relationship between the magnetic induction component (B) and the alternating magnetic field (H), assesses the capacity of materials to store energy, while the μ_i'' parameter measures the ability of materials to dissipate energy. In contrast, the μi″ rapidly declines at lower frequency sides and has a typical peak at higher frequency sides, where the μi′ begins to decline. It's known as the ferrimagnetic resonance phenomena [98]. The two separate magnetization mechanisms such as domain wall motion and spin rotation are related to the permeability of spinel ferrites . In comparison to spin rotation, domain wall motion contributes more to permeability at lower frequencies. Large grains facilitate domain wall motion, resulting in high permeability. The domain's wall causes the initial permeability to be represented as, $(\mu i')_w = (3\pi M_s^2 D_m)/4\gamma$, $(\mu i')_{spin} = (2\pi M_s^2)/k$, where M_s stands for saturation magnetization, D_m stands for average grain size, K for the magnetocrystalline structure's anisotropy constant and γ for domain wall energy [99]. The particle size, saturation magnetization, and magnetocrystalline anisotropy influence the initial permeability [77]. Variation of initial permeability can be made in a number of ways, including high density structures, saturation magnetisation thin grain boundaries with large grain sizes, and chemical composition optimization [100].

4.6.5 QUALITY FACTOR

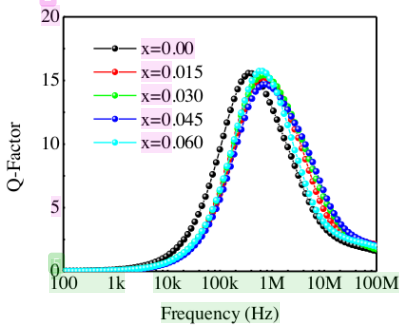


Fig.4.21 Q-factor versus frequency.

Fig. 7 has been shown the quality factor (Q-factor) fluctuations of the compound. The Al substituted compound has been shown wider peak widths than the parent compound.

These wider peak widths offer a broad brand frequency as well as Q-factor value shift towards higher frequency side implies application range suitable for that more accurate method of assessing magnetic characteristics. A favorable peak in the Q-factor for samples containing Al occurs at a frequency of about 1 MHz. Higher Q-factor has observed for x = 0.060 in the middle region of frequency.

4.7 DIELECTRIC PROPERTIES

4.7.1 COMPLEX DIELECTRIC CONSTANT

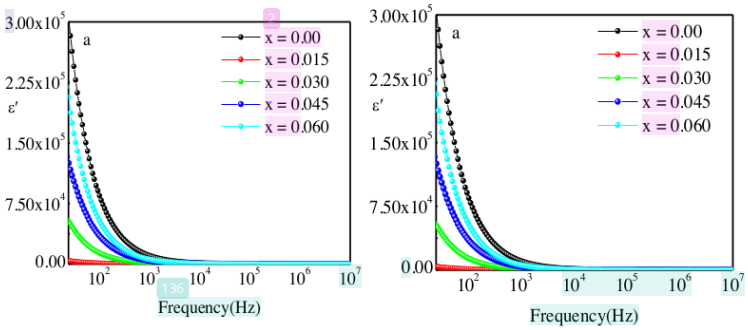


Fig.4.22 Demonstrates (a) the real portion and (b) imaginary portion of the dielectric.

The dielectric properties of Ni-Cd-Al bulk ferrites sintered at 1423K, are shown in both their real and imaginary components in Fig. 4.22a and b. The frequencies are depicted within the range of 20Hz to 10 MHz. As the amount of Al increases, a corresponding decrease in both the real as well as imaginary values ε′ and ε″ of the dielectric constants was noted in the compound. Fig. a shows that the value of ε′ is higher at low frequencies, but lower at higher frequencies. Fig. shows the linear behavior at frequencies above 100 kHz .

The dielectric constant, as observed in Fig. 4.22b, ε″ shows similar decreasing tendency with increasing frequency. After 1 kHz, it also displayed a linear pattern. Comparing ε′ and ε″, in both the cases, substituting Al to Ni-Cd bulk ferrite results in a downward trend of dielectric constant curve [85]. The variation of ε′ and ε″ can be explained by Koop's two-layer model and Maxwell–Wagner polarization theory. The assumption is that electron hopping takes between cations and O^{2-} within framework that enables these interactions. However, when the electrons attempt to pass through the insulating barriers (grain

boundaries), they encounter hindrance and are unable to move from one grain to another. Consequently, the confined electrons accumulate at the grain boundaries, leading to space charge polarization within the ferrites' grains. Furthermore, throughout the sintering process, there exists a chance of forming vacancies for oxygen ions and free charge carriers within the voids. Later, they participate in space charge polarization as well. At low frequencies, the electrons have sufficient time to traverse the grains by following the alternating current field and can engage in space charge polarization. Because of the swift oscillation of the ac field at high frequencies, the electrons attempt to alter their direction too rapidly. Thus, the charge carriers are unable to keep up with the area's path due to a lack of sufficient time. They are unable to gather across the grain boundaries, and space charge polarization vanishes within the grains. Consequently, as frequency rises, the polarization decreases and remains independent in the high-frequency zone [14, 24, 76].

The movement of electron between Fe ions in their Fe^{2+} and Fe^{3+} valence states is caused by the creation of Fe^{2+} ions. The polarization in ferrites is caused by the small-scale shift in charges resulting from the electronic interaction between Fe^{2+} and Fe^{3+} ions, which occur in the with the direction of the applied electric field. The quantity of Fe^{2+}/Fe^{3+} ion pairs located on the B-site determines the magnitude of the exchange. At higher frequencies, conductive grains significantly effect on the material's dielectric constant, whereas the grain boundary has a minimal impact at low frequency [101]. All four types of polarization- electronic, dipolar, ionic, and space charge polarization were detected at lower frequencies. The Maxwell-Wagner Model provides clarity on underlying the concepts of these polarizations. Bulk effect results in electronic polarization, especially at high frequencies. The curve indicates rapid decrease in the dielectric constant with increasing Al concentration [3, 101]. There is a variation in dielectric constants for the x= 0 to x = 0.065 samples within low-frequency range. The interfacial areas of the grain boundaries change because of the variations in grain sizes with Al content. Thus, the buildups of charge carriers at the grain boundaries change depending on compositions x [24]. Consequently, the space charge polarization exhibits minor variations as Al ions doping and dispersion take place for the samples' dielectric constants in the low frequency range [102-105]. The theoretically determined dielectric constant was graphed with frequency and subsequently fitted to the modified Debye equation (MDE) to justify the experimental dielectric properties [106]. The modified Debye relaxation function is a suitable model for describing the dielectric relaxation process, and the dispersion in the dielectric constant can be expressed as, $\varepsilon' = \varepsilon'_{\infty} + (\varepsilon'_0 - \varepsilon'_{\infty})/[1+(\omega\tau)^{2(1-\alpha)}]$.

Where, ε'_{∞} define ε' in the highest frequency ($\omega = 2\pi f_{max}$), ε'_{0} represents ε' in the lowest frequency and the Debye average relaxation time is τ and the spreading factor of the real relaxation times around the mean value is α.

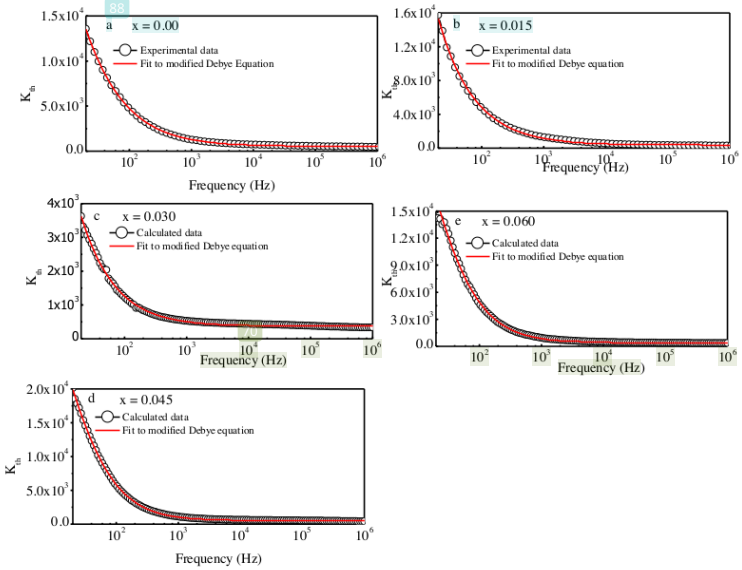


Fig. 4.23 Fitted curve of modified Debye equation of dielectric constant.

Table 4.12 Theoretical dielectric fitting parameters of $Ni_{0.65}Cd_{0.35}Fe_{2-x}Al_xO_4$ bulk ferrites.

Al content	0.00	0.015	0.030	0.045	0.060
ε_{∞}	1.22×10^{5}	85350.67	63278.45	48333.36	41171.33
ε_0	516.80	363.41	373.9	507.15	402.02
τ (s)	1.36×10^{-5}	2.80×10^{-5}	2.64×10^{-5}	1.15×10^{-8}	1.20×10^{-8}
α	0.62	0.62	0.58	0.47	0.48

The spreading factor α ranges from 0 to 1, which is a permissible value [108].

4.7.2 DIELECTRIC LOSS TANGENT

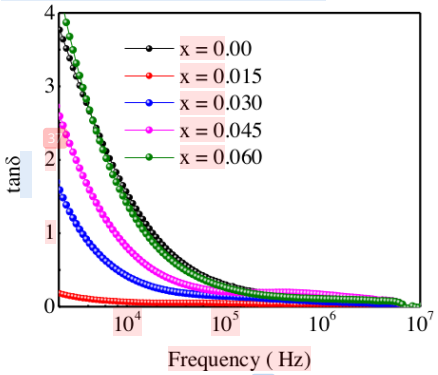


Fig.4.24: Reveals tanδ variation with frequency.

The variations of dielectric loss tangent of $Ni_{0.65}Cd_{0.35}Fe_{2-x}Al_xO_4$ are presented in Fig. 4.23. The tanδ has decreased noticeably with frequency following the substituting of Al on mother sample, and the curve becomes almost linear at frequency of 100 kHz. The graph of the frequency-dependent loss tangent (Fig. 4.24) exhibits a similar trend to the graph of dielectric constants versus frequency (Fig. 22 a and b) [24]. Tanδ has identified the minimal value for x = 0.015.

4.7.3 ELECTRIC MODULUS ANALYSIS

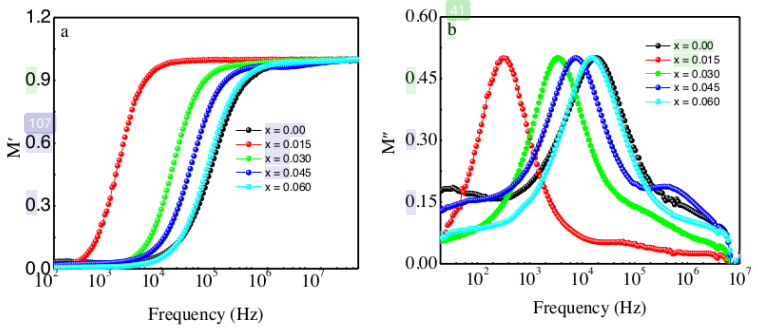


Fig.4.25: Changes of (a) the real portion and (b) imaginary portion of modulus.

The behaviors of the frequency dependence of the real M′ and M″ imaginary components of electric modulus of the ferrites under investigation are illustrated in Fig. 4.25.

Fig. 4.25a is displayed very low value of M′ (close to zero) in the low-frequency area and continuously increases with frequency that reach at maximum value in the high-frequency region at 1MHz for all samples. The real value of M′ remained constant up to 10MHz. The real value M′ reaching its maximum for the compound provides evidence that the relaxation process of voids occurs at high frequencies. Therefore, during conduction, there is a rapid rise in M′ at a high frequency of about 1MHz, which indicates that charge carriers are mobile over short distances. In contrast, the low-frequency zone's minimal values of M′ show that the compound under investigation exhibit a small amount of electrode polarization within their grains [106]. Fig. 4.25 (b) is revealed the relaxation peak, which is caused by the highest conduction loss occurring at the center frequency. On the lower frequency portion of the peak of M″, charge carriers can travel from one site to a nearby site over large distances, but on the higher frequency side, they are constrained to their potential wells and can only travel short distances [3]. It finds that M″ provides low values at lower frequencies; however, when the frequency drive is in the 1 kHz – 10 kHz range, M″ displays broad maxima for the compound. The maxima of M″ for the compound later gradually fall with other higher frequencies to low values. The charge carriers are capable of traveling long distances within the grains at low frequencies and exhibit very high capacitance values [3,108]. In the high-frequency zone, the carriers do not go along the AC fields due to being contained within the potential wells. As a result, the charges travel across short distances. The samples have broad, asymmetric peaks on both sides of the maxima at high frequencies [106].

4.7.4 IMPEDANCE ANALYSIS

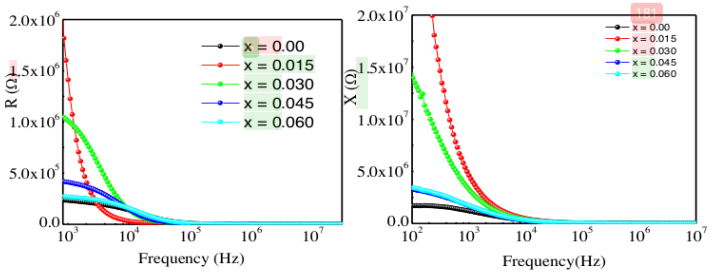


Fig.4.26**:** Demonstrates (a) the real portion and (b) imaginary portion of impedance.

In Fig.4.26, the real part (R) and the imaginary component (X) of the impedance are presented of the Ni-Cd-Al bulk ferrites. The fluctuations in the real (resistive) and imaginary (reactive) portions of the complex impedance spectra are shown in the compositions. Both the real as well as imaginary portions of the impedance were shown to decrease with frequency. The values of R was declined to 10k whereas X at near about 8k. The values of R were became constant at 100k while X after 10k. At higher frequencies, the real component of all the materials seems to blend. The space charge polarization effect in the material may be responsible for the real component decreasing with frequency. The observed larger values of real portion (R) at lower frequencies demonstrates the importance of the grain boundary in the conduction mechanism of the materials under investigation. Consequently, these materials display high impedance in lower frequency range, which is likely caused by the grain boundary, where the formation of Al_2O_3 hinders the grain growth mechanism. The real portion (R) was found to rise with increasing Al content, which can be attributed to the ideal gas behavior of trivalent Aluminum, combined with its tendency to predominantly occupy B sites in the ferrous state, leading to increased resistivity with Al substitution. The imaginary part (X) of plot with frequency was exhibited a comparable pattern to R [10, 14].

4.7.5 Cole - Cole Plot

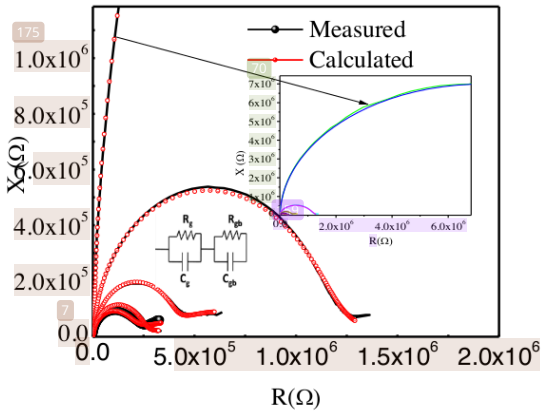


Fig.4.27 Cole-Cole fitted plot of $Ni_{0.65}Cd_{0.35}Fe_{2-x}Al_xO_4$.

In Fig. 4.26, the Cole-Cole plots are depicted the real part (R) alongside the imaginary part (X) impedance of Ni-Cd-Al bulk ferrites. A ferrite material is thought to have a microstructure made up of crystalline parallel conducting plates (grains) that are spaced apart by resistive plates (grain boundaries). Using Zview software, the impedance data are fitted, and the optimal fit is achieved by using an analogous circuit consisting of a grain resistance (Rg) and grain boundary resistance (Rgb) with a parallel combination of grain capacitance (Cg) and grain boundary capacitance (Cgb). The complex impedance that results from the Cole-Cole type of distribution based on a two-layer model is made up of two overlapping semicircles. The plot provides two semicircles as the grain boundary resistance represented by the first semicircle at low frequency, while the resistance of the grain or bulk properties is shown by the second semicircle at high frequency. In the majority of instances, the phenomenon is linked to the existence of a dispersion of relaxation time. The semicircle's size, which varies with grain size and represents the level of resistance. The complex impedance plots can be employed to evaluate the nature of Debye or non-Debye type dielectric relaxation within the system.

The Cole-Cole Plot is displayed semicircles that depressed, having their centers located on a line below the real axis (Z′ axis). This behavior signifies a deviation from ideal Debye behavior. Non-Debye behavior may be attributed to several factors including grain orientation, grain size, distribution, grain boundaries, atomic defect distribution and stress-strain effects, among others [23].

Table 4.13 Grain and grain boundary parameters of $Ni_{0.65}Cd_{0.35}Fe_{2-x}Al_xO_4$.

Al content	$R_g(\Omega)$	C_g(F)	$R_{gb}(\Omega)$	C_{gb} (F)
0.00	2.66×10^{4}	1.97×10^{-9}	2.26×10^{5}	1.21×10^{-10}
0.015	1.92×10^{4}	3.07×10^{-9}	1.41×10^{5}	1.39×10^{-10}
0.030	3.67×10^{5}	7.82×10^{-9}	7.25×10^{9}	3.72×10^{-9}
0.045	5.57×10^{4}	1.09×10^{-10}	4.17×10^{5}	1.07×10^{-6}
0.060	4.04×10^{4}	1.09×10^{-8}	2.32×10^{5}	9.51×10^{-11}

Smaller grain samples display one semicircle, while larger grain samples show two semicircles that correspond to the grain border and grain resistance, respectively [1, 49]. The real portion of impedance in complex impedance diagrams is connected to resistance Zr, whereas the imaginary component has connection to capacitance C, where $Z_r = 1/j\omega C$. Calculating the relaxation period is possible using the formula $\tau_g = C_gR_g$ and $\tau_{gb} = C_{gb}R_{gb}$[8] . This is attributed to a significant increase in electron scattering caused by the disordered atomic arrangement close to the grain boundary area. Furthermore, the concentration of mobile charges may significantly rise as a result of the internal space-charge generated at grain boundaries.

It has been depicted, for all the samples of $Ni_{0.65}Cd_{0.35}Fe_{2-x}Al_xO_4$ in the studied frequency range, that the Cole-Cole plot demonstrates the creation of two semi-circles, grain boundary and grain resistance. The pattern of this curve indicates that the contribution from the grain boundary predominates and that the grain contribution is less demarcated of the sample [105]. The grain resistance, which is substantially less than the grain boundary resistance, is crucial to the conductivity behavior of materials. The grain and grain boundary resistance of the samples is represented by the diameter of the semicircle in the Nyquist plot. In $Ni_{0.65}Cd_{0.35}Fe_{2-x}Al_xO_4$ ferrite, the computed values of grain and grain boundary resistance from these plots revealed that resistance values increasing trend with Al doping [106] as shown in Table 4.13.

4.7.6 AC CONDUCTIVITY

Fig. 4.28 was illustrated the variation in AC conductivity for Ni-Cd-Al bulk ferrites compound at room temperature. It is possible to express the AC conductivity of ferrite materials as $\sigma(\omega,T) = \sigma_{dc}(T) + \sigma_{ac}(\omega,T)$ where the sole temperature-dependent variable is the dc conductivity, which is the first term in the equation. The second term in the equation is the ac conductivity, which is a variable that depends on both temperature and frequency. The formula for this frequency-dependent AC conductivity σac is as follows, $\sigma ac = A\omega^n = \varepsilon'\varepsilon_0 2\pi f \tan\delta$. AC conductivity was found to rise with frequency [107].

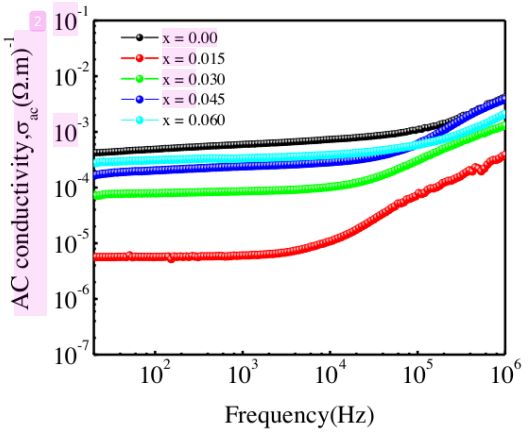


Fig. 4.28 AC conductivity with frequency.

The rise in the ac conductivity of the ferrites with frequency is explained by means of Koop's two-layer model and the space charge. Ferrite materials consist of grains that are highly conductive, which are separated by grain boundaries that possess a resistive characteristic. The grains demonstrate well conductivity at high frequencies but show poor conductivity at a lower frequency due to the hopping of electrons and space charge polarization. As the frequency of the applied field increases, the grains become more dynamic by boosting the hopping between ions, which raises the hopping frequency. Furthermore, the pumping forces of the utilized frequency assist the charge carriers in moving among various localized states and liberate the trapped charges from other trapping centers. Thus, a significant increase in ac conductivities is noted for all the compositions. These hopping charge carriers have a strong correlation with the conduction mechanism and dielectric behavior [24]. The σ_{ac} reduces as the Al content is increased with the steps x = 0.015. The phenomena can be clarified by stating that the Al ions reside in the octahedral sites within the mixed Ni–Cd ferrite, reducing the quantity of Fe present at the octahedral site. The reduction in conductivity with Al content is attributed to a decrease in Fe^{3+} ion concentration at the B site, which restricts the ability to hop between Fe^{3+} and Fe^{2+} ions.

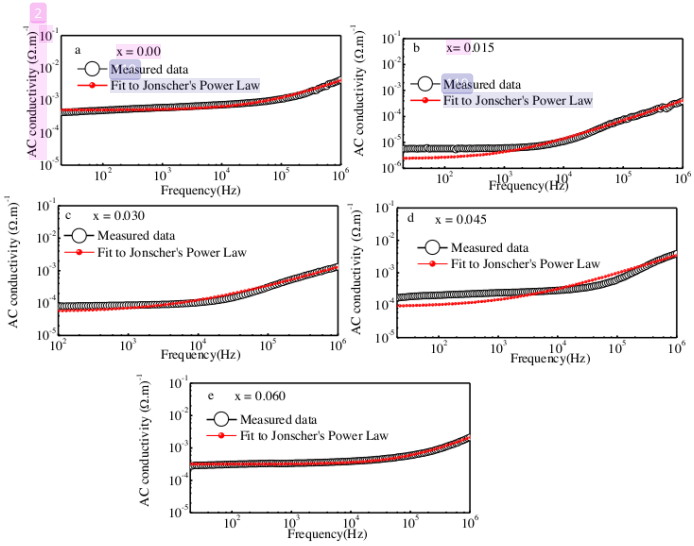


Fig 4.29 Fitting to Jonscher's Law of AC conductivity

The distance of B-B site is shorter than that of the A site and B site. As a result, the probability of electrons exchanging between B-B sites is lower than A-A and A-B sites. Substitution of nonmagnetic Al^{3+} ions for Fe^{3+} in mother compound was found to impede conductivity due to effect of Verwey's hopping process [22, 99]. The theoretically calculated AC conductivity was plotted with frequency and subsequently fitted to the Jonscher's Power Law to justify the experimental results [108].

CHAPTER 5

CONCLUSIONS

Chapter 5: CONCLUSIONS

5.1 GENERAL

In these investigations, we have been studied the influence of Al substitution on the structural, elastic, magnetic, magnetocaloric, optical, dielectric and electrical properties of Ni-Cu-Al dense ferrite with formula $Ni_{0.65}Cd_{0.35}Fe_{2-x}Al_xO_4$

5.2 KEY FINDINGS

The acquired results could be used to mention the following important conclusions;

- The series of Ni-Cd-Al bulk compound have been successfully prepared by sintering at 1423K using sol gel technique from nano-crystallite powders. Utilizing X-ray diffraction technique, structural with Rietveld refinement analyses such as goodness of fit, cation distribution, maximum entropy approach properties have been explored.
- The single-phase homogenous cubic spinel structure is confirmed by XRD and Rietveld refinement analysis. Cation distribution reveals Al substitution in Ni-Cd-Al bulk compound, is shown to occupy on both A and B sites, though slightly larger in the tendency towards A-sites.
- Goodness of fit 1.86 to 2.75 has been obtained from Rietveld refinement analysis. Ni, Al and Fe were found to strong preference for the B site, whereas Fe and Cd were found to occupy the A site from the cation distribution study.
- The strong covalent bond is found to increase from the electron density method with Al substitution.
- The crystalline sizes is observed to decrease using Scherer's formula, Modified Scherer's formula, Williamson-Hall plot, and Size Strain Method (SSM) as well as XRD analysis.
- Interatomic distances of bond length are decreased with Al as well as bond strength increased.
- Bond angles of θ_1 and θ_2 are calculated as a decreasing tendency corresponds with the A-B exchange interaction weakened. On the other hand, bond angles of θ_2 , θ_3 and θ_5 are found to increasing as well as the B-B and A-A interaction goes stronger with Al content.
- Elastic properties including force constant, stiffness constant, elastic moduli, wave velocities and Debye temperature are analyzed and found to decrease with Al content.

- Grain sizes is found to decrease with Al from surface morphology study.
- The saturation magnetization is found to increase initially and then decline with Al due to effect of canting angle. The values of M_s have found to increase initially with Al content as well as supported by the LAS fitting curves.
- Curie temperature (T_c) has been observed to decrease from (582.27 to 578.76) K.
- RCP values have been recorded to be the range of (43.18 - 56.97) Jkg^{-1} of Ni-Cd-Al bulk with Al content which might be consider them a appropriate materials for magnetic refrigeration.
- Refractive index (n) and extinction coefficient are determined with Al from optical study.
- High frequency ranges is observed from initial permeability.
- The dielectric constant, the dielectric loss tangent and AC conductivity are found to decrease with Al.
- Low cost, low temperature dense ceramic fabrication as well as better various properties might be applied for multifunctional devices.

LIMITATION OF THE STUDY

Due to lack of proper availability of characterization facility of various instruments like XRD, FESEM, PPMS etc. practical handling was limited during research time.

PRACTICAL IMPLICATION

The result has found potential for Magnetic Refrigeration as it provided great value of Relative Cooling Power.

RECOMMENDATION FOR FURTHER STUDY

Temperature Dependent magnetization needs to be done on various magnetic field (i.e. 1T to 5T) to obtain optimum for RCP values and to get certainty on being applicable as Magnetic refrigerant. Also, P-E hysteresis loop and and Mossbauer spectra analysis is required to obtain clear image of this research.

BIBLIOGRAPHY

[1] M. A. Mannan & M. B. Hossen, J. Mater. Sci.: Mater. 32, 24524 – 24539, (2019) .

[2] M. M. Rahman, N. Hasan, M. A. Hoque, M. B. Hossen, M. Arifuzzaman, Results in Phys. 38,105610 , (2022).

[3] J. Massoudi, M. Smari, K. Nouri, E. Dhahri, K. Khirouni, S. Bertaina, L. Bessais , E. K. Hlil, RSC Adv. 10, 34556–34580, (2020).

[4] S. K. Nath, K. H. Maria, S. Noor, S. S. Sikder, S. M. Hoque, & M. A. Hakim, J. Magn. Magn. 324, 2116–2120, (2012).

[5] M. M. Eltabey, K.M. El-Shokrofy, S.A. Gharbia, J. Alloys Compd, 509(5), 2473-2477, (2011).

[6] M. A. Munir, M. Y. Naz, S. Shukrullah, M. T. Ansar, M. U. Farooq, M. Irfan, S. N. F. Mursal, S. Legutko , J. Petr, M. Pagac, Materials. 15, 6890 (2022).

[7] R. Valenzuela, T. Gaudisson, S. Ammar, J. Magn. Magn. Mater., 400, 311-314 (2016).

[8] N. Ponpandian & A. Narayanasamy, J. Appl. Phys., 2770–2778, (2002).

[9] S. Hasan, & B. Azhdar , Adv. Condens. Matter Phys. 2022, 1-4, (2022).

[10] M. B. Hossen, A. K. M. A. Hossain. J. Magn. Magn. Mater, 387, 24–36 (2015).

[11] A.Yadav, P. Choudhary, P. Saxena, V. N. Rai, & A . Mishra , J. Adv. Dielectr. 9(2), 1–12, (2019).

[12] S. Bahhar , A. Boutahar , L.H. Omari , H. Lemziouka , E.K. Hlil , H. Bioud , E. Dhahri , J. Magn. Magn. Mater, 539, 168416 (2021).

[13] M. M. Eltabey, A. M. Massoud, H. M. Mohamed, IJARPS, 3, 4, 13-20 , ISSN 2349-7874 (Print) & ISSN 23497882, (2016).

[14] S. K. Ahmed, M. F.Mahmood, M.Arifuzzaman & M.B. Hossen, Results in Phys. 30, 104833, (2021).

[15] S. Aghav , V. N. Dhage , M. L. Mane , D.R. Shengule , R.G. Dorik , K. M. Jadhav, Physica B 406 4350–4354,(2011).

[16] S. U.Rather , O.M. Lemine, J. Alloys Compd. 812 , 152058, (2020).

[17] N. Murali , S.J. Margarette , G. Pavan Kumar , B. Sailaja , S. Y.Mulushoa , P. Himakar , B. Kishore Babu , V. Veeraiah, Physica B 522 1–6,(2017).

[18] L. Z. Li, X. X. Zhong, R. Wang, X.Q.Tu, L. He, R.D. Guo and Z.Y. Xuc, RSC Adv., 7, 39198, (2017).

[19] Muniba, M. Khalid, A. D. Chandio, M. S. Akhtar, J. K. Khan, G. Mustafa, N.U.Channa, Z, A, Gilani, and H. M. N.U. H. K.Asghar, J. Electron. Mater., 50, 3302–3311, (2021).

[20] I. H. Gul , A. Maqsood, M. Naeemb, M. N. Ashiq,J. Alloys Compd. 507 , 201–206, (2010). M. Arifuzzaman, M. B. Hossen, Results Phys. 16 (2020).

[21] M. S. Khan , A. Bagum , M. F. Mahmood , N. Mohammed , M. B. Hossen, J. Magn. Magn. Mater. 603, 172263(2024).

[22] K. M. Batoo, S. Kumar, C. G. Lee, Alimuddin,Curr. Appl. Phys., 9(5), 1072–1078, (2009).

[23] M. B. Hossen, A. K. M. A. Hossain, ICIEV, pp. 903-907, (2012).

[24] N. Jahan, M. N. I. Khan, M. R. Hasan, M. S. Bashar, A. Islam, M. K. Alam, M. A. Hakim J. I. Khandaker, RSC Adv. 12(24), 15167–15179, (2022).

[25] J. Sures, B.V. Babu, A.R. Krisna, P.V.S.S.N. Reddy, B. Trinadh, B. S. Mohan, K. E. Rao, K. Samatha, Chin. J. Phys. 80,334–348,(2022).

[26] S. Sharma, R. Verma, M. Singh, S. K .Sharma, Cham. 21, 41-62,(2021).

[27] G.K. Bhargava, P.Sharma, S. Bharwaj, I.Sharma, Materials Research Forum LLC ,142, 218, (2023).

[28] T. N. Pham, T. Q. Huy, A. T. Le, RSC Adv., 10, 31622-31661,(2020).

[29] S.J. Salih, W.M.Mahmood, . Heliyon, 26; 9(6): e16601,(2023).

[30] N. Thakur, I. Sharma, P.Thakur, Spinel ferrite materials, Fundamentals, Progress, and Applications,1-30, (2025)

[31] https://www.shutterstock.com/image-illustration/tetrahedral-octahedral-sites-cubic-facecentered-crystal-345228092.

[32] M. A.Wahab, Solid State Physics: Structure and Properties of Materials, Narosa Publishing House, New Delhi (1999).

[33] A. R. Liandi, A.H. Cahyana, A.J.F. Kusumah, A. Lupitasari, D.N. Alfariza, R. Nuraini, R.W.Sari, F.C.Kusumasri, Case Studies in Chem.and Environ. Engineering, 7, 2023, 100303,(2023).

[34] S. Gaffar, A.Kumar, U.Riaz, J. Electrocerm. 51, 246–257, (2023).

[35] B-H curve, Magnetic hysteresis curve experiment, https://www.holmarc.com/B-H_curve_experiment.php.

[36] P. Guimarães , Albert , Principles of Nanomagnetism, Springer-Verlag Berlin Heidelberg , 2009.

[37] Magnetocrystalline anisotropy, Wikipedia.

[38] B. D. Cullity, C. D. Graham, Introduction to Magnetic materials, 2nd edition , John Wiley & Sons, Inc., Hoboken, New Jersey, 2009.

[39] Magnetocaloric effect, Wikipedia, https://en.wikipedia.org/wiki/Magnetocaloric_effect.

[40] K. Shankland, J. Res. Natl. Inst. Stand. Technol. 109, 143, (2004).

[41] UV-Vis Spectroscopy: Principle, Strengths and Limitations and Applications, Technology Networks, (2023).

[42] C. Dwivedi , I, Pandey , H. Pandey , Pramod W. Ramteke , A. C. Pandey , S. B. Mishra , S. Patil, Nano- and Microscale Drug Delivery Systems Design and Fabrication , Chap. 9, 147-164, (2017).

[43] M. J. Kadhim, A. K. Abdullah, I. A. Al-Ajaj, and A. S. Khalil, IJAIEM, ISSN 2319 – 4847,(2014).

[44] N. Channa, M. Khalid, A. D. Chandio, G.Mustafa, M. S.Akhtar, , Kareem, J.K.Khan, J.Ahmed , K. A., Kalhoro, J. Mater. Sci. Mater. Electron. 31, 1661-1671,(2020).

[45] M.B. Mohamed , A.M. Wahba , Ceram. Int. 40,8, 11773-11780, (2014).

[46] J. Suresh, B.V.Babu, A. R. Krishna, P.V.S.S.S.N Reddy, Trinadh, B. S. Mohan, K. E. Rao, K. Samatha, Chin. J. Phys. , 80, 334-348, (2022).

[47] N. Suo, A.Sun, L,Yu, Z, Zuo, X, Zhao,W, Zhang,Y. Zhang, L. Shao, Z. Dang, Appl. Phycs. A 126:183, (2020).

[48] Y. Zhang ,C.Yuan,A.Sun, J Mater Sci: Mater Electron, 33,15495–15508, (2022).

[49] M. W. Nafees , M. U Islam, M. Ajmal, M. Hussain , A. Iftikhar and S. Naseem, Mater. Res. Express, 6 , 126121, (2019).

[50] L. Z. Li, X.X. Zhong, R. Wang, X.Q. Tu, L. He, R.D. Guo, Z.Y. Xuc, RSC Adv. 7, 39198, (2017).

[51] M. M. Costa, G. F. M. Pires Júnior, A. S. B. Sombra, Mater. Chem. Phys. 123, 35, (2010).

[52] M. A. Gabal, J. Magn. Magn. Mater. 321, 3144, (2009).

[53] M. F. Kuo, Y. H. Hung, J.Y. Huang, C. C.Huang, AIP Advances 7, 056104, (2017).

[54] N. Jahan , M. N. I. Khan , M. R. Hasan , M. S. Bashar , A. Islam , M. K. Alam , M. A. Hakim & J. I. Khandaker , ACS omega ,6 , 32852- 32862, (2021).

[55] S. Solyman, H.M. Zaki, S. Soliman, Matter. Chem. Phys., 279, 125723, (2022).

[56] S. Gul , M. A. Yousufa , A. Anwara , M. F. Warsi. , P.O Agboolab , I. Shakirc , M. Shahid., Ceram. Int. 46, 14195-14205, (2020).

[57] M.M. Eltabey, A.M. Massoud, H.M. Mohamed, IJARPS 3(4), 13–20, (2016)

[58] S. Hassan , M. Ahmad , A. Rehman , M. W. Iqbal , S.F. Shaukat , Hisham S.M. Abd-Rabboh, J. energy Storage, 55, 105320, (2022).

[59] P. B. Wasnik, K. G. Rewatkar, S.M.Suryawanshi, M. S. Bisen, S.D.Rokade, Nano-Structures & Nano-Objects, 39, 101325,(2024).

[60] E. A. Arrasheed, , Y. A Alibwaini,, T M Meaz , A.W.Ajlouni, R M Shalaby , O M Hemeda and A M A Henaish, Phys. Scr. 97 ,115701, (2022).

[61] B. Rabil, A. Essoumhi, M. Sajieddine, E.K. Hlil, A. Razouk, R. Moubah, H. Lassri, J. Supercond. Nov. Magn. 33, 2527–2534, (2020) .

[62] X-ray diffraction, https://www.britannica.com/science/crystallography.

[63] U.D. Das, J.U. Ahmed, M.A. M. Hossain, M.E.A Razzaq, S. Dewanjee, and R.N. Jisu, Mech. Eng. J. 12, 19-29(2020).

[64] N. Channa, M. Khalid, A.D. Chandio, G. Mustafa, M.S. Akhtar, J.K. Kareem, J. Ahmed, K.A. Kalhoro. J. Mater. Sci. Mater. Electron. 31, 1661–1671, (2020).

[65] N. Channa, M. Khalid, A.D. Chandio, M.S. Akhtar, J.K. Khan, G. Mustafa, Muniba, ZA Gilani, J. Mater. Sci. Mater. Electron. 32, 2832–2844 (2021).

[66] M. A. Islam, A. K. M. Akther Hossain, M. Z. Ahsan, M. A. A. Bally, M. Samir Ullah, S. M. Hoque , F. A. Khan, RSC Adv., 12, 8502, (2022).

[67] T. D. Thanh, T. T. N. Nha, T. T. H. Giang, P. H. Nam, D. N. Toan, D. T. Khan, D.H.Manh, P. T. Phong, RSC Adv., 14, 23645, (2024).

[68] F. Fakhry, E. Shaheen, H. El-Dosoky,T. M. Meaz, M. Mubark, R. El-Shater, Scientific Reports, 14:29407, (2024).

[69] N. Amri, J. Massoudi, K. Nouri, M. Triki,E. Dhahri , L. Bessais,RSC Adv., 11, 13256,(2021).

[70] S. A. Mazen and T. A. Elmosalami,ISRN Condensed Matter, 820726,9,(2011).

[71] M. H. Abdellatif and A. A. Azab, BNRC, 43:111, (2019).

[72] M. M. El-Masry, A. E. Mahmoud, H. Y. Morshidy, R. Ramadan,J Mater Sci: Mater Electron, 34:383,(2023).

[73] T.Ş Kuru, V. Eyüpoğlu, F. Yıldız,Acta Phys. Pol. 134(1092), 1098 (2018).

[74] P. Soltanpour , R. Naderali & Kh. Mabhouti, Scientific Reports, 14,21287,(2024).

[75] F. Alam, M. L. Rahman, M. H. R. Khan, A. K. M. A. Hossain, J. Mod. Phys., 05(14), 1223–1233, (2014).

[76] K. Shahzadi, A. D. Chandio, G. Mustafa, M. Khalid, J. K. Khan, M. S. Akhtar, Z. A. Gilani,, & Asgar, H. M. N. H. Khan, Opt. Quantum Electronics. 52, 1–17, (2020).

[77] A. Birajdar, S.E. Shirsath, R.H. Kadam, M.L. Mane, D.R. Mane, A.R. Shitr, J. Appl. Phys. 112(5), 053908, (2012).

[78] M.F. Mahmood, M.B. Hossen, J. Mater. Sci. Mater. Electron. 32, 14248–14273, (2021)

[79] S. Sachdeva , N. Budhiraja, V. Kumar, V., S. K. Singh, J. Adv. Phys., 6(4), 492–495,(2018).

[80] A.B. Kulkarni, S.N. Mathad (2018), International Journal of Self-Propagating High-Temperature Synthesis, 27(1), 37–43, (2018).

[81] K.M. Batoo, Nanoscale Res. Lett. 6, 1–7, (2011).

[82] J.K. Khan, M. Khalid, A.D. Chandio, K. Shahzadi, Z. Uddin, G. Mustafa, M.S. Akhtar, N. Channa, Z.A. Gilani, , J. Sol-Gel Sci. Technol. 101, 606–617, (2022).

[83] K. Dubey, S. Dubey, V. Sahu, R. A.Parry, A. Modi, , & N. K. Gaur , Appl. Phys. A: Mater. Sci. Process. 128, 1–11, (2022).

[84] N. Abinaya, M.C. Robert, N. Srinivasan, S. Saravanakumar, J. Magn. Magn. Mater. 580, 170938, (2023).

[85] M.M. Khalid, A.D. Chandio, M.S. Akhtar, J.K. Khan, G. Mustafa, N.U. Channa, Z.A. Gilani, H.M.N.U.H.K. Asghar, J. Electron. Mater. 50, 3302–3311, (2021).

[86] N. Nazari , M. M. Golzan , Kh. Mabhouti, Scientific Reports 14, 6407, (2024).

[87] P. G. Undre, A. V. Humbe, J. S. Kounsalye , A. Kumar, R. V. Kathare, K. M. Jadhav, J. Inorgan. Organomet. Polym. Mater 33, 3372–3388, (2023).

[88] Z. Karimi , Y. Mohammadifar, H. Shokrollahi, Sh. Khameneh Asl, Gh. Yousefi, L. Karimi, J. Magn. Magn. Mater., 361, 150–156,(2014).

[89] N. Mohammed, A. Bagum , M. S. Khan and M. B. Hossen , Applied Physics A : Materials Science and Processing, 131, 216, (2025).

[90] D.N. Dipesh, L. Wang, H. Adhikari, J. Alam, S.R. Mishra, J. Alloys Compd. 688(413), e421, (2016).

[91] P.J.V.D. Zaag, P.J.V.D. Valk, MTh. Rekveldt, Appl. Phys. Lett. 69, 2927–2929, (1996).

[92] R.B. Kamble, V. Varade, K.P. Ramesh, V. Prasad,. AIP Adv. 539(108), 17119–84321, (2015).

[93] J.A. Paulsen, C.C.H. Lo, J.E. Snyder, A.P. Ring, L.L. Jones, D.C. Jiles, IEEE Trans. Magn. 39(5), 3316–3318, (2003).

[94] M.A. Islam, A.K.M.A. Hossain, RSC Adv. 12, 17362–17378, (2022).

[95] A. Aslam , N.A. Morley , N. Amin , M. I. Arshad , M. A. Nabi , A. Ali , K. Mahmood , A. Bibi , F. Iqbal , S. Hussain , Y. Jamil, Physica B: Cond.Mattr., 602. 412565, (2021).

[96] N. Kouki, S. Hcini, M. Boudard, R. Aldawas, A. Dhahri, RSC Adv. 9, 1990–2001, (2019).

[97] M.S. Anwar, B.H. Koo, Appl. Phys. A 128, 580, (2022).

[98] M. A. Ali, M. N. I. Khan, F. U. Z. Chowdhury, M. M. Hossain, A. K. M. A. Hossain, R. Rashid, , A. Nahar, S. M. Hoque, M. A. Matin, M. M. Uddin, J. Mater. Sci.: Mater. , 30(14), (2019).

[99] Islam, M. A., Rahaman, M. Z., Hasan, M. M., & Hossain, A. K. M. A. (2019). Heliyon, 5(2), e01199, (2019).

[100] M. Mostafa,,O. Saleh, A.M. Henaish, S.A.A El-Kaream, R. Ghazy, O.M. Hemeda, A.M. Dorgham, H. Al-Ghamdi, A.H. Almuqrin, M.I. Sayyed, S.V.Trukhano, E.L.Trukhanova, A.V. Trukhanov, D. Zhou, M. A. Darwish, (2022), Nanomater., 12(7), (2022).

[101] M. Z. Ahsan, F. A. Khan, M. A. Islam, T. Tabassum, M. K. Alam, Commun. Phys , 2(10), 105008, (2018).

[102] K. V. Kumar, D. Paramesh, P. V. Reddy, W. J. nano sci. Engn., 5 (3), (2015).

[103] Q. Khan, A. Majeed , N. Ahmad, I.Ahmad , R. Ahmad, Mater.Chem. Phys., 15, 125028, (2021).

[104] K. Naz, J. K. Khan, M. Khalid, M. S. Akhtar, Z. A. Gilani, H. M. N.H. K. Asghar, G. A. M. Mersal, M. M Ibrahim, A. Muhammad, M. G. B. Ashiq, Mater. Chem. Phys. 285,126091, (2022).

[105] A. Selmi, S. Hcini, H. Rahmouni, A. Omri, M. L Bouazizi, A. Dhahri, Phase Transitions, 90(10), 942–954 (2017).

[106] A. Loganathan, K. Kumar, Applied Nanoscience (Switzerland), 6(5), 629–639(2016).

[107] E. R Kumar, R. Jayaprakash, T. Arunkumar, S. Kumar, J. Phys. Chem. Solids 74, 110–114, (2013).

[108] N. Jahan, M. I. Khan, J.I. Khandaker, ACS Omega, 6, 32852−32862,(2021).

BIBLIOGRAPHY

Final_Thesis_-_Copy_1.pdf

ORIGINALITY REPORT

24%	15%	20%	5%
SIMILARITY INDEX	INTERNET SOURCES	PUBLICATIONS	STUDENT PAPERS

PRIMARY SOURCES

1	link.springer.com Internet Source	2%
2	lib.buet.ac.bd:8080 Internet Source	1%
3	pubs.rsc.org Internet Source	1%
4	Submitted to University of Warwick Student Paper	1%
5	M. Faishal Mahmood, M. Belal Hossen. "Dynamic response of electrical, dielectric and magnetic properties of La-substituted Ni-Cu-Cd bulk ceramics with structural rietveld refinement", Journal of Materials Science: Materials in Electronics, 2021 Publication	1%
6	Md. Shahbaz Khan, Arjumanara Bagum, M. Faishal Mahmood, Nur Mohammed, M. Belal Hossen. "Effects of Mg substitution on the structural with Rietveld Analysis, magnetic and magnetocaloric properties of Ni-Cu-Cd bulk ceramics", Journal of Magnetism and Magnetic Materials, 2024 Publication	1%
7	Submitted to Higher Education Commission Pakistan Student Paper	<1%
8	irgu.unigoa.ac.in Internet Source	<1%

9	etheses.saurashtrauniversity.edu Internet Source	<1%
10	M. Abdul Mannan, M. Belal Hossen. "Dynamic electric, modulus and impedance study of Ni0.5Cu0.2Cd0.3Fe2-zAlzO4 nanoparticles with magnetization and Rietveld analysis", Journal of Materials Science: Materials in Electronics, 2021 Publication	<1%
11	www.skmg.ac.in Internet Source	<1%
12	Mohamed, Mohamed Bakr, and Adel Maher Wahba. "Structural, magnetic, and elastic properties of nanocrystalline Al-substituted Mn0.5Zn0.5Fe2O4 ferrite", Ceramics International, 2014. Publication	<1%
13	discovery.researcher.life Internet Source	<1%
14	Alberto P. Guimarães. "Principles of Nanomagnetism", Springer Science and Business Media LLC, 2017 Publication	<1%
15	Md. Arman Hossain, Hasan Khaled Rouf, Murad Hossain, Mohammad Khurshed Alam, Mohammed Nazrul Islam Khan. "Synthesis and exploration of structural, optical, magnetic, and electrical properties of Ti-doped Mn–Ni–Zn ferrite", AIP Advances, 2025 Publication	<1%
16	pdfcookie.com Internet Source	<1%

17	M.M. Rahman, N. Hasan, M.A. Hoque, M.B. Hossen, M. Arifuzzaman. "Structural, dielectric, and electrical transport properties of Al3+ substituted nanocrystalline Ni-Cu spinel ferrites prepared through the sol–gel route", Results in Physics, 2022 Publication	<1 %
18	hal.archives-ouvertes.fr Internet Source	<1 %
19	dokumen.pub Internet Source	<1 %
20	teses.usp.br Internet Source	<1 %
21	Mohd. Hashim, Alimuddin, Shalendra Kumar, Sikander Ali, B.H. Koo, H. Chung, Ravi Kumar. "Structural, magnetic and electrical properties of Al3+ substituted Ni–Zn ferrite nanoparticles", Journal of Alloys and Compounds, 2012 Publication	<1 %
22	Pallavi G. Undre, Ashok V. Humbe, Jitendra S. Kounsalye, Arun Kumar, R. V. Kathare, K. M. Jadhav. "Diamagnetic Al3+ Doped Ni–Zn Spinel Ferrite: Rietveld Refinement, Elastic, Magnetic, Mössbauer, and Electrical Explorations", Journal of Inorganic and Organometallic Polymers and Materials, 2023 Publication	<1 %
23	core.ac.uk Internet Source	<1 %
24	Submitted to Corporación Universitaria del Caribe Student Paper	<1 %

25	Sanjeet Kumar Paswan, Pawan Kumar, Suman Kumari, Subhadeep Datta, Manoranjan Kar, J.P. Borah, Lawrence Kumar. "Temperature dependent magnetic and electrical transport properties of lanthanum and samarium substituted nanocrystalline nickel ferrite and their hyperthermia applications", Journal of Alloys and Compounds, 2023 Publication	<1 %
26	arxiv.org Internet Source	<1 %
27	M.D. Hossain, M.N.I. Khan, A. Nahar, M.A. Ali, M.A. Matin, S.M. Hoque, M.A. Hakim, A.T.M.K. Jamil. "Tailoring the properties of Ni-Zn-Co ferrites by Gd3+ substitution", Journal of Magnetism and Magnetic Materials, 2020 Publication	<1 %
28	Submitted to Oxford & Cherwell Valley College Student Paper	<1 %
29	dspace.ncl.res.in:8080 Internet Source	<1 %
30	www.preprints.org Internet Source	<1 %
31	M. Arifuzzaman, M. Belal Hossen. "Effect of Cu substitution on structural and electric transport properties of Ni-Cd nanoferrites", Results in Physics, 2020 Publication	<1 %
32	N. Hasan, S.S. Nishat, S. Sadman, M.R. Shaown, M.A. Hoque, M. Arifuzzaman, A. Kabir. "Magnetic, optoelectronic, and rietveld refined structural properties of Al3+ substituted nanocrystalline Ni-Cu spinel	<1 %

ferrites: An experimental and DFT based study", Journal of Magnetism and Magnetic Materials, 2023
Publication

33	Submitted to Universiti Teknologi Malaysia Student Paper	<1%
34	Submitted to University of Basrah - College of Science Student Paper	<1%
35	etheses.whiterose.ac.uk Internet Source	<1%
36	Raghupathi Ganta, Mainampati Srinivasa Reddy. "Effect of erbium ion doping on Mg–Co nano ferrites: A study on structural, optical, elastic, electric and magnetic properties", Journal of the Indian Chemical Society, 2025 Publication	<1%
37	Yue, Z.. "Magnetic and electrical properties of low-temperature sintered Mn-doped NiCuZn ferrites", Journal of Magnetism and Magnetic Materials, 200308 Publication	<1%
38	Submitted to Bharathidasan University, Tiruchirappalli Student Paper	<1%
39	KRUTIKA LOKAPRIYA ROUTRAY, Sunirmal Saha. "Investigation of structural, electrical, and magnetic variations of Ni-Zn-Co ferrites by substituting rare earth Ho3+ for high-frequency applications", Physica Scripta, 2024 Publication	<1%
40	M. Faishal Mahmood, M. Belal Hossen. "Rietveld refinement and complex dielectric, modulus and impedance study of	<1%

Ni0.27Cu0.10Zn0.63AlxFe2-xO4 bulk ceramics", Results in Physics, 2024
Publication

41	Submitted to University of Sheffield Student Paper	<1%
42	S. Bahhar, A. Boutahar, L.H. Omari, H. Lemziouka, E.K. Hlil, H. Bioud, E. Dhahri. "Structural, magnetic and magnetocaloric properties of TMCeFeO4 (TM=Mn, Co) spinel ferrites powders", Journal of Magnetism and Magnetic Materials, 2021 Publication	<1%
43	hdl.handle.net Internet Source	<1%
44	M. Belal Hossen, A.K.M. Akther Hossain. "Influence Of Al3+ Substitution On Impedance Spectroscopy Studies Of Ni0.27Cu0.10Zn0.63AlxFe2-xO4", Advanced Materials Letters, 2015 Publication	<1%
45	Priyanka Kashid, S.N. Mathad, Mahadev R. Shedam, Amita Somya, AbuZar Ansari, Mohamed Hashem, Majed M. Alsarani, Omar Alageel. "Facile fabrication and grain-size depended on structural behavior of Cadmium-Substituted nano Co-Ni ferrites by chemical method", Ain Shams Engineering Journal, 2023 Publication	<1%
46	S.A. Mamun, Mithun Kumar Das, K.S. Uddin, T. Ahamed, Mohammad J. Miah. " Structural, morphological, dielectric, electric and magnetic properties of ceramics for multifunctional applications ", Heliyon, 2024 Publication	<1%

47	O. Amorri, M. Khalfa, R. Jemai, J. Horchani, L. Bessais, K. Khirouni. "Structural, optical electrical and magnetic properties of Zn0.5Mg0.5Fe2O4 ferrite", Inorganic Chemistry Communications, 2025 Publication	<1 %
48	S. Solyman, H.M. Zaki, S. Soliman. "Investigation of structural, magnetic and electrical properties of aluminum substituted Co-Mg ferrite", Materials Chemistry and Physics, 2022 Publication	<1 %
49	Submitted to Universiti Putra Malaysia Student Paper	<1 %
50	uol.de Internet Source	<1 %
51	www.researchgate.net Internet Source	<1 %
52	Atul Thakur, Ritesh Verma, Fayu Wan, Blaise Ravelo, Irina Edelman, Sergei Ovchinnikov, Preeti Thakur. "Investigation of structural, elastic and magnetic properties of Cu2+ ions substituted cobalt nano ferrites", Journal of Magnetism and Magnetic Materials, 2023 Publication	<1 %
53	Bishakar Sharma, M. Belal Hossen. "Radiation-induced structural and electric properties of Al-substituted NiCuCd nanoparticles", Journal of Materials Science: Materials in Electronics, 2022 Publication	<1 %
54	Muniba, Muhammad Khalid, Ali Dad Chandio, Muhammad Saeed Akhtar et al. "Aluminum Substitution in Ni-Co Based Spinel Ferrite	<1 %

Nanoparticles by Sol–Gel Auto-Combustion Method", Journal of Electronic Materials, 2021
Publication

55	c.coek.info Internet Source	<1 %
56	eprints.whiterose.ac.uk Internet Source	<1 %
57	R. Mguedla, A. Ben Jazia Kharrat, N. Moutia, K. Khirouni, N. Chniba-Boudjada, W. Boujelben. "Gd doping effect on structural, electrical and dielectric properties in HoCrO3 orthochromites for electric applications", Journal of Alloys and Compounds, 2020 Publication	<1 %
58	Ramesh B. Kamble, Vaibhav Varade, K. P. Ramesh, V. Prasad. "Domain size correlated magnetic properties and electrical impedance of size dependent nickel ferrite nanoparticles", AIP Advances, 2015 Publication	<1 %
59	www.science.gov Internet Source	<1 %
60	M.A.A. Bally, F.A. Khan. "Structural, dielectric and magnetic properties of La0.55Sr0.45MnO3 polycrystalline perovskite", Journal of Magnetism and Magnetic Materials, 2020 Publication	<1 %
61	Amna Tariq, Kiran Mehmood, Aamir Shahzad, Hamayl Asim, Saira Tariq, Qurat Ul Ain Asif. "Role of Cr-dopant in tuning the properties of Mg-Ni ferrites nanoparticles synthesized by sol-gel auto combustion method for	<1 %

applications in electronic device", Materials Today Communications, 2025
Publication

62	M. Moazzam Hossen, M. Belal Hossen. "Study of structural and electrical properties along with magnetic properties of Ni0.5−xMgxCu0.2Cd0.3Fe2O4 nanoferrites synthesized by employing sol–gel auto-combustion method", Journal of Materials Science: Materials in Electronics, 2019 Publication	<1 %
63	M.H. Rashid, A.K.M. Akther Hossain. "Structural, morphological and electromagnetic properties of Sc3+ doped Ni-Cu-Zn ferrites", Results in Physics, 2018 Publication	<1 %
64	Nusrat Jahan, M. N. I. Khan, M. R. Hasan, M. S. Bashar, A. Islam, M. K. Alam, M. A. Hakim, J. I. Khandaker. " Correlation among the structural, electric and magnetic properties of Al substituted Ni–Zn–Co ferrites ", RSC Advances, 2022 Publication	<1 %
65	Ruqayya Zakir, Sadia Sagar Iqbal, Atta Ur Rehman, Sumaira Nosheen, Tasawer Shahzad Ahmad, Nimra Ehsan, Fawad Inam. "Spectral, electrical, and dielectric characterization of Ce-doped Co-Mg-Cd spinel nano-ferrites synthesized by the sol-gel auto combustion method", Ceramics International, 2021 Publication	<1 %
66	S. M. Patange, Sagar E. Shirsath, G. S. Jangam, K. S. Lohar, Santosh S. Jadhav, K. M. Jadhav. " Rietveld structure refinement, cation distribution and magnetic properties of Al	<1 %

substituted NiFe O nanoparticles ", Journal of Applied Physics, 2011
Publication

67	Tran Thi Ngoc Nha, Dang Ngoc Toan, Pham Hong Nam, Do Hung Manh, Dinh Thanh Khan, Pham Thanh Phong. "Determine elastic parameters and nanocrystalline size of spinel ferrites MFe2O4 (M = Co, Fe, Mn, Zn) through X-ray diffraction and infrared spectrum: Comparative approach", Journal of Alloys and Compounds, 2024 Publication	<1 %
68	V. Lakshmi Savithri Vatsalya, G. Sunita Sundari, ChS.L.N. Sridhar, M. Durairaj, T.C. Sabari Girisun, ChS. Lakshmi. "Exploring nonlinear optical absorption in cobalt-doped Nickel–Zinc nanomaterials", Materials Chemistry and Physics, 2024 Publication	<1 %
69	ethesis.nitrkl.ac.in Internet Source	<1 %
70	Submitted to Ganpat University Student Paper	<1 %
71	Reddy, M.P.. "Influence of copper substitution on magnetic and electrical properties of MgCuZn ferrite prepared by microwave sintering method", Materials Science & Engineering C, 20101012 Publication	<1 %
72	doctorat.ubbcluj.ro Internet Source	<1 %
73	Submitted to Aga Khan Education Service, Bangladesh Student Paper	<1 %

74	Anuja Dhingra, O. P. Thakur, Raghvendra Pandey. "Structure–Property Relationship and Electronic Structure Calculation of Cubic YSZ Solid Electrolyte for Electrochemical Applications", Journal of Electronic Materials, 2025 Publication	<1 %
75	Dar, M.A.. "Synthesis and characterization of nano-sized pure and Al-doped lithium ferrite having high value of dielectric constant", Journal of Alloys and Compounds, 20100318 Publication	<1 %
76	P. Monisha, P. Priyadharshini, S.S. Gomathi, K. Pushpanathan. "Influence of Mn dopant on the crystallite size, optical and magnetic behaviour of CoFe2O4 magnetic nanoparticles", Journal of Physics and Chemistry of Solids, 2020 Publication	<1 %
77	S.K. Ahmed, M. Faishal Mahmood, M. Arifuzzaman, M. Belal Hossen. "Enhancement of electrical and magnetic properties of Al3+ substituted CuZn nano ferrites with structural Rietveld refinement", Results in Physics, 2021 Publication	<1 %
78	Shameran Jamal Salih, Wali M. Mahmood. "Review on magnetic spinel ferrite (MFe2O4) nanoparticles: From synthesis to application", Heliyon, 2023 Publication	<1 %
79	Submitted to Universite de Sfax Student Paper	<1 %
80	M. Belal Hossen, A.K.M. Akther Hossain. " Structural and dynamic electromagnetic	<1 %

properties of ", Journal of Magnetism and Magnetic Materials, 2015
Publication

81	Prachi Jain, S. Shankar, O.P. Thakur. "Unveiling the Structural, Optical, Electrical, and Ferromagnetic properties of Ca2+ doped mixed spinel ferrites for switching field high-frequency device applications", Ceramics International, 2024 Publication	<1 %
82	(8-29-14) http://202.56.4.123/IRPortal/annualreport/2012/Directo Report.pdf Internet Source	<1 %
83	Arpon Debnath, Md Sazzad Hossen, Rajon Saha Auntu, Sujit Kumer Shil. "High Permeability with Ultra-Soft Magnetic Behavior of Solid State Method Synthesized Al-substituted Ni-Mg-Zn Ferrites for High Frequency Applications", Surfaces and Interfaces, 2025 Publication	<1 %
84	Humbe, Ashok V., Anant C. Nawle, A.B. Shinde, and K.M. Jadhav. "Impact of Jahn Teller ion on magnetic and semiconducting behaviour of Ni-Zn spinel ferrite synthesized by nitrate-citrate route", Journal of Alloys and Compounds, 2017. Publication	<1 %
85	K.R. Rahman, F.-U.-Z. Chowdhury, M.N.I. Khan. "Influence of Al 3+ substitution on the electrical resistivity and dielectric behavior of Ni 0.25 Cu 0.20 Zn 0.55 Al x Fe 2-x O 4 ferrites synthesized by solid state reaction	<1 %

technique", Journal of Magnetism and Magnetic Materials, 2017
Publication

86	Mohamed Lamjed Bouazizi, Sobhi Hcini, Kamel Khirouni, Fehmi Najar, Abdullah H. Alshehri. "Structural and Optoelectronic Properties of Mixed Mg–Cu–Cd Spinel Chromites Prepared by the sol–gel Method Under Different Calcination Temperatures", Journal of Inorganic and Organometallic Polymers and Materials, 2023 Publication	<1 %
87	N. Mohammadinezhad, Kh Gheisari, K. Ranjbar, A. Sabahi. "Dielectric behavior of nanocrystalline Cu-Fe ferrites synthesized by plasma arc discharge process", Physica B: Condensed Matter, 2022 Publication	<1 %
88	Serine Kassem, Nour AlHajjar, Amani Aridi, Ramadan Awad. "Identification of structural and optical properties and adsorption performance of (Cd0.4Ni0.4Mn0.2)Fe2-xRuxO4 nanoparticles for the removal of Congo red dye", Arabian Journal of Chemistry, 2023 Publication	<1 %
89	Submitted to University of Birmingham Student Paper	<1 %
90	dsclatur.org Internet Source	<1 %
91	essuir.sumdu.edu.ua Internet Source	<1 %
92	Amir Hossain, A. Mimi, A.H. Zulkarnine, M.R. Hasan, Mohammad K. Alam, KA Khan, A.A.	<1 %

Momin. "Influence of Ni substitution on Structural, Optical, magnetic and transport properties of Mn0.5-xNixZn0.4Cu0.1Fe1.95Al0.05O4", Journal of Magnetism and Magnetic Materials, 2024
Publication

93 Apparao R. Chavan, Shankar D. Birajdar, Rahul. R. Chilwar, K.M. Jadhav. "Structural, morphological, optical, magnetic and electrical properties of Al 3+ substituted nickel ferrite thin films", Journal of Alloys and Compounds, 2018 <1%
Publication

94 Ibtihel Soudani, Fahad N. Almutairi, Iskandar Chaabane, Abderrazek Oueslati, Abdelhedi Aydi, Kamel Khirouni. "Conduction mechanism and dielectric relaxation in LiMg0.5Fe2O4 spinel ferrite: A temperature- and frequency-dependent complex impedance study", Journal of Physics and Chemistry of Solids, 2025 <1%
Publication

95 J.B. Shitole, S.N. Keshatti, S.M. Rathod, Santosh S. Jadhav. "Y3+ composition and particle size influenced magnetic and dielectric properties of nanocrystalline Ni0.5Cu0.5YxFe2-xO4 ferrites", Ceramics International, 2021 <1%
Publication

96 Julia Mazurenko, Larysa Kaykan, A. K. Sijo, Mykola Moiseienko, Myroslav Kuzyshyn, Nataliia Ostapovych, Mariia Moklyak. "The Influence of Reaction Medium pH on the Structure, Optical, and Mechanical Properties of Nanosized Cu-Fe Ferrite Synthesized by the <1%

Sol-Gel Autocombustion Method", Journal of Nano Research, 2023
Publication

97	Kashif Ali Kalhoro, Muhammad Khalid, Kiran Naz, Muhammad Saeed Akhtar, Muhammad Nadeem, H. H. Somaily. "Sol–gel synthesis and physical properties of Ni–Cu based spinel ferrites nanoparticles", Journal of Materials Research, 2023 Publication	<1%
98	Maninder Kaur, John S. McCloy, Weilin Jiang, Qi Yao, You Qiang. "Size Dependence of Inter- and Intracluster Interactions in Core–Shell Iron–Iron Oxide Nanoclusters", The Journal of Physical Chemistry C, 2012 Publication	<1%
99	P. Cardoso-das-Chagas, J. Pereira-Silva, A. Delgado, A.R. Rodrigues et al. "Exploring the structural, elastic, magnetic, and electrical properties of the BaFe12-xTixO19 compound obtained by co-precipitation", Materials Science and Engineering: B, 2025 Publication	<1%
100	Submitted to University of Bristol Student Paper	<1%
101	"Spinel Nanoferrites", Springer Science and Business Media LLC, 2021 Publication	<1%
102	Fai Abdullah Alfehaid, Raihane Charguia, Sobhi Hcini, Kamel Khirouni, M.L. Bouazizi. "Comprehensive structural analysis, magnetic, elastic, and optical properties of Cu–Ni–Co spinel and its potential applications", Optical Materials, 2024 Publication	<1%

103	Ferreira, Helena Susana da Costa Machado(Reis, Maria de la Salette Hipólito). "Utilização de lipossomas como modelos de biomembranas na avaliação e quantificação da actividade de anti-inflamatórios", Porto : [Edição do Autor], 2012. Publication	<1 %
104	K.J. Oviya, P. Sivagurunathan. "Structural, Magnetic and Electrochemical Properties of Nickel Manganese Ferrite (NixMn1-xFe2O4) Nanoparticles Prepared via Coprecipitation Method", Asian Journal of Chemistry, 2024 Publication	<1 %
105	Alibasha Akbar, M. Bhavani Lakshmi, Tonoy K. Das, Mihir Ghosh. "Spinel ferrites in the photocatalytic and adsorptive remediation of dyes and heavy metals: A review", Journal of Water Process Engineering, 2025 Publication	<1 %
106	Evgeny A. Gorbachev, Ekaterina S. Kozlyakova, Lev A. Trusov, Anastasia E. Sleptsova, Mikhail A. Zykin, Pavel E. Kazin. "Design of modern magnetic materials with giant coercivity", Russian Chemical Reviews, 2021 Publication	<1 %
107	Submitted to Guru Jambheshwar University of Science & Technology Student Paper	<1 %
108	Submitted to Panjab University Student Paper	<1 %
109	Somashekhar Hiremath, L.R. Naik, Geeta Chavan, Suresh Kumbar, R.B. Pujar, Shidaling Matteppanavar. "Synthesis, analysis, and characterization of thermal, magnetic, optical, and electrical properties of Al-doped	<1 %

nanocrystalline nickel zinc ferrite", Journal of Alloys and Compounds, 2025
Publication

110	Submitted to University of Glamorgan Student Paper	<1%
111	Amal Tounsi, Besma Hamdi, Ridha Zouari, Abdelhamid Ben Salah. "DFT(B3LYP/LanL2DZ), non-linear optical and electrical studies of a new hybrid compound: [C 6 H 10 (NH 3) 2]CoCl 4 ·H 2 O", Physica E: Low-dimensional Systems and Nanostructures, 2016 Publication	<1%
112	Submitted to Beirut Arab University Student Paper	<1%
113	coek.info Internet Source	<1%
114	Submitted to Indian Institute of Science, Bangalore Student Paper	<1%
115	Kacuk Cikal Nugroho, Ubaidillah Ubaidillah, Budi Purnama, Ahmad Masudi, Nurazmah Nordin, Saiful A Mazlan, Seung-Bok Choi. "The effect MnxCo(x-1)Fe2O4 WITH x = 0, 0.25 AND 0.5 AS nanoparticles additives in magnetorheological fluid", Smart Materials and Structures, 2020 Publication	<1%
116	Kiran Naz, Junaid Kareem Khan, Muhammad Khalid, Muhammad Saeed Akhtar et al. "Structural, dielectric, impedance and electric modulus analysis of Ni substituted copper spinel ferrites nanoparticles for microwave device applications", Materials Chemistry and Physics, 2022 Publication	<1%

117	M. A. Ali, M. N. I. Khan, F.-U.-Z. Chowdhury, M. M. Hossain et al. "Yttrium-substituted Mg–Zn ferrites: correlation of physical properties with Yttrium content", Journal of Materials Science: Materials in Electronics, 2019 Publication	<1 %
118	Marwene Oumezzine, Alin Iuga, Monica Enculescu, Aurelian Catalin Galca. "Structural, Frequency and Temperature Dependent Dielectric Properties of Zn2+ Substituted Ni-Co Based Spinel Ferrite (ZnxNi0.8−xCo0.2Fe2O4)", ECS Journal of Solid State Science and Technology, 2023 Publication	<1 %
119	T. Rafique, M. Atif, Atta Ur Rehman, H. Wahab, W. Khalid, Z. Ali, M. Nadeem. "Colossal permittivity, resistive and magnetic properties of zinc substituted manganese ferrites", Journal of Alloys and Compounds, 2022 Publication	<1 %
120	Submitted to University of Florida Student Paper	<1 %
121	dspace.bracu.ac.bd:8080 Internet Source	<1 %
122	publikationen.bibliothek.kit.edu Internet Source	<1 %
123	www.benchchem.com Internet Source	<1 %
124	A. M. Abdallah, Amani Aridi, Mariam Rabaa, Ramy M. Moussa, R. Awad. "Tailored physical and magnetic properties by La3+ dopants in Mg–Ni–Co nanoferrites: insight into the law of approach to saturation", Applied Physics A, 2023	<1 %

Publication

125	Ameer Azam, Arham S. Ahmed, M. Chaman, A. H. Naqvi. "Investigation of electrical properties of Mn doped tin oxide nanoparticles using impedance spectroscopy", Journal of Applied Physics, 2010 Publication	<1 %
126	Submitted to Institute of Technology, Nirma University Student Paper	<1 %
127	Jiang, Lai. "Characterizing an Effective Magnetic Field During Asymmetric Creep Motion of Dzyaloshinskii Domain Walls", Carnegie Mellon University, 2024 Publication	<1 %
128	M. Siva Ram Prasad, B. R. Babu, K. V. Ramesh, K. Trinath. " Effect of Substitution on Structural, Magnetic and Dielectric Properties of Nanocrystalline Ferrite System ", Nano, 2015 Publication	<1 %
129	M.A. Ali, M.N.I. Khan, F.-U.-Z. Chowdhury, M.M. Hossain, M.Z. Rahaman, S.M. Hoque, M.A. Matin, M.M. Uddin. "Study of physical properties towards optimizing sintering temperature of Y-substituted Mg-Zn ferrites", Results in Physics, 2019 Publication	<1 %
130	M.D. Hossain, M.A. Hossain, S.S. Sikder. "Hysteresis loop properties of rare earth doped spinel ferrites: A review", Journal of Magnetism and Magnetic Materials, 2022 Publication	<1 %

131	N. Fortas, Arwa Belkahla, S. Ouyahia, J. Dhahri, E.K. Hlil, K. Taibi. "Effect of Ni substitution on the structural, magnetic and magnetocaloric properties of Zn0.5-xNixMg0.5Fe2O4 (x = 0, 0.125 and 0.250) ferrites", Solid State Sciences, 2020 Publication	<1%
132	P. Monisha, S.S. Gomathi. "Improved photocatalytic performance in Ce3+ doped CoFe2O4 nanoparticles by modifying structural, optical, and magnetic properties", Materials Science in Semiconductor Processing, 2024 Publication	<1%
133	P.B. Wasnik, K.G. Rewatkar, S.M. Suryawanshi, M.S. Bisen, S.D. Rokade. "Structural and magnetic properties of aluminium substituted Ni-Cu spinel ferrite", Nano-Structures & Nano-Objects, 2024 Publication	<1%
134	Raju Ahmed, A.S.M. Moslehuddin, Zahid Hasan Mahmood, A.K.M. Akther Hossain. "Weak ferromagnetism and temperature dependent dielectric properties of Zn0.9Ni0.1O diluted magnetic semiconductor", Materials Research Bulletin, 2015 Publication	<1%
135	Sushen Chandra Devsharma, Md. Lutfor Rahman, Md. Jakir Hossain, Bristy Biswas, Md. Farid Ahmed, Nahid Sharmin. "Elucidation of structural, electromagnetic, and optical properties of Cu–Mg ferrite nanoparticles", Heliyon, 2024 Publication	<1%

136	V. Speziali. "Deep submicron CMOS transistors for low-noise front-end systems", 2001 IEEE Nuclear Science Symposium Conference Record (Cat No 01CH37310) NSSMIC-01, 2002 Publication	<1 %
137	nlist.inflibnet.ac.in Internet Source	<1 %
138	open.library.ubc.ca Internet Source	<1 %
139	pepite-depot.univ-lille.fr Internet Source	<1 %
140	tudr.thapar.edu:8080 Internet Source	<1 %
141	www.vinstan.com Internet Source	<1 %
142	A. A. Kadam, K. Y. Rajpure. "Compositional variation of structural, electrical and magnetic properties of Dy substituted Ni–Co spinel ferrite", Journal of Materials Science: Materials in Electronics, 2016 Publication	<1 %
143	A. Dhahri, A. Zaouali, A. Benali, N. Abdelmoulla et al. "Synthesis and study of the structural and dielectric properties of La0.67Ca0.2Ba0.13Fe1−xMnxO3 ferrites (x = 0, 0.03 and 0.06)", Journal of Materials Science: Materials in Electronics, 2021 Publication	<1 %
144	Bade Venkata Suresh, G.V.R. Seshagiri Rao, E. Nirmala Devi, Govind Nandipati. "Effect of Cr3+ substitution on the structural and magnetic properties of Co-Cu-Zn nano	<1 %

ferrites", Inorganic Chemistry Communications, 2024
Publication

145	Chandu N. Potangale, Satish K. Pardeshi. "Effect of Ni2+ substitution on magnetic, optical and electrical properties of SrFe2O4", Materials Science and Engineering: B, 2022 Publication	<1 %
146	H.R. Venkatesh, K.S. Kiran, E. Melagiriyappa. "Influence of Ce3+ substitution on structural, dielectric and impedance properties of Co-Cd nanoferrites prepared by solution combustion method", Materials Chemistry and Physics: Sustainability and Energy, 2025 Publication	<1 %
147	Khalid Mujasam Batoo. "Study of dielectric and impedance properties of Mn ferrites", Physica B: Condensed Matter, 2011 Publication	<1 %
148	M. Horchani, Aref Omri, A. Benali, M. Seif Eddine, A. Tozri, E. Dhahri, M.F.P. Graca, M.A. Valente, S.K. Jakka, B.F.O. Costa. "Synthesis and investigation on the microstructural and electrical proprieties of Ni0.1Co0.5Cu0.4Fe2O4 ferrite prepared using sol-gel route", Journal of Solid State Chemistry, 2022 Publication	<1 %
149	M. M. Rahman, M. Hedayet Ullah, S. Tabassum, M. A. Hoque, M. Harun-Or-Rashid. "Rietveld refined structural and sintering temperature dependent electromagnetic properties of Al3+ substituted Ni–Co ferrites prepared through sol–gel auto combustion method for high-frequency and microwave	<1 %

devices", Journal of Materials Science: Materials in Electronics, 2024
Publication

150	R. S. Arun Raj, Aruna Joseph, Shamima Hussain, Mohd Fahad, Tuhin Maity, P. M. Sarun, Lija K. Joy. " Frequency and temperature dependent dielectric properties of CoFe Y O : polarization and conduction mechanisms related to crystallographic symmetry and electronic transitions ", Journal of Materials Chemistry C, 2025 Publication	<1 %
151	S. Nasir, G. Asghar, Muhammad Ali Malik, M. Anis-ur-Rehman. "Structural, dielectric and electrical properties of zinc doped nickel nanoferrites prepared by simplified sol–gel method", Journal of Sol-Gel Science and Technology, 2011 Publication	<1 %
152	Saini, Lalit. "Optical Properties of Aluminium (Al) and Copper(II) Oxide (CuO) Nanoparticles and Their Composites", University of Massachusetts Lowell, 2025 Publication	<1 %
153	Sanele Dlamini, Amos Nhlapo, Thomas Moyo. "Remarkable structural and magnetic properties of nickel-zinc spinel ferrites synthesized by refluxing method", Next Materials, 2025 Publication	<1 %
154	Shyamaldas, M. Bououdina, C. Manoharan. "Dependence of structure/morphology on electrical/magnetic properties of hydrothermally synthesised cobalt ferrite	<1 %

nanoparticles", Journal of Magnetism and Magnetic Materials, 2020
Publication

155	iaeme.com Internet Source	<1%
156	qspace.qu.edu.qa Internet Source	<1%
157	www.arcjournals.org Internet Source	<1%
158	www.biltek.org Internet Source	<1%
159	1library.org Internet Source	<1%
160	A. Boutahar, R. Moubah, H. Lemziouika, S. Bahhar, M. Dahbi, M. Ounacer, E. Sebbar, M. Sajieddine, H. Bioud, E. K. Hlil. "Effects of Ce3+ doping on the structural, magnetic and hyperfine properties of cobalt ferrite nanoparticles", Indian Journal of Physics, 2023 Publication	<1%
161	Davuluri Venkatesh, G. Himavathi, K. V. Ramesh. "Structural, Magnetic, and Electrical Properties of Ni0.65Zn0.35−x Cu x Fe2 O 4 Nanoferrite System", Journal of Superconductivity and Novel Magnetism, 2015 Publication	<1%
162	Debabrata Nayak, Madhusmita Swain, Kiran, Sudha Yadav. "Investigation of the Structural, Elemental, and Magnetic Properties and Intensity-Dependent Third-Order Nonlinearity of Nickel Ferrite for Hyperthermia and Nonlinear Optical Application", Journal of Electronic Materials, 2024	<1%

Publication

163	Fakher Hcini, Sobhi Hcini, Salah Knani, Mohamed Lamjed Bouazizi, Kamel Khirouni. "Investigation of Structural, Elastic, and Optical Properties of Li0.5Co0.5FeCrO4 Spinel for Nonlinear Optical and Optoelectronic Applications", Journal of Electronic Materials, 2025 Publication	<1 %
164	Kavita Kumari, Shalendra Kumar, Ram K. Sharma, Rajesh Kumar, Ankush Vij, Faheem Ahmed, Akshay Kumar, Mohd Hashim, B.H. Koo. "Dielectric properties of spinel ferrite nanostructures", Elsevier BV, 2023 Publication	<1 %
165	Submitted to Kyungpook National University Student Paper	<1 %
166	M.D. Hossain, Md. Sarowar Hossain, M.A. Hossain, M.N.I. Khan, S.S. Sikder. "Finding the best frequency dependent performance of 3d transition metals (Co, Ni, and Mn) substituted nano magnetite for miniaturizing device applications", Ceramics International, 2024 Publication	<1 %
167	Mallesh Shanigaram, Ugendar Kodam, Ji-Sub Noh, Young-Woo Nam. "Cation distribution in MFe2O4 (M = Ni, Co): X-ray diffraction, electron spectroscopy, Raman, and magnetization studies", Journal of Physics and Chemistry of Solids, 2022 Publication	<1 %
168	Md.D. Rahaman, Tania Nusrat, Rumana Maleque, A.K.M. Akther Hossain. "Investigation of structural, morphological and electromagnetic properties of Mg 0.25	<1 %

Mn 0.25 Zn 0.5−x Sr x Fe 2 O 4 ferrites", Journal of Magnetism and Magnetic Materials, 2018
Publication

169	Phenikaa University Publication	<1 %
170	Probal Roy, S. Manjura Hoque, Sumi Akter, S.I. Liba, Shamima Choudhury. "Study on the chemical co-precipitation synthesized CoFe2O4 nanoparticle for magnetocaloric performance in the vicinity of superparamagnetic blocking temperature", Heliyon, 2024 Publication	<1 %
171	Rohit Ranga, Krishan Kumar, Ashok Kumar. "Influence of rare-earth La3+ ion doping on microstructural, magnetic and dielectric properties of Mg0.5Ni0.5Fe2-xLaxO4 (0 ≤ x ≤ 0.1) ferrite nanoparticles", Ceramics International, 2023 Publication	<1 %
172	Shrikant M. Suryawanshi, Dilip S. Badwaik, Bipin S. Shinde, Kunal D Gaikwad, Mohd. Shkir, Kamlesh V. Chandekar, Shweta Gundale. "A comprehensive study on structural, magnetic and dielectric properties of Ni0.3Cu0.3Zn0.4Fe1.8Cr0.2O4 nanoparticles synthesized by sol-gel auto combustion route", Journal of Molecular Structure, 2022 Publication	<1 %
173	Vijayakumar, M.. "Synthesis and ion dynamics studies of nanocrystalline Mg stabilized zirconia", Physica B: Physics of Condensed Matter, 200307 Publication	<1 %

174	Wahab Ullah, Muhammad Khalid, Shamoon Ismail, Muhammad Younas et al. "Structural, dielectric and impedance spectroscopic studies of (CoZnSmFe2O4)1-x/(MWCNTs)x nanocomposite for energy storage applications", Journal of Alloys and Compounds, 2025 Publication	<1 %
175	Submitted to Western Washington University Student Paper	<1 %
176	Zahra Mosleh, Shiva Moorchegani, Parviz Kameli. "Investigating the characteristics of Fe3-xZnxO4 nanoparticles: An experimental and theoretical approach", Results in Physics, 2025 Publication	<1 %
177	businessdocbox.com Internet Source	<1 %
178	gala.gre.ac.uk Internet Source	<1 %
179	library.iugaza.edu.ps Internet Source	<1 %
180	pdfs.semanticscholar.org Internet Source	<1 %
181	pdfslide.net Internet Source	<1 %
182	studentsrepo.um.edu.my Internet Source	<1 %
183	uir.unisa.ac.za Internet Source	<1 %
184	www.scielo.br Internet Source	<1 %

185 "Nanoscience and Nanotechnology in Security and Protection against CBRN Threats", Springer Science and Business Media LLC, 2020 <1%
Publication

186 A. M. A. Henaish, M. Mostafa, B. I. Salem, Hesham M. H. Zakaly, Shams A. M. Issa, I. A. Weinstein, O. M. Hemeda. "Spectral, electrical, magnetic and radiation shielding studies of Mg-doped Ni–Cu–Zn nanoferrites", Journal of Materials Science: Materials in Electronics, 2020 <1%
Publication

187 B. N. Swathi, B. R. Radha Krushna, Krishtappa Manjunatha, Wei-Che Lo et al. " Orange–Red Emitting Sr Al O :Pr Nanophosphors for Advanced Latent Fingerprints and Security Ink ", ACS Applied Nano Materials, 2023 <1%
Publication

188 Basaran, Burak. "Magnetic field-induced phase transformation and power harvesting capabilities in magnetic shape memory alloys", Proquest, 20111108 <1%
Publication

189 Hani Korek, Khulud Habanjar, Ramadan Awad. "Influence of samarium on the structural, magnetic, and gas sensing performance of cadmium zinc ferrites", Physica Scripta, 2024 <1%
Publication

190 J.N. Pavan Kumar Chintala, S. Bharadwaj, M. Chaitanya Varma, G.S.V.R.K. Choudary. "Impact of cobalt substitution on cation distribution and elastic properties of Ni–Zn ferrite investigated by X-ray diffraction, <1%

infrared spectroscopy, and Mössbauer spectral analysis", Journal of Physics and Chemistry of Solids, 2022
Publication

191 Kiran Mehmood, Atta Ur Rehman, Nasir Amin, N.A. Morley, Muhammad Imran Arshad. "Graphene nanoplatelets/Ni-Co-Nd spinel ferrite composites with improving dielectric properties", Journal of Alloys and Compounds, 2022 <1%
Publication

192 Krishna Kumar Yadav, Marina M.S. Cabral-Pinto, Amel Gacem, Ahmed M. Fallatah et al. "Recent advances in the application of nanoparticle-based strategies for water remediation as a novel clean technology–A comprehensive review", Materials Today Chemistry, 2024 <1%
Publication

193 M. A. A. Bally, M. Z. Ahsan, M. A. Islam, M. K. Alam, F. A. Khan. " Magnetic, magnetocaloric, and dielectric properties of polycrystalline perovskite La Ca Pb CoO ", AIP Advances, 2020 <1%
Publication

194 M. K. H. Bhuiyan, M. A. Gafur, M. N. I. Khan, A. A. Momin, A. K. M. Akther Hossain. "Correlations of Structural, Dielectric, Magnetic and Magnetoelectric Properties of Ca_{1-x}Sr_x (Fe_{0.5}Ta_{0.5})O₃ Multiferroic Ceramics", Materials Sciences and Applications, 2017 <1%
Publication

195	M. Madhu, A. Venkateswara Rao, N. Murali, D. Parajuli, Tulu Wegayehu Mammo. "Effect of Al3+ substitution on the synthesis, magnetic, and electrical properties of Ni0.3Zn0.5Co0.2Fe2−xAlxO4 spinel ferrites", Journal of Materials Science: Materials in Electronics, 2023 Publication	<1 %
196	Mund, H.S., and B.L. Ahuja. "Structural and magnetic properties of Mg doped cobalt ferrite nano particles prepared by sol-gel method", Materials Research Bulletin, 2017. Publication	<1 %
197	Nanzhaxi Suo, Aimin Sun, Lichao Yu, Zhuo Zuo, Xiqian Zhao, Wei Zhang, Yanchun Zhang, Liqiong Shao, Zhoujia Dang. "Effect of Al3+ ion-substituted Ni–Mg–Co ferrite prepared by sol–gel auto-combustion on lattice structure and magnetic properties", Applied Physics A, 2020 Publication	<1 %
198	Noor-ul-Haq Khan, Zaheer Abbas Gilani, Muhammad Khalid, H.M. Noor ul Huda Khan Asghar et al. "Impact of cerium substitution cobalt–zinc spinel ferrites for the applications of high frequency devices", Physica B: Condensed Matter, 2023 Publication	<1 %
199	Paul J. van der Put. "The Inorganic Chemistry of Materials", Springer Nature, 1998 Publication	<1 %
200	Pourya Motavallian, Behzad Abasht, Hassan Abdollah-Pour. "Zr doping dependence of structural and magnetic properties of cobalt ferrite synthesized by sol–gel based Pechini	<1 %

method", Journal of Magnetism and Magnetic Materials, 2018
Publication

201 Pradeep Chavan, L. R. Naik, P. B. Belavi, Geeta Chavan, C. K. Ramesha, R. K. Kotnala. "Studies on Electrical and Magnetic Properties of Mg-Substituted Nickel Ferrites", Journal of Electronic Materials, 2016 <1%
Publication

202 Punam B. Dube, Pooja G. Shinde, S.P. Jadhav, S.V. Rajmane, Dilip Garud, K.M. Jadhav. "Synthesis and characterization of La3+ doping nickel ferrite nanoparticles for antibacterial application", Ceramics International, 2025 <1%
Publication

203 Rajeshwari Mirji, Blaise Lobo, Shubharaj Mukherjee, Maudud Ahmed, P. M. G. Nambissan. "Influence of Polyaniline as Filler on the Microstructural Features and Properties of Polycarbonate: Bismuth Sulfide Nanocomposite", Journal of Inorganic and Organometallic Polymers and Materials, 2023 <1%
Publication

204 Rowshon Satara, Muhammad Samir Ullah. "Structural, elastic, microstructural, ac electrical conductivity and magnetic properties of Li–Cr–Zn ferrite ceramics", Journal of Materials Science: Materials in Electronics, 2025 <1%
Publication

205 S. Gowreesan, A. Ruban Kumar. " Preparation of Magnesium-Based Cobalt-Ferrites (Co1−xMg Fe O) Nanoparticles by Sol–Gel <1%

Auto Combustion Method ", International Journal of Nanoscience, 2017
Publication

206 Shikhil S. Wanjari, Deoram V. Nandanwar, K.G. Rewatkar, Amit V. Gongal, S.R. Sarve. "Structural and microwave absorption properties of Ni-doped Cd-La nanoferrites synthesized via sol-gel auto combustion route", Ceramics International, 2025 <1%
Publication

207 Shinde, T.J.. "Effect of Nd^3^+ substitution on structural and electrical properties of nanocrystalline zinc ferrite", Journal of Magnetism and Magnetic Materials, 201009 <1%
Publication

208 Siddikha Sultana Liyakath Ali, Satheesh Selvaraj, Khalid Mujasam Batoo, Ankush Chauhan et al. "Green synthesis of Cubic Spinel ferrites and their Potential biomedical applications", Ceramics International, 2024 <1%
Publication

209 Sidra Khalid, Saira Riaz, Samia Naeem, Aseya Akbar, S. Sajjad Hussain, YB Xu, Shahzad Naseem. "Spin polarization and magneto-dielectric coupling in Al-modified thin iron oxide films -microwave mediated sol-gel approach", Journal of Industrial and Engineering Chemistry, 2021 <1%
Publication

210 Siwar Dhahri, Aref Omri, Mohamed Houcine Dhaou, Essebti Dhahri et al. "Structural, optical, and dielectric studies on transition metals doping (Cu, Ni) in MgFe2O4 ferrites", Ceramics International, 2025 <1%
Publication

211	Somnath Sahu, Prajna P. Mohapatra, Hodam Karnajit Singh, Pamu Dobbidi. "Enhanced microwave absorbing performance of Sr2+ substituted Nickel-Cobalt nano ferrite for radar and stealth applications", Materials Science and Engineering: B, 2023 Publication	<1 %
212	Suhel Ahmed, Subrat Kumar Barik. "Preparation of novel (Sb1/2Na1/2) (Fe2/3W1/3)O3 compound by solid state reaction technique and their multiferroic property", Journal of Materials Science: Materials in Electronics, 2016 Publication	<1 %
213	T. M. Ali, S. M. Ismail, S. F. Mansour, M. A. Abdo, M. Yehia. "Physical properties of Al-doped cobalt nanoferrite prepared by citrate–nitrate auto combustion method", Journal of Materials Science: Materials in Electronics, 2021 Publication	<1 %
214	V. Ludhiya, N. Hari kumar, D. Ravinder, Avula Edukondalu. "Structural, Optical, Dielectric and Magnetic Properties of Nd3+ ion Substituted Ni-Mg-Cu Spinel Ferrites", Inorganic Chemistry Communications, 2023 Publication	<1 %
215	Y. D. Kolekar, L. J. Sanchez, C. V. Ramana. "Dielectric relaxations and alternating current conductivity in manganese substituted cobalt ferrite", Journal of Applied Physics, 2014 Publication	<1 %
216	aip.scitation.org Internet Source	<1 %
	docplayer.net	

217	Internet Source	<1%
218	dr.ntu.edu.sg Internet Source	<1%
219	dspace.iiuc.ac.bd Internet Source	<1%
220	eprints.usq.edu.au Internet Source	<1%
221	m.moam.info Internet Source	<1%
222	ore.exeter.ac.uk Internet Source	<1%
223	vdoc.pub Internet Source	<1%
224	www.bhumipublishing.com Internet Source	<1%
225	www.charge-transfer.pl Internet Source	<1%
226	www.saulibrary.edu.bd Internet Source	<1%
227	Banoth Baburao, N. Hari Kumar, Avula Edukondalu, M. Venkata Narayana, D. Ravinder. "Structural, optical, DC electrical, thermo-electric, dielectric and magnetic properties of Mg0.8Zn0.2GdxFe2-xO4 nanoparticles synthesised by citrate-gel auto combustion method", Inorganic Chemistry Communications, 2023 Publication	<1%
228	Darshan Malik, Nandita Narayanasamy, V A Pratyusha. "Essential Laboratory Techniques and Biochemical Analysis", CRC Press, 2025 Publication	<1%

229	Davuluri Venkatesh, K. V. Ramesh. " Structural, dielectric and impedance spectroscopic studies of Ni0.5Zn0.5−xLixFe O nanocrystalline ferrites ", International Journal of Modern Physics B, 2017 Publication	<1 %
230	Gul, I.H.. "Comparative study of NiFe"2"-"xAl"xO"4 ferrite nanoparticles synthesized by chemical co-precipitation and sol-gel combustion techniques", Materials Research Bulletin, 201206 Publication	<1 %
231	Haydhah, Saeed Ahmad Saeed. "Design of a Pattern Reconfigurable Massive MIMO Antenna for 5G Technology", King Fahd University of Petroleum and Minerals (Saudi Arabia), 2023 Publication	<1 %
232	Khairiah Alshehri. "Role of Mn doping to transform ZnLa0.1Fe1.9O4 nanoparticles from antiferromagnetic to ferromagnetic characteristics", Applied Physics A, 2024 Publication	<1 %
233	M. Krimi, K. Karoui, A. Ben Rhaiem. "Electrical and dielectric properties of the Li 1.5 Na 0.5 WO 4 compound", Journal of Alloys and Compounds, 2017 Publication	<1 %
234	R.N. Bhowmik, K.S. Aneesh Kumar. "Role of pH value during material synthesis and grain-grain boundary contribution on the observed semiconductor to metal like conductivity transition in Ni 1.5 Fe 1.5 O 4 spinel ferrite", Materials Chemistry and Physics, 2016 Publication	<1 %

235 Sharifa Nasrin, Most. Sharmin, A. K. M. Akther Hossain, Md. D. Rahaman. "Fabrication and unravelling the impact of iron-deficiency amount on crystal structure, micromorphology, elastic and electromagnetic properties of Ni0.25Cu0.13Zn0.62Fe2−xO4−3x/2 ferrites under different sintering temperatures", Journal of Materials Science: Materials in Electronics, 2021 <1%
Publication

236 A.A. Momin, Roksana Parvin, A.K.M. Akther Hossain. "Structural, morphological and magnetic properties variation of nickel-manganese ferrites with lithium substitution", Journal of Magnetism and Magnetic Materials, 2017 <1%
Publication

237 A.K.M. Akther Hossain, M.L. Rahman. "Enhancement of microstructure and initial permeability due to Cu substitution in Ni0.50−xCuxZn0.50Fe2O4 ferrites", Journal of Magnetism and Magnetic Materials, 2011 <1%
Publication

238 Ahmad Shahid Khan, Saurabh Kumar Mukerji. "Electromagnetic Fields - Theory and Applications", CRC Press, 2020 <1%
Publication

239 B. D. Cullity, C. D. Graham. "Introduction to Magnetic Materials", Wiley, 2008 <1%
Publication

240 Batoo, K.M.. "Structural and electrical properties of Cu doped NiFe"2O"4 nanoparticles prepared through modified <1%

citrate gel method", Journal of Physics and Chemistry of Solids, 201112
Publication

241 Biju Thangjam, Ibetombi Soibam. "Comparative Study of Structural, Electrical, and Magnetic Behaviour of Ni-Cu-Zn Nanoferrites Sintered by Microwave and Conventional Techniques", Journal of Nanomaterials, 2017 <1%
Publication

242 Le-Zhong Li, Xiao-Xi Zhong, Rui Wang, Xiao-Qiang Tu, Lei He, Rong-Di Guo, Zhi-Yong Xu. "Structural, magnetic and electrical properties in Al-substitued NiZnCo ferrite prepared via the sol–gel auto-combustion method for LTCC technology", RSC Advances, 2017 <1%
Publication

243 M.A. Ali, M.M. Uddin, M.N.I. Khan, F.-U.-Z. Chowdhury, S.M. Haque. "Structural, morphological and electrical properties of Sn-substituted Ni-Zn ferrites synthesized by double sintering technique", Journal of Magnetism and Magnetic Materials, 2017 <1%
Publication

244 Muhammad Zain Yar, Muhammad Khalid, Muhammad Yasin, Kiran Naz et al. "Structural, dielectric, and magnetic properties of nickel rich manganese substituted Li2Ni6MnxCo2-xO10 nanomaterial synthesized via sol-gel method", Physica B: Condensed Matter, 2023 <1%
Publication

245 N. Jahan, M.N.I. Khan, M.A. Ali, M.M. Hossain, M.S. Aktar, M.R. Hasan, Md. Akhtaruzzaman, M.M. Uddin. "A comprehensive study of RE ions Ho doped Ni-Zn nanoferrites synthesized <1%

by sol–gel auto-combustion techniques", Journal of Magnetism and Magnetic Materials, 2025
Publication

246 WongCarter, Katherine. "Photoprotective & Solar Light Collecting Biomimetic Molecules.", Proquest, 2014. <1%
Publication

Exclude quotes	Off	Exclude matches	Off
Exclude bibliography	On		

Final_Thesis_-_Copy_1.pdf

GRADEMARK REPORT

FINAL GRADE

/0

GENERAL COMMENTS

PAGE 1

PAGE 2

PAGE 3

PAGE 4

PAGE 5

PAGE 6

PAGE 7

PAGE 8

PAGE 9

PAGE 10

PAGE 11

PAGE 12

PAGE 13

PAGE 14

PAGE 15

PAGE 16

PAGE 17

PAGE 18

PAGE 19

PAGE 20

PAGE 21

PAGE 22

PAGE 23

PAGE 24

PAGE 25

PAGE 26

PAGE 27

PAGE 28

PAGE 29

PAGE 30

PAGE 31

PAGE 32

PAGE 33

PAGE 34

PAGE 35

PAGE 36

PAGE 37

PAGE 38

PAGE 39

PAGE 40

PAGE 41

PAGE 42

PAGE 43

PAGE 44

PAGE 45

PAGE 46

PAGE 47

PAGE 48

PAGE 49

PAGE 50

PAGE 51

PAGE 52

PAGE 53

PAGE 54

PAGE 55

PAGE 56

PAGE 57

PAGE 58

PAGE 59

PAGE 60

PAGE 61

PAGE 62

PAGE 63

PAGE 64

PAGE 65

PAGE 66

PAGE 67

PAGE 68

PAGE 69

PAGE 70

PAGE 71

PAGE 72

PAGE 73

PAGE 74

PAGE 75

PAGE 76

PAGE 77

PAGE 78

PAGE 79

PAGE 80

PAGE 81

PAGE 82

PAGE 83

PAGE 84

PAGE 85

PAGE 86

PAGE 87

PAGE 88

PAGE 89

PAGE 90

PAGE 91

PAGE 92

PAGE 93

PAGE 94

PAGE 95

PAGE 96

PAGE 97

PAGE 98

PAGE 99

PAGE 100

PAGE 101

PAGE 102

PAGE 103

PAGE 104